

## ABSTRACT

Title of dissertation: ATOM-TRAPPING AND PHOTON-COUNTING EXPERIMENTS WITH OPTICAL NANOFIBERS

Jeffrey Aaron Grover, Doctor of Philosophy, 2015

Dissertation directed by: Professor Luis A. Orozco  
Department of Physics

New platforms in quantum physics often rely on strong coupling, either between atoms and light or between different quantum systems. This thesis examines optical nanofiber atom traps as a mediator of atom-light interactions and a potential element of a hybrid system. The evanescent field around the sub-wavelength waist of an optical nanofiber possesses a small mode area that increases the cooperativity between atoms and the mode, in a manner analogous to traditional cavity QED.

We demonstrate trapping of  $^{87}\text{Rb}$  atoms with an optical nanofiber, confining hundreds of atoms with typical trap lifetimes of tens of milliseconds. We then employ single photon counting techniques to study untrapped ensembles of cold atoms around the nanofiber. A first experiment uses intensity autocorrelations of resonance fluorescence emitted into the nanofiber mode to observe a transition from classical to nonclassical photon statistics. Measuring the correlations on longer timescales reveals the motion of atoms through the optical mode, and we develop a correspondence between the transit time and atomic cloud temperature. A second experiment measures Purcell enhancement of spontaneous emission of atoms near

the nanofiber by correlating their fluorescence with a known trigger event. The spontaneous decay rate of an atom near a dielectric is modified by the induced dipole and by a change in the modes of the vacuum electromagnetic field. Our observed enhancement of  $6.5 \pm 0.9\%$  over the free-space rate matches well with calculations.

ATOM-TRAPPING AND PHOTON-COUNTING EXPERIMENTS  
WITH OPTICAL NANOFIBERS

by

Jeffrey Aaron Grover

Dissertation submitted to the Faculty of the Graduate School of the  
University of Maryland, College Park in partial fulfillment  
of the requirements for the degree of  
Doctor of Philosophy  
2015

Advisory Committee:

Professor Luis A. Orozco, Chair/Advisor  
Professor Steven L. Rolston, Co-Advisor  
Professor Mario Dagenais, Dean's Representative  
Professor Frederick C. Wellstood  
Professor Christopher J. Lobb  
Professor Mohammad Hafezi

© Copyright by  
Jeffrey Aaron Grover  
2015

## Dedication

For Moe. Your memory preserves the light that was your life.

## Acknowledgments

Scientists like to overuse a phrase oft-attributed to Newton: “If I have seen further it is by standing on the shoulders of Giants.” I have no grand delusions about how far I have seen. But if I have seen further than I might have otherwise, I owe it all to the optics of that old British fellow and to the giants in my life who have carried me, limping, to this juncture.

It would be impossible to overstate the influence of my advisor, Luis Orozco. In the beginning he taught me my first lessons in atomic physics, and the teaching continues to this day with his characteristic, indefatigable passion for his students. That instruction has not been limited to atomic physics nor physics at all, as our weekly meetings spanned all realms of culture and arts, often functioning as a literature exchange. More than this, though, his confidence in me persists despite my doubts and without that push it is certain that I would not have made it here. I am indebted to him in more ways than I convey, but I hope he accepts my leaving his tutelage as a proper first attempt at repayment.

It is rare that having two bosses is a *good* thing, but Steve Rolston was a great second advisor. He has the most scarily-keen physics intuition and an encyclopedic knowledge to match it. I’m thankful that his door was always open, where a 5-second question often turned into a 30-minute discussion about a problem.

Fred Wellstood and Chris Lobb (and that damned dil fridge!) were often the foils to our plans, but their presence kept us honest and made me a better scientist. Fred demands precision and thoroughness from us befitting of his own care,

thoughtfulness, and diligence as a scientist. And Chris reminds me of a condensed-matter version of Steve with his quick-thinking and intuitive grasp of physics. It was also welcome to have someone to inject much-needed levity into any physics situation.

It was often with much envy that I watched my labmates collaborate with Fredrik Fatemi, who appeared by all firsthand accounts to be about 10 super-postdocs wrapped into one PI. It is an uncommon privilege to have someone with such a vast knowledge of both physics and experimental techniques be present in the lab with you. I'm thankful to have had that privilege, no matter how short, towards the end of my thesis and regret that I don't have more time to learn from him.

Now for the younger folks...I'm fairly certain that Jon and I had no idea what we were getting into when we independently signed up for this project, but I am glad that we stumbled into it together. I could not envision spending those far-too-many hours with a better colleague or friend. He meets problems with an earnestness and creativity that I am supremely jealous of, never satisfied until he's figured it out. I hope we find that his skills serve us well when we start our cheese farm in the mountains soon.

No one has been more fortunate than me that Pablo decided to join our group after his internship. I've had the distinct honor of working closely with him for the last two years, and his unparalleled knowledge of all areas of physics, his experimental creativity, and his Zen-like calm have enriched my time beyond measure. I'll miss most our philosophical chats about *anything* while photon clicks accumulated

and the frequent occurrences of Pablo at the Board<sup>TM</sup>, arguably the times when I've learned the most.

Sylvain is a force in the lab, unrelentingly focused and exquisite in his technique, and he also shares Pablo's gift of being able to explain any concept off-the-cuff with striking clarity. We were doubly lucky that he, too, "chose" us from plenty of other options. His influence extended beyond the walls of the lab, from teaching us about Dirty French and Speculoos to simply being a reliable and hilarious friend.

Our postdocs Jongmin and Jared joined the group with an almost-frightening intensity and work ethic that transformed it from an effective spare parts room to a full-fledged lab. I am grateful for their mentorship and guidance as we put this thing together. I also must thank the superconducting grad students Kristen and Rangga for their companionship and shared head-scratching that made the lab a fun place to be. A cohort of other Orozco lab members made my time at Maryland more fulfilling through shared knowledge, equipment, and commiseration: David, Andres, Burkley, and, especially, Jiehang.

My science education started long before I stepped foot onto Maryland's campus. For their tireless efforts and commitment to my – and countless others' – success, I thank Matthew Corcoran, Norton Starr, Rob Benedetto, Jagu, and Jonathan Friedman.

Adam occupies a number of roles in my life: a best friend halfway across the country, a constant GChat companion, and the best physicist I know. I owe much of my intellectual development and emotional stability to his frequent advice, our discussions, my visits to Boulder, and his unwavering support.

There is nothing like a coterie of close friends to help you survive a move to a new city and to turn a low point in life into one of its highest. For that I will be forever grateful to my skangaga crew in DC: Max, Emily, Lindsay, Mark(-Frank), Sami, Karti, and Billy. But most of all Billy has carried me as my partner in our oddest of pairings, with his infectious laughter and the deepest depth of caring I have witnessed in another human. We've seen each other at our respective worsts, but that has made us each our bests.

There is no good word in the English language to define what Joe is to me, so I turn to the Turks and call him my kanka – part brother, part best friend. Through time and across borders our closeness has endured, thanks in no small part to email and YouTube. I love you, son.

My parents and my sister are my tireless cheerleaders and advocates, the ones who have made any success in my life possible. They do it all simply out of love, with the only demand being that I actually call home occasionally. Thank you for nurturing my curiosity and supporting me, often from afar.

Stafford, you entered my life unexpectedly, but now your presence seems so obvious it's hard to imagine what preceded it. Building a home with you has been one of the most fulfilling experiences of my life, and it has kept me grounded during this simultaneous and arduous path I'm now finishing. I owe you so much for keeping me calm, pleasantly distracted, and always excited for what the unknown future has in store for us. Thank you for making my life more beautiful.

And it is with great humility that I thank the JQI for its hospitality, sense of community, unequaled opportunity, and generous funding.

## Table of Contents

List of Tables	x
List of Figures	xi
List of Abbreviations	xiv
1 Introduction	1
1.1 Cooperativity	2
1.1.1 Optical nanofibers	5
1.2 Hybrid quantum systems	6
1.2.1 Neutral atoms coupled to superconducting circuits	8
1.3 Outline of thesis	10
2 Apparatus	12
2.1 New laboratory construction	13
2.2 Nanofiber pulling	13
2.2.1 The flame-brush method	14
2.2.2 Setup and procedure	15
2.2.3 Results	18
2.3 Laser systems	23
2.3.1 Cooling and probing laser: saturation spectroscopy	23
2.3.2 Repump laser: Doppler-free DAVLL	27
2.3.3 Nanofiber “blue” laser: Ti:Sapph	29
2.3.4 Nanofiber “red” laser: Nd:YAG	30
2.4 UHV system	30
2.4.1 Science chamber	31
2.4.2 Washer optics mounts	32
2.4.3 Ion pump placement	32
2.4.4 Manipulator	34
2.4.5 Nanofiber mount	34
2.5 Magnetic field control	35
2.5.1 MOT coils	36

2.5.2	MOT coil PID . . . . .	38
2.5.3	Shim coils . . . . .	38
2.5.4	Shim coil driver . . . . .	39
2.6	Optics . . . . .	39
2.6.1	Imaging . . . . .	39
2.6.2	MOT beams . . . . .	41
2.7	Photon counting . . . . .	41
2.8	Electronics and control . . . . .	43
2.8.1	Timing and DAQ cards . . . . .	43
2.9	Conclusions: improvements and laboratory relocation . . . . .	44
3	Optical nanofiber trap	45
3.1	Introduction . . . . .	45
3.2	Setup . . . . .	46
3.3	Experiment . . . . .	51
3.4	Fitting asymmetric absorption curves . . . . .	55
3.5	Conclusions . . . . .	60
4	Photon correlation measurements	62
4.1	Introduction . . . . .	62
4.2	Intensity autocorrelations . . . . .	63
4.3	The system . . . . .	64
4.3.1	Nanofiber mode structure . . . . .	65
4.3.2	Potentials . . . . .	65
4.3.3	Light shifts . . . . .	67
4.3.4	Coupling strength . . . . .	67
4.4	Theoretical background . . . . .	68
4.4.1	Transit-time effects . . . . .	68
4.4.2	Relating correlations to temperature . . . . .	69
4.4.3	Simulating atomic trajectories . . . . .	69
4.5	Experiment and results . . . . .	70
4.5.1	Apparatus . . . . .	70
4.5.2	Data and fitting . . . . .	72
4.5.3	Temperature extraction . . . . .	76
4.5.4	Atomic dynamics . . . . .	77
4.5.5	Simulations . . . . .	78
4.6	Conclusions . . . . .	84
5	Measurement of the lifetime of the $5P_{3/2}$ state of $^{87}\text{Rb}$ near a nanofiber	85
5.1	Theoretical overview . . . . .	86
5.1.1	Dipoles near surfaces: calculating $\gamma_{\text{rad}}$ . . . . .	87
5.1.2	Dipoles near waveguides: calculating $\gamma_{1\text{D}}$ . . . . .	88
5.1.3	Atom density near surfaces . . . . .	90
5.1.4	Expected decay rate . . . . .	93
5.2	Experimental setup . . . . .	94

5.2.1	Optical pulse generation and improvement . . . . .	98
5.3	Data and results . . . . .	99
5.3.1	Exponential fitting . . . . .	100
5.4	Conclusions . . . . .	103
6	Quantum hybrid system	105
6.1	Compact atom trap: GMOT . . . . .	106
6.1.1	Experimental setup . . . . .	107
6.1.2	Temperature measurement . . . . .	108
6.1.3	Theory: sub-Doppler cooling . . . . .	111
6.1.4	Atom number and density . . . . .	115
6.2	Conclusions . . . . .	119
7	Conclusions and outlook	120
7.1	Faraday spectroscopy with nanofibers . . . . .	120
7.2	Surface physics . . . . .	122
7.3	Hybrid system . . . . .	125
7.3.1	Atomic source: 2D MOT . . . . .	125
7.3.2	Interfacing fibers with superconducting circuits . . . . .	125
7.4	Self-organization . . . . .	126
7.5	Conclusions . . . . .	128
A	Nanofiber modes	129
A.1	Field equations . . . . .	129
A.2	Propagation constant . . . . .	131
A.3	Normalization . . . . .	131
B	Nanofiber vibrations	135
B.1	Transverse vibrational modes of a nanofiber . . . . .	137
B.2	Effect of heating . . . . .	141
B.3	Heterodyne technique . . . . .	142
C	Calculating van der Waals coefficients for $^{87}\text{Rb}$	145
C.1	Index of refraction . . . . .	145
C.2	Atomic polarizabilities . . . . .	147
C.3	$C_3$ and $C_4$ coefficients . . . . .	149
	Bibliography	150

## List of Tables

2.1	Nanofiber dimensions . . . . .	21
2.2	Shim coil specifications . . . . .	39
6.1	Single-stage, 50 ms far-detuned MOT parameters when scanning the detuning of a single MOT beam . . . . .	110
6.2	Multi-stage, 60 ms far-detuned MOT and 1 ms optical molasses parameters . . . . .	110
C.1	van der Waals and Casimir-Polder coefficients for $^{87}\text{Rb}$ near fused silica	149

## List of Figures

2.1	New laboratory space, circa September 2009 and May 2010 . . . . .	13
2.2	Fiber pulling apparatus schematic and photograph . . . . .	16
2.3	Flame nozzle for nanofiber pulling . . . . .	17
2.4	Three-angle pull results and comparison with simulation . . . . .	19
2.5	SEM image of nanofiber . . . . .	20
2.6	Transmission of optical nanofiber . . . . .	22
2.7	Illustration of nanofiber geometry used in this thesis . . . . .	22
2.8	$D_2$ level structure for $^{87}\text{Rb}$ with relevant lasers . . . . .	24
2.9	Optics for saturation-free spectroscopy . . . . .	26
2.10	Electronics for Pound-Drever-Hall locking of the cooling laser . . . . .	27
2.11	Optics for DAVLL . . . . .	29
2.12	UHV science chamber without coils . . . . .	31
2.13	Washers for mounting optics directly to CF flanges . . . . .	32
2.14	Washer for mounting UHV chamber to optical table . . . . .	33
2.15	UHV manipulator and load-lock . . . . .	35
2.16	Titanium nanofiber holder for UHV . . . . .	36
2.17	Science chamber with magnetic coils . . . . .	37
2.18	Vertical imaging system . . . . .	41
3.1	Illustration of trapping potential around optical nanofiber. . . . .	48
3.2	Characterization of Rayleigh scattering on the nanofiber waist . . . . .	49
3.3	Experimental schematic for nanofiber trapping experiments . . . . .	50
3.4	Transmission spectrum for atoms trapped along a nanofiber . . . . .	53
3.5	Nanofiber trap lifetime measurement . . . . .	54
3.6	Calculated light shifts (including scalar, vector, and tensor shifts) for different polarization configurations of trapping light . . . . .	56
3.7	Simulations of transmission spectra taking into account all light-shifts and finite temperature distribution of atoms in the nanofiber trap . . . . .	59
3.8	A more symmetric absorption curve due to better polarization alignment . . . . .	60
4.1	Cartoon illustration of atoms moving near an optical nanofiber showing the position-dependent coupling . . . . .	66

4.2	Experimental schematic for correlation measurements . . . . .	72
4.3	Short timescale autocorrelation function of resonance fluorescence emitted into the nanofiber guided mode, illustrating a transition from bunching to antibunching . . . . .	74
4.4	Autocorrelation function that displays transit-time effects of atoms passing through the nanofiber guided mode, with fit and residuals . .	75
4.5	Extracted transit time as a function of temperature (verified by TOF)	77
4.6	Transit time as a function of 1064-nm power for different atomic cloud temperatures . . . . .	79
4.7	An example simulated correlation function for an atom temperature of $787 \mu\text{K}$ . . . . .	81
4.8	Simulated correlation function width vs. sampling angle range for an atomic temperature of $90 \mu\text{K}$ . . . . .	82
4.9	Comparison of experimental and simulated temperature extraction . .	83
5.1	$\gamma_{\text{rad}}$ for an atom near a silica surface . . . . .	89
5.2	$\gamma_{1\text{D}}$ for a 500-nm diameter fiber . . . . .	91
5.3	Position density of thermal rubidium atoms near a silica surface . .	94
5.4	Schematic for atomic lifetime measurement . . . . .	95
5.5	Timing sequence for lifetime measurements . . . . .	97
5.6	Optical pulse from fiber-EOM . . . . .	99
5.7	Free-space decay histogram . . . . .	101
5.8	Fiber-modified decay histogram . . . . .	102
5.9	Contour plot of $\gamma_{1\text{D}}$ as a function of fiber size and atom-fiber distance	104
6.1	Cartoon schematic of hybrid system pieced together . . . . .	106
6.2	Schematic for room-temperature GMOT experiments . . . . .	107
6.3	Temperature measurements of atoms in a GMOT . . . . .	109
6.4	GMOT beam geometry and resultant lattices along different crystal axes . . . . .	113
6.5	Simulated GMOT force as a function of atom velocity for different axes and polarization configurations . . . . .	116
6.6	Atom number and density measurements of the GMOT . . . . .	117
6.7	Atom number measurements of the GMOT as a function of magnetic field gradient . . . . .	118
7.1	Free-space Faraday spectroscopy signal . . . . .	121
7.2	Transmission through nanofiber as a function of time after applying 1064-nm light to desorb atoms from surface . . . . .	123
7.3	Heating time before onset of desorption occurs, as a function of 1064-nm power . . . . .	124
7.4	Schematic illustration of self-organization of atoms trapped around an optical nanofiber . . . . .	127
A.1	Effective index of refraction as a function of V-number . . . . .	132
A.2	Fundamental ( $\text{HE}_{11}$ ) mode structure of 360-nm diameter nanofiber . .	134

B.1	Experimental schematic of vibration measurements based on photon correlations	136
B.2	Long-timescale correlation function displaying pronounced oscillations due to nanofiber vibrations	136
B.3	Geometry of the problem for a conical cantilever	139
B.4	Power spectrum of autocorrelation function, illustrating pronounced peaks. Inset shows effect of 1064-nm light on some of the observed vibrational modes	142
B.5	Fractional change in frequency as a function of 1064-nm power sent through the nanofiber	143
C.1	Index of refraction of fused silica for $\lambda$ between 0.2 and 7 $\mu\text{m}$	146
C.2	Scalar polarizabilities for the $5S_{1/2}$ and $5P_{3/2}$ states of $^{87}\text{Rb}$ as a function of imaginary angular frequency	148

## List of Abbreviations

$\gamma_{1D}$	coupling rate into a 1-dimensional optical waveguide
$\gamma_{\text{rad}}$	radiative decay rate of an atom
$\lambda/4$	quarter-wave plate
$\lambda/2$	half-wave plate
AOM	acousto-optical modulator
APD	avalanche photodiode
AR	anti-reflection
ASE	amplified spontaneous emission
AWG	American wire gauge
BS	beam-splitter
CCD	charge-coupled device
CF	Conflat
CW	continuous-wave
DAVLL	dichroic atomic vapor laser lock
DAQ	data acquisition
DDS	direct digital synthesis
EOM	electro-optical modulator
FEM	finite element model
FPGA	field-programmable gate array
GMOT	grating-mirror magneto-optical trap
GRIN	gradient index of refraction
HWP	half-wave plate
JQI	Joint Quantum Institute
LHS	left-hand side
LP	low pass (filter)
MCS	multi-channel scaler
MOT	magneto-optical trap
Nd:YAG	neodymium-doped yttrium aluminium garnet
NISP	Nanoscale Imaging Spectroscopy and Properties
NIST	National Institute of Standards and Technology
NRL	Naval Research Laboratory
OD	optical depth
ONF	optical nanofiber
PBS	polarizing beam-splitter
PD	photodetector
PDH	Pound-Drever-Hall
PFI	programmable function interface
PID	proportional-integral-derivative

PM	polarization-maintaining
Q	quality factor
QED	quantum electrodynamics
QWP	quarter-wave plate
RHS	right-hand side
SEM	scanning electron microscope
SPCM	single-photon counting module
SC	superconducting
SS	stainless steel
TCSPC	time-correlated single-photon counting
Ti:Sapph	titanium:sapphire
TOF	time of flight
TTL	transistor-transistor logic
UHV	ultrahigh vacuum

## Chapter 1: Introduction



A main thrust in the engineering of quantum systems is the generation of strong coupling. These enable, for instance, high quantum efficiency, fast exchange of information before relaxation or decoherence occurs, and strong nonlinearities approaching the point where a single photon can saturate a single atom. Depending on the application, the interactions might occur between constituents within the same system or between different quantum systems, often mediated by photons.

In the case of photon-mediated interactions, the advent of cavity QED [1], whereby cavities formed by mirrors or other structures modify the vacuum modes of the electromagnetic field while providing a preferential mode for the coupling, marked a transformative milestone. Cavity QED ushered in the ability to sufficiently isolate a quantum system from its environment and control nearly all of its degrees of freedom [2]. This has led to the observation of increased [3] and inhibited [4] spontaneous emission rates, the generation of highly nonclassical photon states [5], and has been realized within many different regions of the electromagnetic spectrum, e.g. from the microwave [5, 6] to optical [7]. It is within this context that we want to frame our study of atom-light interactions, using the notion of cooperativity to motivate our use of evanescent waveguides.

## 1.1 Cooperativity

Consider a two-level atom with dipole moment  $\vec{d}$  interacting with an electric field  $\vec{E}$ . The parameter  $g$  encodes the strength of the coupling,

$$g = \frac{\vec{d} \cdot \vec{E}}{\hbar}. \quad (1.1)$$

For an atom with decay rate  $\gamma$  and a field with decay rate  $\kappa$ , we define the single-atom cooperativity to be [2]

$$C_1 = \frac{g^2}{\kappa\gamma}. \quad (1.2)$$

A cooperativity of  $C_1 > 1$  then signifies a coupling rate between atom and field that overcomes the decays of both the atom and the optical field. This places the system in the so-called strong coupling regime, which was a longstanding goal within the quantum optics community and has been achieved in a plethora of systems, such as ions [8], Rydberg atom in microwave cavities [5], neutral atoms in optical cavities [7], and superconducting circuits in planar waveguides [9].

To better understand how one can coerce a system into the strong coupling regime, we can think of the cooperativity in a different way. We illustrate the argument by considering a high-finesse Fabry-Pérot cavity with mirror transmission  $T$  and optical length  $L$  so that its FWHM linewidth is  $\kappa = cT/2L$ . The electric field amplitude for a field with an average energy of a single photon within this mode is

given by

$$E = \sqrt{\frac{\hbar\omega}{2\varepsilon_0 V}}, \quad (1.3)$$

defining the mode volume to be  $V = A_{\text{mode}} \times L$ . The free-space linewidth of the atom from Fermi's Golden Rule is

$$\gamma = \frac{4\omega^3}{3c^2} \frac{d^2}{4\pi\varepsilon_0\hbar c}, \quad (1.4)$$

where  $d$  is the magnitude of the dipole moment of the atom and  $\omega = 2\pi c/\lambda$  is the resonant angular frequency of the decay transition. Combining these expressions into Eq. 1.2 yields a single-atom cooperativity of [10]

$$C_1 = \frac{A_{\text{atom}}}{A_{\text{mode}}} \times \frac{1}{T}. \quad (1.5)$$

Here we have defined the “area” of the atom,  $A_{\text{atom}}$ , to be the resonant scattering cross section,  $\sigma_0 = 3\lambda^2/2\pi$ . This gives us a geometric framework with which to think about the cooperativity.

Efforts to increase  $C$  then follow a few different tacks. One method recognizes that the total cooperativity is directly proportional to the number of atoms interacting with the mode,  $C = N \times C_1$ , so that one can simply increase the atom number. Vapor cells with high atomic densities have used this principle to observe coherent processes such as electromagnetically-induced transparency (EIT) [11]. The Nobel Prize-worthy efforts of Serge Haroche focused on decreasing  $T$  with microwave cavities possessing finesse greater than  $10^9$  while making sure that the cross sec-

tion of the cavity significantly overlapped with the properly aligned rydberg atoms, allowing his group to create highly nonclassical states and perform quantum non-demolition measurements of photon jumps [5]. Recent advances in superconducting technology have allowed physicists to create nonlinear quantum circuits that behave like “artificial atoms” [12]. By coupling these so-called qubits to a high-quality-factor coplanar resonator, scientists have engineered an analog of cavity QED dubbed circuit QED that achieves couplings far beyond what have been realized in optical systems [6, 9]. This architecture does rely on the large finesse of the cavity to increase  $C$ , but more than that they have made the area of their “atoms” (antennae, qubits) exceed that of the mode by a large extent.

More recently, some groups have moved away from the use of a traditional cavity altogether, trying to increase the cooperativity of an atom in free space. They use a parabolic mirror that focuses a laser such that the focussed beam has the same structure as the dipole radiation pattern of a single atom, thereby increasing the ratio of the respective areas [13–15]. Others use high-NA optical systems to focus light to a small spot and achieve high coupling in free space [16–18].

This thesis will focus on an attempt to increase the atom-light cooperativity that draws on a couple of these ideas, taking advantage of the evanescent fields of nanophotonic waveguides [19, 20]. Nanophotonic waveguides are not like the traditional optical cavities with high finesse discussed above, but they do modify the vacuum mode structure in a nontrivial way. As a result of this and the appreciable overlap between the atomic and optical areas, one can realize strong atom-photon interactions with these systems. We will consider waveguides formed by

thinning single-mode optical fibers to sub-wavelength diameters, so-called optical nanofibers [21–24]. There is an active area of research studying waveguides constructed via nanofabrication techniques that couple either to neutral atoms [25–27] or to spins that possess atom-like structure [28].

### 1.1.1 Optical nanofibers

Reducing the thickness of an optical fiber to sub-wavelength diameters changes the boundary conditions such that a significant fraction of the light propagates in an evanescent field [19]. In this regime, the optical depth per atom is a few percent so that a modest atom number can achieve large optical thicknesses. To confine atoms along the nanofiber for appreciable lengths of time, one can create an optical dipole potential by sending beams down the fiber tuned to the red and blue of the relevant atomic transition [19]. The differing decay lengths of the two colors, combined with the attractive van der Waals surface interaction, produce a potential a few hundred microkelvin deep and a few hundred nanometers from the fiber. Moreover, counter-propagating one of the trapping beams can form one-dimensional lattices along the nanofiber.

This scheme has been used to trap cesium [21–23], opening the door to reach the strong-coupling regime with these ensembles. Trapping lifetimes of tens of milliseconds and coherence times of  $\sim 600 \mu\text{s}$  [29] confirm that this is a viable platform ~~in atomic physics~~. Other research explores forming cavities on nanofibers to increase the cooperativity [30–32], coupling the spin and orbital degrees of freedom of the

light [33, 34], producing highly nonlinear phase shifts with atoms in the mode [35], coupling quantum dots to the nanofiber [36], as well as storing pulses in the atoms via EIT [37, 38].

Our work with nanofibers in this thesis centers on extending optical trapping to rubidium [24] and directly measuring the cooperativity with photon counting techniques. We also seek to interface this ensemble with another quantum system consisting of a superconducting circuit, which we discuss in the next section.

## 1.2 Hybrid quantum systems

A future with more complex quantum systems will require methods to connect spatially-separated elements of that network [39, 40]. In this scenario, photons present the most promising candidate for transferring information as the “flying qubits” between stationary qubits given their ability to propagate over long distances with little loss. On the other hand, what makes a sedentary qubit good depends largely on what it is used for.

Superconducting (SC) qubits have flourished as a potentially scalable processor of quantum information, implementing nontrivial quantum algorithms [41, 42], entangling three qubits [43], and performing a quantum simulation of the Hubbard model [44]. Despite these remarkable successes, however, the coherence times of SC qubits remain quite short when compared to those achieved in atomic systems where, for example, neutral atoms can maintain two seconds of ground-state coherence [45]. This has spurred a concerted interest in interfacing SC circuits with other quantum

systems that can better store the information generated by the superconductor [46].

SC qubits emit microwave photons in the GHz range so that their propagation in dielectric waveguides is lossy over distances longer than a few centimeters [47]. For this reason, some hybrid system realizations aim to upconvert these photons into the optical band for better transfer fidelity and reversibly retrieve them at another node [48, 49]. The coupling of a SC resonator with an optomechanical oscillator recently demonstrated a conversion efficiency of 10% and offers a promising link between the microwave and optical regimes [50].

Most other methods pursue a direct coupling, owing to the fact that the hyperfine structure of alkali atoms and other spin systems posses energy scales comparable to those of superconductors. Here the exchange of microwave photons through a magnetic dipole interaction mediates the coupling [46]. Because the single-atom, single-photon coupling strength is typically very small ( $g/2\pi \approx 100$  Hz), most realizations of this hybrid system will take advantage of the ensemble enhancement of the Rabi rate, which scales as  $\sqrt{N}$  [1].

Solid-state spin systems such as NV centers have enjoyed the most experimental progress as a memory for a SC circuit, as they can be placed in close proximity to the superconductor without the need for complicated trapping mechanisms [51–58]. These experiments have reached the strong-coupling regime between the spins and a resonator [53], coupled a qubit to the spins [55, 57], and demonstrated coherent storage of microwave photons in the ensemble [56, 58]. These results are making a bonafide hybrid quantum system a more immediate reality.

The hybrid system that interests us in this work is that of a SC circuit coupled

to an ensemble of neutral atoms, which has garnered theoretical attention [59–63] and recent experimental progress [64–69]. This particular brand of hybrid system adds the complication of needing either optical or magnetic trapping (or both) to bring the atoms close enough to the superconductor such that the coupling becomes appreciable. Despite these difficulties, neutral atoms remain a promising candidate due to the long coherences in the hyperfine clock states and the lack of large inhomogeneous broadening mechanisms that exist in many bulk spin systems. We discuss our particular vision in the next section.

### 1.2.1 Neutral atoms coupled to superconducting circuits

The difficulty of trapping atoms near a superconductor stems from both the cryogenic environment and the superconductor itself. In order to ensure that a quantum circuit has low thermal excitation probability, it must be housed inside of a dilution refrigerator that can reach temperatures of tens of millikelvin. The cooling power at the base temperature stage is usually on the order of  $100 \mu\text{K}$  (e.g. our Oxford Triton 200 Cryofree system will heat up to  $100 \text{ mK}$  when  $200 \mu\text{W}$  of heat is applied to the mixing chamber plate), necessitating that great care be taken when designing an atomic trap for this environment. Moreover, the superconductor itself is perilously sensitive to photons [70, 71] and magnetic flux [72, 73], placing even more stringent restrictions on the types of traps one can consider.

Magnetic chip traps for this style of hybrid system are an active area of research [61, 65–69]. The group of József Fortágh at the University of Tübingen has re-

cently demonstrated coherence times of seconds in small ( $10^4$  atoms) BECs trapped near superconducting microwave circuits [67] and observed the sensitivity of these atom clouds to quantized flux in a SQUID [69], both performed in 4.2 K cryostats. An ongoing effort in their group is performing these experiments inside a dilution refrigerator, where they have achieved a MOT within a higher-temperature region and eventually a scheme of magnetic transport coils will bring the atoms to the science region at millikelvin temperatures [68].

Our proposal instead uses the low-loss optical nanofiber trap to create our atomic ensemble [64]. The superconducting circuit at present consists of a lumped-element,  $LC$  resonator with resonant frequencies near 6 GHz and quality factors greater than  $10^5$ . The atoms will then be trapped within a few micrometers of the inductor line of the resonator in order to maximize the magnetic dipole coupling. Ultrahigh transmissions of 99.95% [74] place these devices in a regime where the scattered light from the thin waist is low enough so that the quality factor of the resonator remains high [75].

We now estimate the cooperativity of this system based on current state-of-the-art numbers. Nanofiber traps typically contain  $10^3$  atoms, but implementing deterministic loading [76] can increase that number to  $10^4$ . The linewidths of the SC resonators are about  $10^4$  kHz, whereas the best-reported decay rate of nanofiber-trapped atoms is roughly  $1$  kHz ]. Given a coupling strength of  $g = 100$  Hz, these numbers translate to a total cooperativity of  $C = 10$ , which places this system into the strong coupling regime.

### 1.3 Outline of thesis

This thesis is concerned with a series of experiments performed with optical nanofibers, with an eye toward their ultimate integration with a superconducting device. In Chap. 2 we present the design and construction of the atomic physics side of the experiment, where an empty room was converted into a laboratory. It highlights the aspects of the apparatus, such as the nanofiber puller, ~~that~~ differ from some of the standard features that are ubiquitous in laser cooling and trapping experiments. Chap. 3 demonstrates the trapping of  $^{87}\text{Rb}$  atoms around an optical nanofiber produced within our laboratory. This marks an important first step for using nanofibers as part of a hybrid system. Much of this chapter is almost verbatim from Ref. [24].

In Chap. 4 we move to the study of photon correlations in atom-ONF systems and how they can inform our knowledge of atomic dynamics and the mode structure of these waveguides. Measuring the transit time of atoms through the optical mode allows us to extract the temperature of the atomic cloud. The text of this chapter is almost verbatim a paper we have recently submitted. We present an extension of these correlation measurements in Chap. 5, where we use time-correlated single-photon counting to measure the enhancement of spontaneous decay of atoms near the nanofiber surface. This is a useful confirmation – in the time domain – of a Purcell-like effect in this system.

Coming back to the overall hybrid system in Chap. 6, we summarize how the various pieces will fit together. We then delve into a particular implementa-

tion of a compact laser cooling and trapping scheme and demonstrate that it can bring atoms to sub-Doppler temperatures, which is presented almost verbatim from the published paper Ref. [77]. Finally, in Chap. 7, we highlight four studies with nanofibers that are either planned or ongoing within our group. Three Appendices add discussions regarding mode structure of optical nanofibers, correlation measurements of nanofiber vibrations, and a calculation of van der Waals coefficients between  $^{87}\text{Rb}$  and fused silica.

## Chapter 2: Apparatus

Starting an atomic physics laboratory from an empty room requires a combination of planning, building, designing, buying, soldering, and aligning. This chapter outlines the process of assembling an experiment from scratch that can cool, trap, and study neutral atoms around optical nanofibers – from conception to data-taking. It functions almost as a “parts list” for the experiment, chronicling the aspects that are particular to this setup or keeping track of how things fit together for future students on the project.

This chapter is organized in the following manner. We first summarize the initial conversion of office space to laboratory space in Sec. 2.1. Next we discuss the nanofiber puller and highlight the relevant results in Sec. 2.2. Sec. 2.3 outlines the lasers and control systems used to form a MOT and a nanofiber dipole trap. We then proceed to cover the distinctive parts of our ultrahigh vacuum (UHV) system in Sec. 2.4. Secs. 2.5 and 2.6 catalog the magnetic and optical systems built around this UHV environment to create and image cold atom clouds. In the next section, Sec. 2.7, we present the electronics and detectors that facilitate the photon-counting experiments that are central to this thesis. Sec. 2.8 lists the devices and DAQ cards that oversee the synchronization of many the devices discussed earlier in the chapter.

Finally, Sec. 2.9 concludes and offers an outlook on the new laboratory space in the basement of the PSC, as well as some experimental improvements in the works.

## 2.1 New laboratory construction

The fall of 2009 marked the beginning of the conversion of literally empty former office space to a cold atom laboratory (see Fig. 2.1). We began by populating the room with fire- and chemical-resistant desks from VWR. A  $4' \times 12' \times 12''$  optical table from TMC was installed in May 2010, with our first lasers following about a month later. We built a system of 80/20 shelves around the table to house electronics

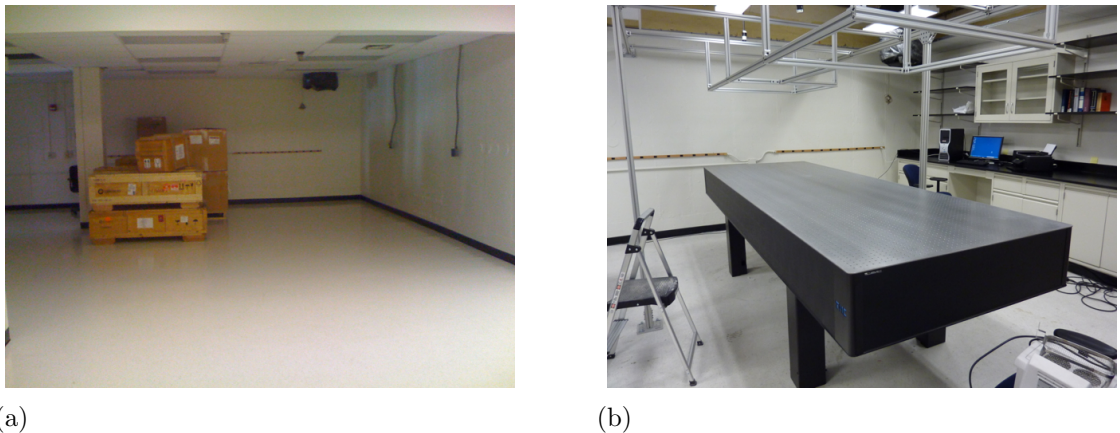


Figure 2.1: (a) Empty laboratory space in Physics 1305B before construction, September 2009. (b) Initial optical table installation and 80/20 construction.

## 2.2 Nanofiber pulling

The success of this experiment hinges on the creation of optical nanofibers with high transmission. High transmission ensures that sufficient optical powers ( $\sim$  mW) can be sent through the ONF under vacuum without breaking it, as well

as minimizes the scattering of photons into the dilution refrigerator. This section provides an overview of the general fiber pulling process as well as the specific apparatus in our laboratory, with more details to be found in the PhD thesis of Jonathan Hoffman [78] and Ref. [74].

### 2.2.1 The flame-brush method

Many methods exist to thin normal, single-mode fibers to subwavelength diameters through physical or chemical mechanisms [79, 80]. The non-chemistry techniques rely on heating a small section of fiber and pulling on either end, where the choice of heat source presents the biggest variation between the different methods. Our laboratory utilizes a small, hydrogen-oxygen flame to heat the fused silica to just below its melting point (1585 °C). At this temperature where the glass flows but does not melt, conservation of volume of the glass dictates how the fiber radius evolves during the pull [81]. After a time  $t$ , the initial radius  $r_0$  becomes

$$r = r_0 \exp \left( -\frac{t v_f}{2L_0} \right), \quad (2.1)$$

where  $L_0$  is the flame width and  $v_f$  is the pulling velocity. A stationary flame results in an exponential taper, with the final radius dependent on the duration and velocity of the pull. Varying the relative position of the so-called hot zone throughout the pulling process allows for the production of controlled taper geometries [74, 81–85], whereby short exponential sections are stitched together to approximate the desired taper shape.

This shape becomes important when considering experimental length constraints, which can jeopardize the conditions of total internal reflection that ultimately govern the adiabaticity of the shape. We want to minimize the excitation of higher-order modes in as short of a fiber as possible. This issue is especially prescient<sup>1</sup> for our hybrid experiment with an ONF in a dilution refrigerator, where the lengths set by Eq. 2.1 would be too long for the area below the mixing chamber plate. Sec. 2.2.3 will present our results for pulling fibers with shorter, linear tapers while maintaining ultrahigh transmission.

### 2.2.2 Setup and procedure

Fig. 2.2 displays our fiber puller in both a schematic and photograph. The entire apparatus is under a softwall clean room (initial rating Class 100) with HEPA filters in the ceiling to maintain a dust-free environment. Preventing dust from falling onto the fiber before or after fabrication is crucial for achieving high transmission, as we will discuss in more detail later in this section.

High-precision linear bearing stages (Newport XML 210) mounted to a granite slab perform the controlled pulling of the fiber. The flatness of the granite slab allows the stages to perform within their specifications, and its mass minimizes jerk when the motors change directions. A flame formed by a stoichiometric ratio of hydrogen and oxygen provides the heat source so that the only combustion product is water, mitigating contamination of nanofiber surface. The flame head consists of 29, 228- $\mu\text{m}$  holes in a  $1 \times 2\text{-mm}$  hexagonal pattern (holes made by Twin City EDM) on

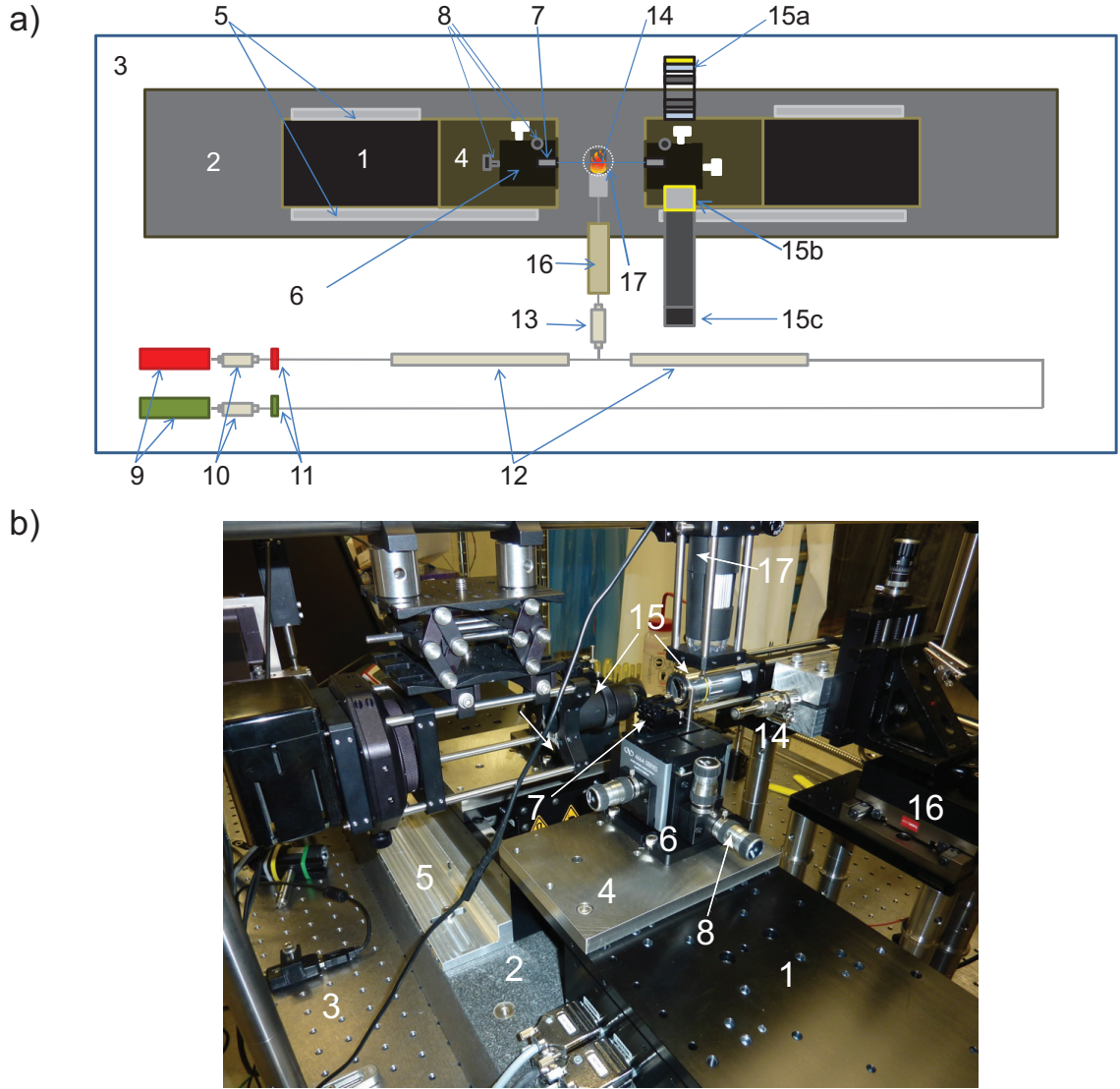


Figure 2.2: (a) Experimental schematic of the fiber puller (top view). (b) Photograph of apparatus. 1) Fiber motors. 2) Granite slab. 3) Optical breadboard. 4) Adapter plates. 5) L-bracket mounts. 6) XYZ fiber alignment flexure stages. 7) Fiber holders. 8) Adjustment screws. 9) Gas flow meters. 10) Gas line filters. 11) Valves. 12) Flexible pipes. 13) Fine gas line filter. 14) Nozzle. 15) (a) Kohler illumination system. (b) Optical microscope. (c) CCD camera. 16) Flame positioning motor. 17) USB camera aligned vertically above fiber. (figure from Ref. [74])

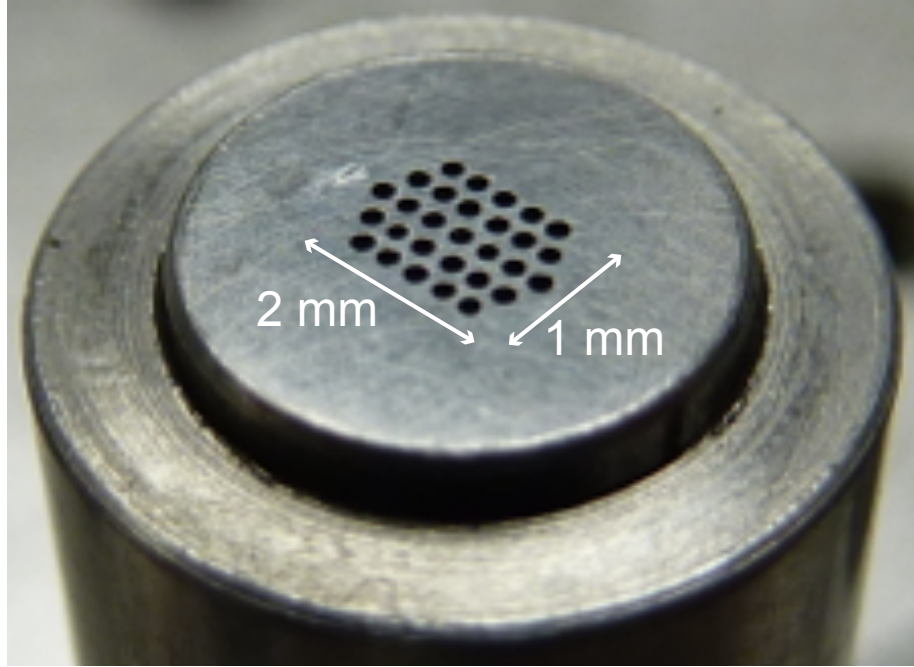


Figure 2.3: Image of stainless steel nozzle for hydrogen-oxygen flame in the nanofiber pulling rig. The  $1 \times 2$  mm array consists of 29,  $228\text{-}\mu\text{m}$  holes.

a stainless steel plate (see Fig. 2.3). The small hole size is a safety precaution to ensure that hydrogen gas does ~~no~~ back flow into the line, but the dimensions ensure that the Reynolds number (1.9 for  $\text{H}_2$  and for 6.3  $\text{O}_2$ ) is low enough for laminar flow ( $< 2100$ ) of the gases.

Before each pull, the fiber-flame position is set to maintain a repeatable flame size. The fiber ends are then aligned relative to one another using an *in-situ* imaging system ( $\text{NA} = 0.28$ ,  $2 \mu\text{m}$  resolution), which fixes the pulling axis to be parallel to the flame nozzle face. Most importantly, the plastic fiber buffer is mechanically stripped off of the region of fiber to be stretched, and this region is repeatedly cleaned with methanol and cleanroom-compatible wipes (Ted Pella) until no particulate remains. The fiber is then placed into the fiber clamps, and the cleaned fiber is imaged section by section with the microscope to verify that the fiber is particulate- and dust-free.

If anything is visible in the images, the cleaning procedure is repeated until this test is passed.

The pull is then initiated, and the pulling motors are computer-controlled by a Newport XPS controller, which uses pre-generated trajectories to direct the motors. These trajectories are calculated by an algorithm (see Refs. [78, 82]) that generalizes Eq. 2.1 to create non-exponential tapers. As noted above, the idea is to stitch together short exponential sections in order to approximate any desired taper. One experimental deviation from this picture is how the hot zone is varied, as air currents would disturb a moving flame and degrade the pull. Instead the algorithm works in the rest frame of the flame, imparting that motion into the pulling motors so that one leads and the other lags during each pull step.

### 2.2.3 Results

As a proof of concept, we stretch a single-mode, SMF-28 fiber to a final waist radius of  $10 \mu\text{m}$  with three linear sections of different taper angle (5, 2, and 3 mrad) [78]. The larger final radius allows the imaging system within the apparatus to characterize the entirety of the fiber profile. Fig. 2.4 displays the measured fiber geometry compared with the intended geometry. Over the 60-mm pull, the maximum deviation between the input control program to the apparatus and the output of the puller is  $\sim 2\%$ , confirming that this technique can produce non-exponential tapers with high accuracy.

Verifying nanometer-scale radii is beyond the resolution of the *in-situ* imaging

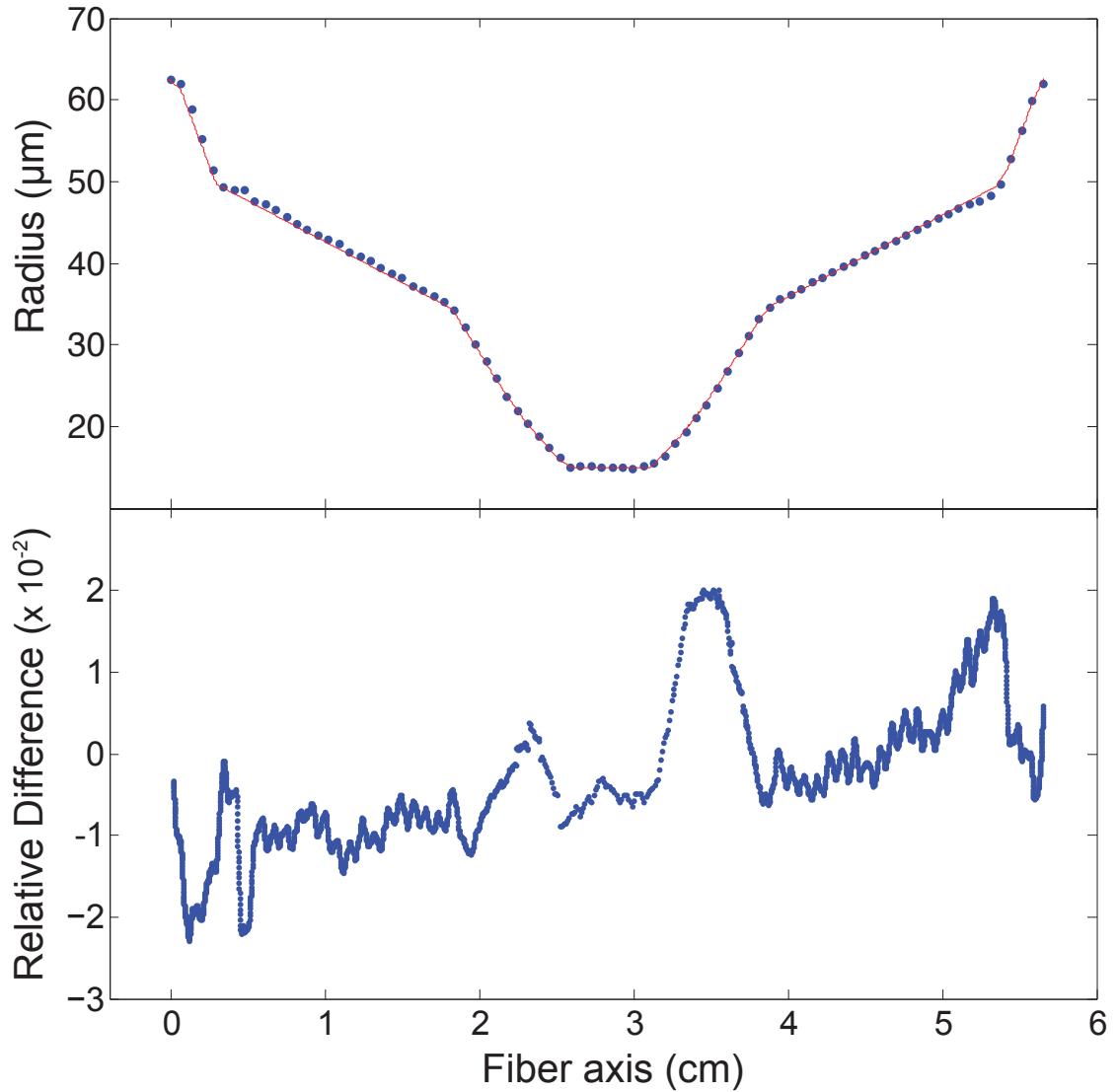


Figure 2.4: Profile of a triple-angled, linear-taper fiber. (a) Blue dots are data from optical microscope images, and the red line is expected profile from simulation. The three angles of 5, 2, 3 mrad end at respective radii of 50, 35, and 25  $\mu\text{m}$ , with a final radius of 15  $\mu\text{m}$ . (b) Relative error between measured and expected value, with an RMS error of 0.0187 (figure from Ref. [74]).

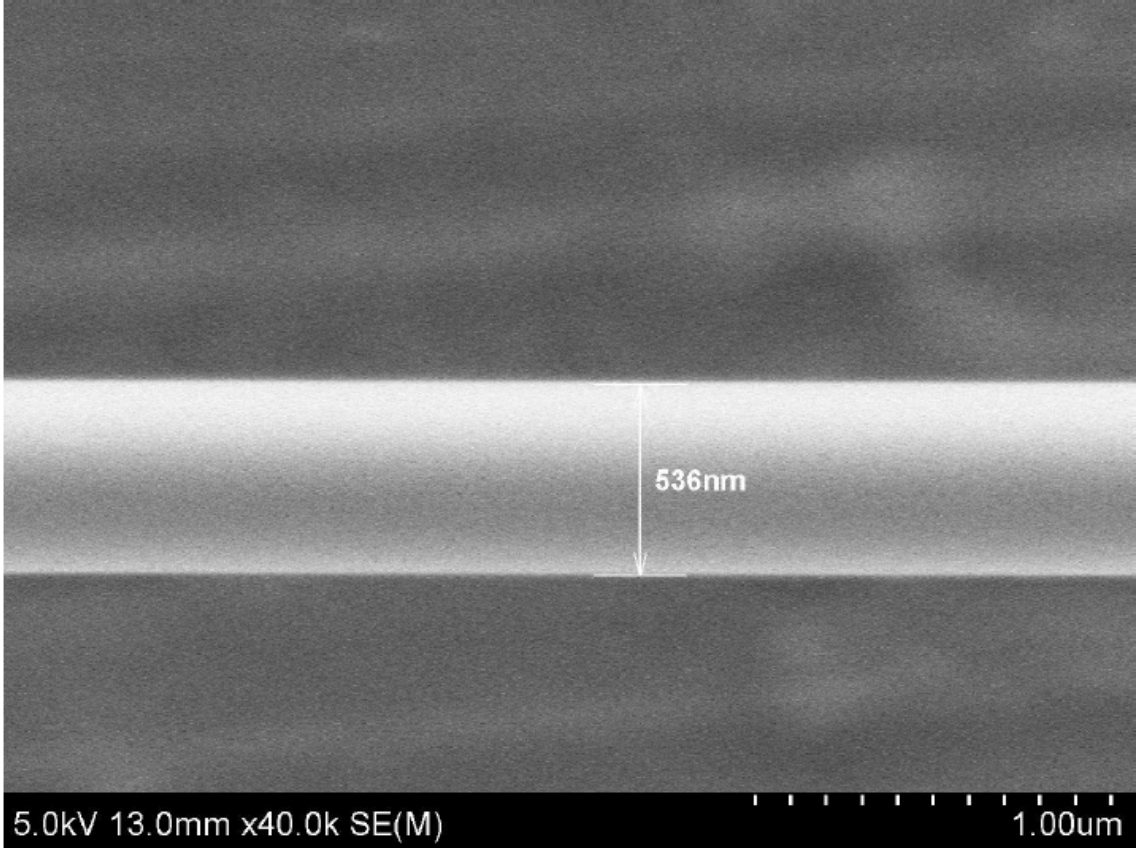


Figure 2.5: SEM image of 536-nm diameter nanofiber (design diameter: 500 nm) taken at the NISP Lab at UMD (figure from Ref. [74]).

system, and we rely on non-optical imaging methods. Some fibers are (destructively) coated with graphite and imaged in a scanning electron microscope (SEM). Fig. 2.5 shows an example of one such fiber with a final waist diameter of  $536 \pm 12$  nm, compared to a design diameter of 500 nm. We find that nanofibers are systematically  $\sim 10\%$  larger than the design size, likely due to small air currents pushing the thin fiber into a different region of the flame [78].

In addition to a particular waist diameter, nanofibers must possess high transmission for use in optical trapping experiments. Losses arise from Rayleigh scattering in the silica, fluorescence from impurities in the glass, nonadiabatic excitation

of higher-order-modes in the taper region, and surface scattering from contaminants on the waist. The first two loss mechanisms are inherent to the glass, while the latter two can be eliminated through careful fabrication. Surface contaminants are minimized by adhering to the cleaning procedure outlined in Sec. 2.2.2 and keeping the nanofiber in a dust-free environment post-pull. Gradual tapers tend to minimize the excitation of higher-order modes, and while an optimal adiabatic taper exists [81, 86], we find that a single-angle taper of 2 mrad works well. Monitoring the transmission during the pull allows us to extract an overall transmission of  $99.95 \pm 0.02\%$  (see Fig. 2.6) for a nanofiber with an angle of 2 mrad and 500-nm diameter waist. These dimensions are similar to the nanofiber that we use for the subsequent experiments in this thesis, and we present the geometry in Fig. 2.7 and Table 2.1.

The region between 325 s and 425 s in Fig. 2.6 exhibits pronounced oscillations in the transmission. These oscillations are the result of beating between higher-order modes that are excited when the fiber thins to a radius (typically about  $23 \mu\text{m}$  for SMF-28 fiber) that supports them [74, 86–88].

Region	Initial radius ( $\mu\text{m}$ )	Final radius ( $\mu\text{m}$ )	Length (mm)	Taper angle (mrad)
1	62.5	6	28.25	2
2	6	0.25	10.75	N/A
3	0.25	0.25	7	0

Table 2.1: Dimensions of the nanofiber used in this thesis. The regions refer to Fig. 2.7.

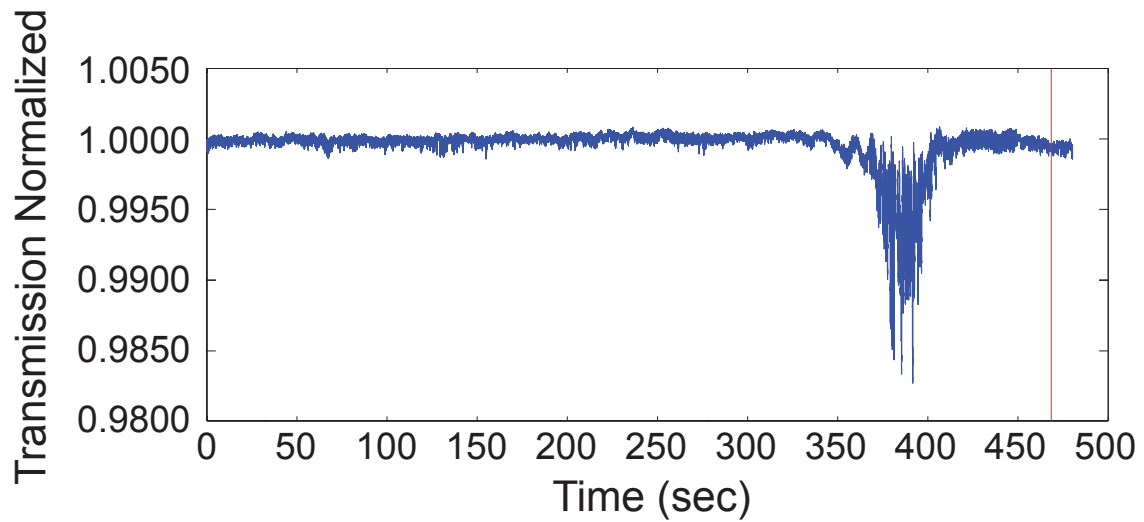


Figure 2.6: Nanofiber transmission measured during the pulling process for a taper angle of 2 mrad down to 6  $\mu\text{m}$ , and an exponential taper from there to the final radius of 250 nm. The waist is 5 mm long. The vertical red line demarcates the end of the pull. The final transmission is  $99.95 \pm 0.02\%$ .

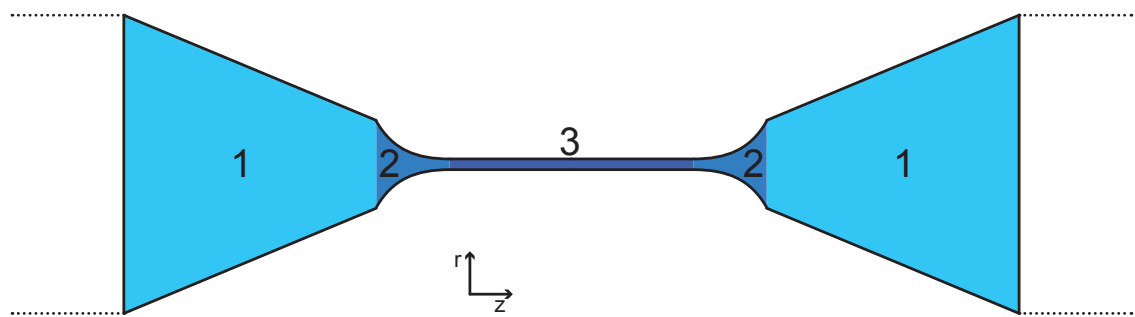


Figure 2.7: Illustration of geometry of the nanofiber used throughout this thesis. An exponential section (region 2) connects the linear taper (region 1) to the uniform nanofiber waist (region 3). The region in white is the unmodified fiber. The parameters are given in Table 2.1. Drawing is not to scale.

## 2.3 Laser systems

This section details the four lasers used in the experiment, two for creating the MOT and two for forming the nanofiber dipole potential. The two MOT lasers require frequency stabilization in order to consistently address the hyperfine levels within the  $D_2$  transition of  $^{87}\text{Rb}$  (see Fig. 2.8), and so we discuss the different locking schemes for each laser. Because the nanofiber trap lasers are far off-resonant beams ( $|\omega_{\text{trap}} - \omega_0| \gg \gamma_0$ , where  $\omega_0/2\pi$  and  $\gamma_0/2\pi$  are the atomic resonant frequency and excited-state linewidth, respectively), small drifts in the frequencies are unimportant.



### 2.3.1 Cooling and probing laser: saturation spectroscopy

The laser beam that provides (sub-)Doppler cooling for our magneto-optical trap originates from a CW diode with a tapered amplifier (Toptica TA Pro) that generated roughly 1.3 W of power at 780.24 nm upon initial purchase in 2010. To lock this laser we employ a variation of the Pound-Drever-Hall (PDH) technique [89], which typically uses a stable optical cavity as a reference in order to feed back to the laser. Locking requires knowledge of whether the laser is above or below the resonant frequency, and because the lineshape of a cavity or atomic resonance is a symmetric Lorentzian, analog techniques do not enable us to use the intensity of a transmitted or reflected signal as our error signal<sup>1</sup>. The *phase* of the lineshape,

---

<sup>1</sup>The authors in Ref. [90] demonstrated that with sufficient accuracy in their analog-to-digital conversion, they can use microcontrollers to lock directly to the resonance peak.

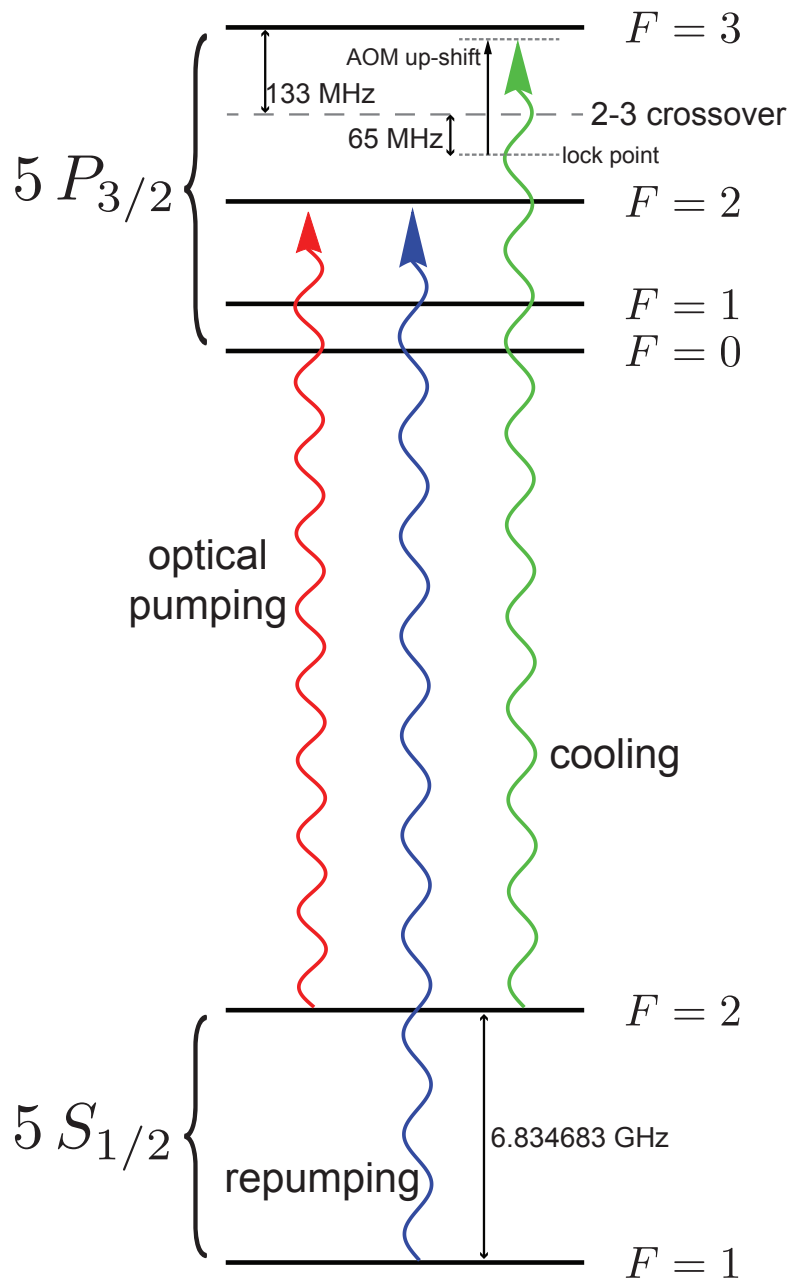


Figure 2.8: D<sub>2</sub> level structure for <sup>87</sup>Rb with lasers for cooling, repumping, and optical pumping drawn between appropriate states. The 2 – 3 crossover represents a crossover transition due to saturation-free spectroscopy and is discussed in Sec. 2.3.1.

however, is asymmetric about the resonance frequency, and the PDH lock measures the phase through a clever scheme of interfering sidebands with the carrier.

Rather than lock to an optical cavity, we send the beam through a rubidium vapor cell and perform saturated absorption spectroscopy to find our lock point (see Fig. 2.9<sup>2</sup>). Saturated absorption spectroscopy eliminates Doppler broadening in the vapor cell, which can smear out natural atomic linewidths of a few MHz to hundreds of MHz [91]. Two beams are required for this purpose, one for probing and detecting the absorption spectrum, and another, stronger beam to pump and saturate the atoms. This pump beam burns a so-called hole in the spectrum by exciting atoms with velocity  $v = (\omega_{\text{pump}} - \omega_0)/k$ , so that near atomic resonance it interacts with atoms moving with velocity  $v \approx 0$  relative to the beam direction [91]. When the probe beam is also tuned to resonance, it sees fewer atoms in the ground state, decreasing absorption at this frequency. The spectral width of this hole is given by the power-broadened natural linewidth of the atom in the absence of inhomogenous broadening from magnetic fields and light shifts, as Doppler effects are eliminated due to this selection of only the atoms at a particular velocity. Because the linewidth of our Toptica laser is much narrower ( $\lesssim 100$  kHz) than the atomic transition linewidth, we can resolve the hyperfine resonances by these holes in the absorption.



In addition to the hyperfine states, saturation spectroscopy produces cross-over transitions midway between the “real” transitions [91] (the dotted line in Fig. 2.8 indicates one such transition, the  $2 - 3$  crossover). We use the  $2 - 3$  cross-over

---

<sup>2</sup>This and many other figures in this thesis were made with the help of ComponentLibrary by Alexander Franzen, under the Creative Commons Attribution-NonCommercial 3.0 Unported License.

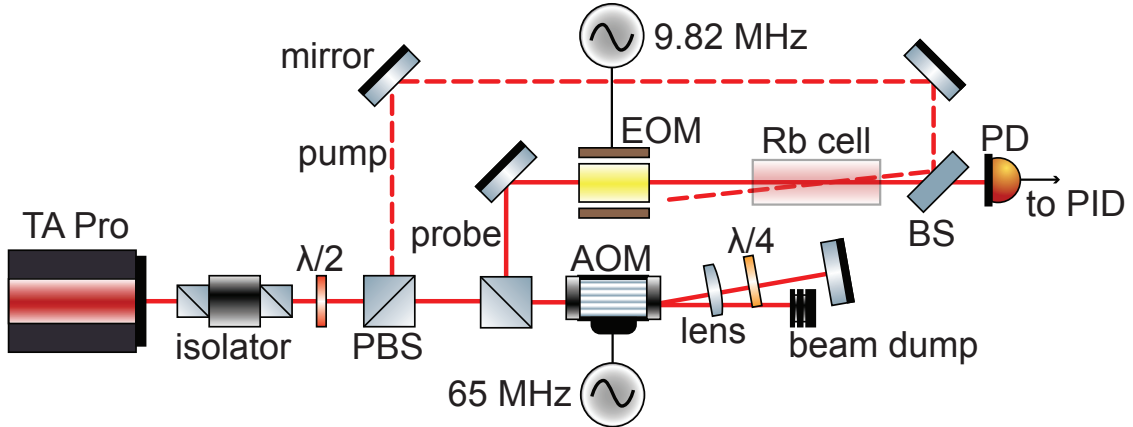


Figure 2.9: Schematic of the optics to perform saturated spectroscopy and Pound-Drever-Hall locking of the cooling laser. Note that the probe beam is up-shifted by 130 MHz relative to the pump beam.

transition for our lock point, which sits 133.3 MHz to the red of the  $F = 2 - F' = 3$  cycling transition. The contributions from both the  $F' = 2, 3$  levels make it the strongest peak in the spectrum, and it also gives us a nice point to work from using AOMs. In our setup, we upshift *only* the probe beam (see Fig. 2.9) with a double-passed AOM by  $2 \times \Omega_{\text{AOM}}/2\pi = 2 \times 65 \text{ MHz}$ . This scheme will burn the saturated holes discussed above at effective cross-overs between pump and probe, i.e.  $\omega_{\text{laser}} + \Omega_{\text{AOM}}$ . Thus in order for these cross-overs to be resonant with the atomic transition, the laser will sit at a frequency  $\omega_{\text{laser}} = \omega_{2-3} - \Omega_{\text{AOM}}$ , where  $\omega_{2-3}/2\pi$  is the frequency of the  $2 - 3$  cross-over transition, as indicated in Fig. 2.8. Therefore the laser is tuned 198 MHz to the red of the cycling transition, and a double-passed, tunable, 100-MHz AOM can bring the MOT and probing beams to the appropriate detuning.

An EOM phase-modulates the probe at 9.82 MHz, and we use this same RF frequency to demodulate the saturated spectroscopy signal (see Fig. 2.10). The

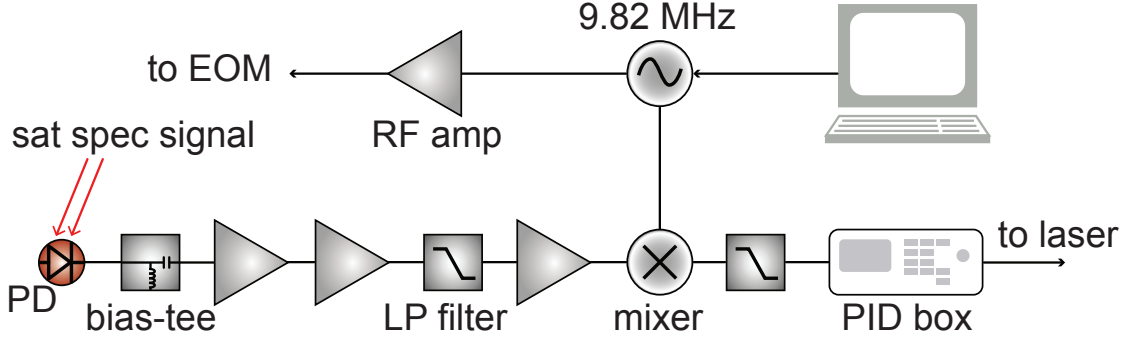


Figure 2.10: Schematic of the electronics to perform Pound-Drever-Hall locking of the cooling laser. The saturated spectroscopy signal is amplified and then mixed down with the same signal that dithers the EOM.

mixed-down signal is then sent to a lock box (Newport LB1005), and fed back to the laser piezo to stabilize its frequency.

### 2.3.2 Repump laser: Doppler-free DAVLL

While the cooling transition is to a reasonable extent a closed cycling transition, there is a nonzero probability for the atom to be excited to the  $F' = 2$  state, allowing it to decay to the  $F = 1$  state in the ground-state manifold. Here the atom is dark to the MOT laser, and no further cooling occurs. In order to remove the atoms that have fallen into this dark state, we add a second laser (Toptica DL Pro) tuned between  $F = 1$  and  $F' = 2$  to repump the atoms back into the cycling transition (see Fig. 2.8).

To lock the repump laser we employ a variation of the dichroic atomic vapor laser lock (DAVLL) [92, 93] that uses saturated spectroscopy to narrow the locking transition [94]. The DAVLL utilizes the Faraday effect [95] with a magnetic field along the direction of light propagation in an atomic vapor to generate an error

signal, without the need for additional RF electronics. Linearly-polarized light can be decomposed into left- and right-circularly polarized components,  $\sigma^-$  and  $\sigma^+$ , respectively. When a resonant, linearly-polarized beam is sent through an atomic medium, these two circular components are degenerate, and a magnetic field applied along the direction of propagation lifts this degeneracy through the Zeeman effect. Applying this field along the axis of propagation (as in Fig. 2.11) shifts the absorption curve of each component, creating elliptically polarized light at the output with phase difference given by [95]

$$\varphi \simeq \frac{2g\mu B/\hbar\Gamma}{1 + (2g\mu B/\hbar\Gamma)^2} \frac{l}{l_0}, \quad (2.2)$$

where  $B$  is the magnitude of the applied field,  $\Gamma$  is the width of resonance peak,  $g$  is the Landé factor,  $\mu$  is the Bohr magneton,  $l$  is the length of the sample, and  $l_0$  is the absorption length. We separate these components with a quarter-wave plate and Wollaston prism, and subtracting the photodetector signals yields a dispersive curve for locking. Optimal fields for creating a linear error signal near resonance occur when the equality  $2g\mu B/\hbar = \Gamma$  holds, and the Doppler-free DAVLL scheme requires smaller fields to shift the narrower resonances. We find that a chain of permanent magnets appropriately oriented near the rubidium cell is sufficient to produce a stable error signal.

Other groups have found ~~that~~ too much temperature dependence that was linked to the polarization beam splitters, which is one reason why we use a Wollaston prism at the output, after the atoms have rotated the light polarization (the input is

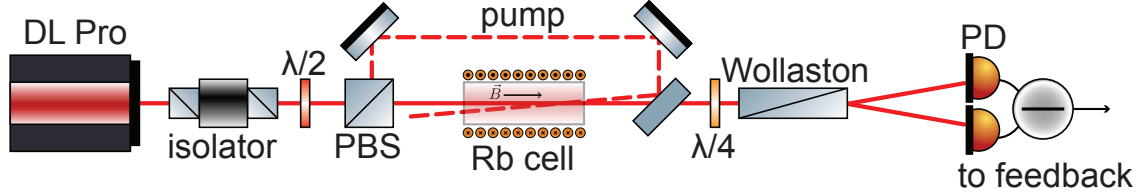


Figure 2.11: Schematic of the optics for the DAVLL for the repump laser. The magnetic field points in the direction of propagation of the probe beam.

less sensitive). The optical setup is covered with a plastic box to shield air currents and to help maintain stable temperatures, as temperature changes can indeed affect the field from the permanent magnets.

### 2.3.3 Nanofiber “blue” laser: Ti:Sapph

We use a Ti:Sapph laser tuned to 750 nm to produce the repulsive, blue-detuned beam for our nanofiber trap. This system consists of a tunable, ring cavity Ti:Sapph (Coherent 899-01) free-running but with thick and thin etalons, pumped by a 10-W, 532-nm beam (Coherent Verdi-V10). The large cavity length of the Ti:Sapph reduces the amount of ASE in the beam relative to a diode laser, which helps when filtering background in front of our detection SPCMs. Additionally, high output powers of hundreds of mW ensure that we have a suitable range of power at the nanofiber waist even after heavy filtering. The wide frequency tunability (from  $\sim 720 - 810$  nm) allowed us to rule out Raman gain in the silica as the cause of the background light we detect in the optical fiber, and we instead think it is likely fluorescence from impurities.

### 2.3.4 Nanofiber “red” laser: Nd:YAG

An Nd:YAG laser (JDSU NPRO-126N-1064-100) generates the 1064-nm beam to create the attractive potential for the nanofiber trap. The NPRO laser is based on a monolithic design that ensures narrow linewidth, excellent stability, and Gaussian optical modes ( $M^2 \approx 1$ ), which allows for highly efficient fiber-coupling and AOM diffraction, leaving us with the requisite few mW per beam to generate the standing-wave potential along the nanofiber. Moreover, the low intensity noise ( $< 0.05\%$  rms for frequencies between 10 Hz to 2 MHz, and  $< -165$  dB/Hz above 10 MHz) minimizes heating in the trap. The two beams for each leg of the standing wave are up-shifted by 80 MHz using two AOMs, and the RF signals to each AOM are phase-locked. We can control the relative frequency of these two beams to create an optical “conveyor belt” along the nanofiber to transport atoms.

## 2.4 UHV system

Cold-atom experiments require an environment devoid of other gases, as collisions with these particles limit the amount of time that atoms will remain trapped. To this end the experiments are performed in UHV systems, where pressures less than  $10^{-9}$  mbar are easily achievable. Because these systems are commonplace in AMO laboratories, in this section we outline only the characteristic features of our UHV apparatus.



Figure 2.12: Photograph of UHV science chamber before coil installation. Visible are the large, AR-coated windows and the washer mount described in Sec. 2.4.2 to attach the chamber to the table.

#### 2.4.1 Science chamber

A SS chamber (Kimball Physics MCF800-SphSq-G2E4C4A16) with a range of CF flange sizes forms our science chamber (see Fig. 2.12). Viewports on either side are AR coated (Rocky Mountain Instruments) for 780-nm light, and their large size affords us generous optical access to the chamber for MOT beams, imaging, optical pumping, and other probes. A reentrant viewport (MPF Products, Inc.) on the top of the chamber provides an orthogonal imaging direction, decreasing the working distance from about 111 mm to 60 mm.

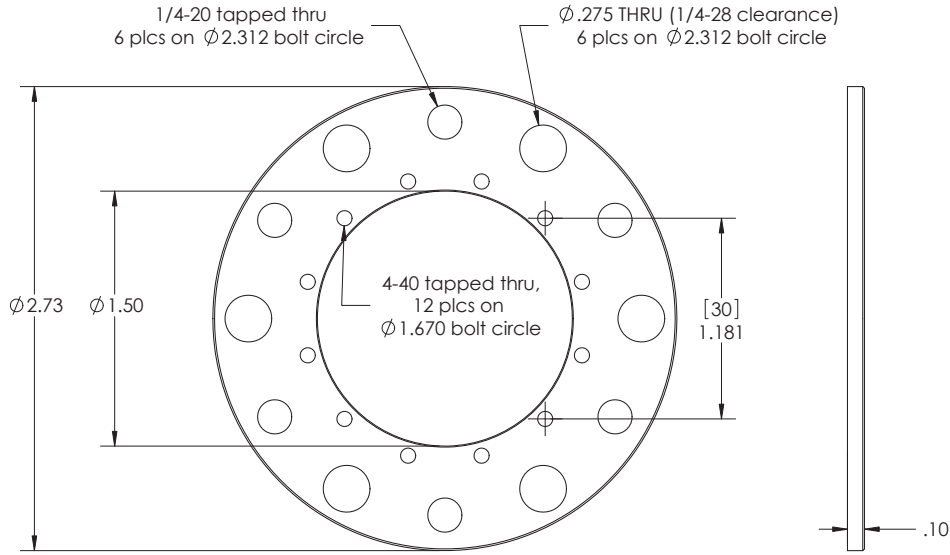


Figure 2.13: Drawing of special washer to attach 30-mm cage-mounts from Thorlabs to a 2 3/4" CF flange, adapted from the original design of Creston Herold.

#### 2.4.2 Washer optics mounts

Creston Herold from the JQI Ultracold Mixtures group of Trey Porto and Steve Rolston designed large, SS washers that allow cage-mount optics from Thorlabs to be mounted directly to CF flanges. We use some of his designs (see Fig. 2.13) to mount four of MOT beams to our science chamber, and we built off the idea to make a washer to mount the entire chamber to the optical table (Fig. 2.14, and visible in Fig. 2.12). These optics mounts greatly simplify the alignment of these four crossed MOT beams, as well as free up space on the optical table.

#### 2.4.3 Ion pump placement

Efficient devices that achieve and maintain UHV conditions with no moving parts, ion pumps rely on a high voltage and an electron current to ionize residual

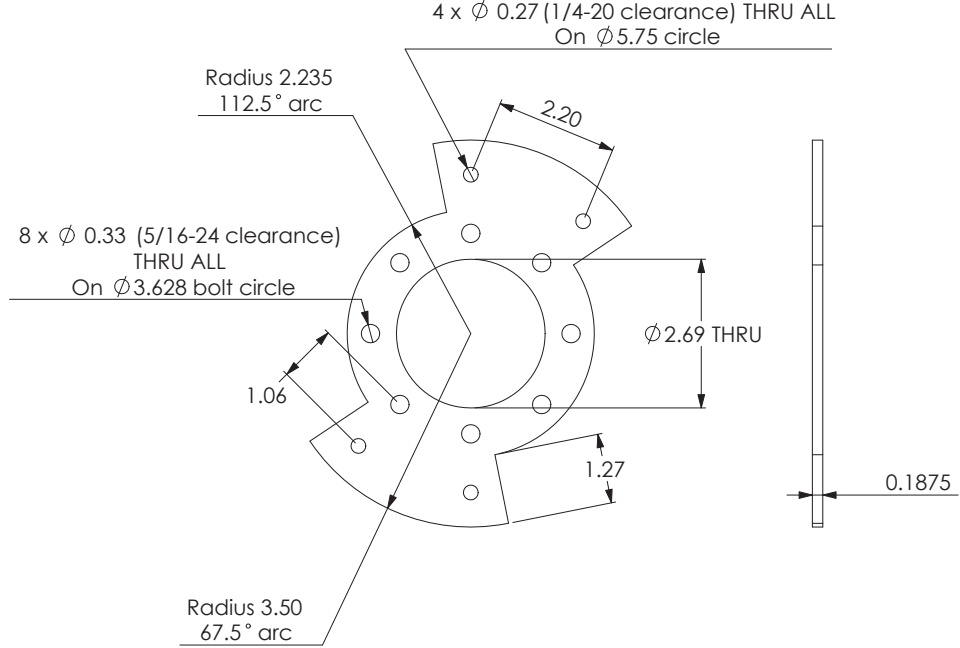


Figure 2.14: Drawing of special washer to attach the 4 1/2" CF flange of our science chamber to the optical table on 1" and 1.5" optical posts.

gas particles that diffuse near their entrance. The high voltage and magnetic field are not sufficient to direct all of the residual electrons and/or ions to the titanium, and some escape to produce a current on the order of a few pico amps [96]. We find that if the nanofiber is placed within the line-of-sight of an ion pump, these leakage currents cause charge buildup on the nanofiber, which eventually breaks under strain from external electric fields. We circumvent this issue by inserting 90° vacuum elbows between the ion pumps and the science chamber so that the leakage currents “see” a grounded surface rather than the nanofiber. As a further precautionary measure, we place protective vacuum screens (Pfeiffer PM 016 333) within the pump CF flange, offering another grounded surface on which to discharge the leakage current without adversely affecting the conductance of the pump.

#### 2.4.4 Manipulator

We added to the science chamber a load-lock system that facilitates quick transfer of samples into UHV. A 6" cube (MDC Vacuum 408004) serves as the antechamber, separated from the science region by a 2 1/2" all-metal gate valve (MDC Vacuum 302002), chosen so that the bore can accommodate mounted nanofibers (see Fig. 2.15). Attached to the antechamber is an UHV-compatible manipulator (VG Scienta Transax), which has 450 mm of translation parallel to the optical table and 25 mm of (radial) motion in the transverse plane. A stepper motor provides quick motion in the parallel direction, and manual micrometers position the manipulator transversally. Due to the large torque exerted on the mounting flange, the manipulator is counter-balanced by a pulley system attached to a bucket of steel balls on the side of the table. The manipulator has proven useful when interchanging various GMOT prototypes and when nanofibers continually broke during the beginning attempts at transferring them into UHV. One shortcoming of the system, however, is the long lever arm of the support rod to which samples are mounted, as it couples external vibrations to the nanofiber.

#### 2.4.5 Nanofiber mount

Post-pull, a nanofiber must be mounted to a rigid structure before being moved, as its thin diameter leaves it susceptible to breaking from shearing forces. The mounts typically have a "U" shape, and the nanofiber is glued with UV-curing epoxy to the vertical sections of the U. Fig. 2.16 is a photograph of our mount, dis-

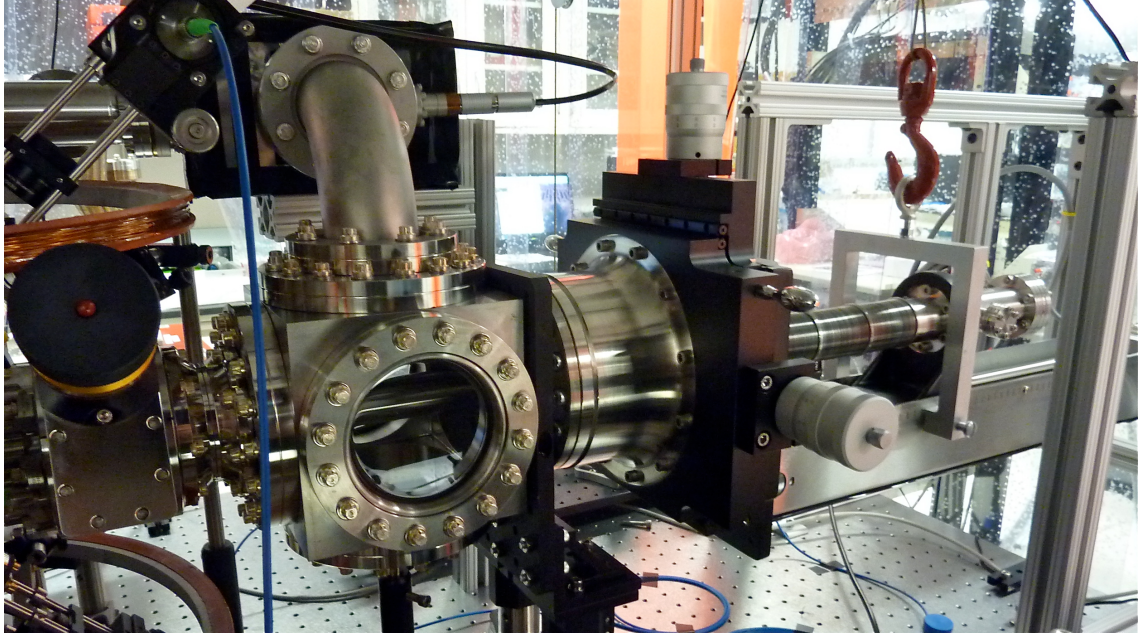


Figure 2.15: Photograph of UHV manipulator attached to science chamber via a gate valve. Note the ion pump placed at a right angle relative to the antechamber to prevent the breaking of fibers.

playing the characteristic shape and the hollowed-out section on the bottom through which MOT light can pass. It is made of a titanium alloy because it is machinable, lighter than steel (less deflection of the manipulator support rod), non-magnetic, and has a conductivity ( $\sigma = 2.38 \times 10^6 \text{ S} \cdot \text{m}^{-1}$ ) 15 times smaller than that of aluminum to lessen eddy currents when the MOT coils turn off.

## 2.5 Magnetic field control

Forming a MOT requires cancellation of spurious external magnetic fields, as well as the generation of a linear magnetic gradient at the trap location. To this end we use three pairs of coils with separation between their radius and their diameter that produce a roughly uniform magnetic field at the center in three orthogonal directions for cancellation, and two coils where each field points towards the center

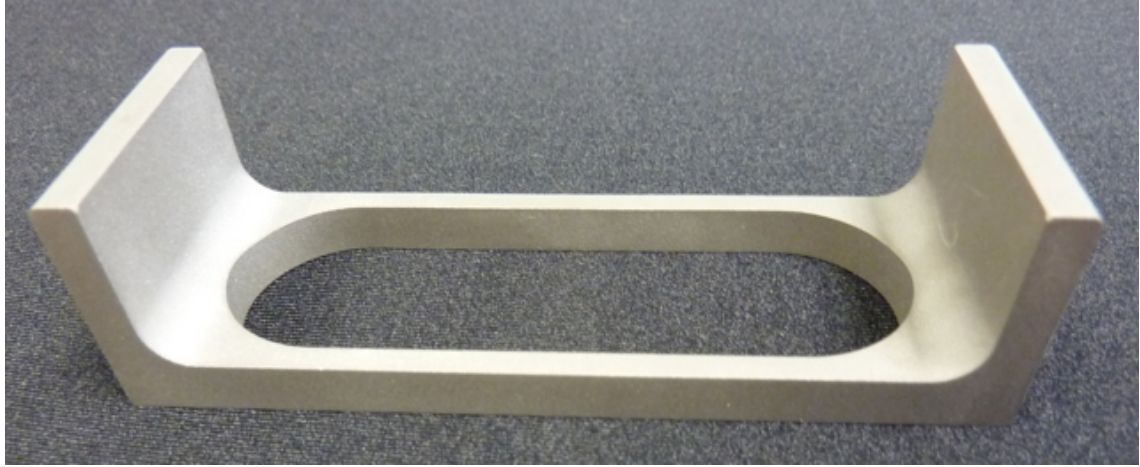


Figure 2.16: Titanium nanofiber holder for UHV.

to make the gradient. This section presents the specifications for these coils and an overview of the circuitry that drives their currents.

### 2.5.1 MOT coils

Each coil for the gradient magnetic field consists of 22 turns of rectangular wire with cross-sectional dimensions of  $0.191'' \times 0.481''$ . The large thermal mass of the coils allow us to run high (up to 90 A) currents for long periods of time without the need for water cooling. The coils have an inner diameter of approximately 8" and are separated by 7", and typical currents (30 – 90 A) generate gradients between  $5 - 15 \text{ G} \cdot \text{cm}^{-1}$ . We supply them with current via a high-current power supply (Electronic Measurements Inc. TCR Power Supply, DC-200A), connected by 4-AWG, super-flexible welding cable.

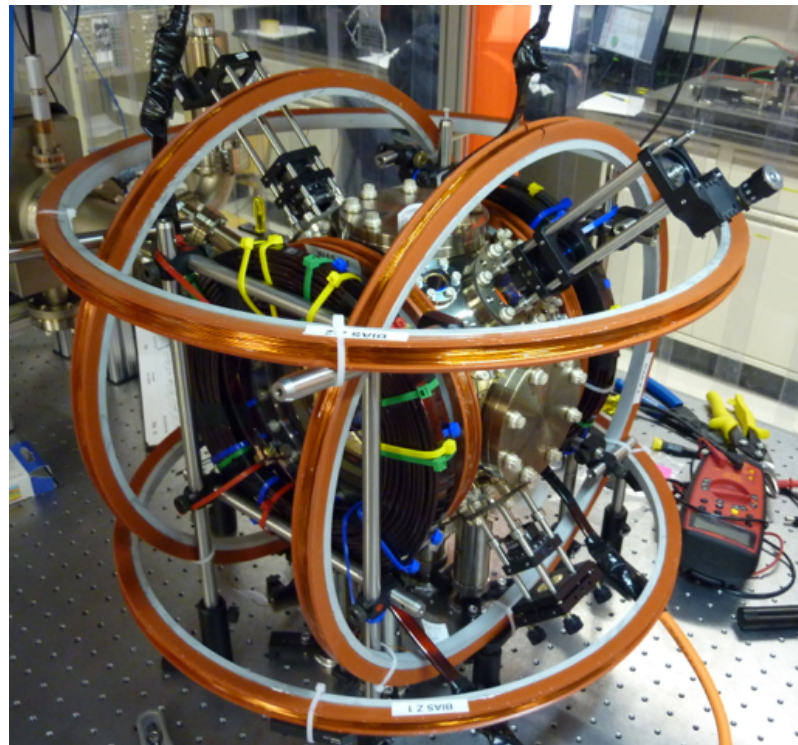


Figure 2.17: Photograph of science chamber with all three pairs shim coils and gradient coils (dark maroon with rainbow cable ties) installed. Also visible are the MOT beam optics mounted to the special CF washers from Sec. 2.4.2.

### 2.5.2 MOT coil PID

The 4 AWG welding cables that run from the power supply to the coils pass through two Hall sensors (F. W. Bell, CLSM-1000), which sense the current running through the cables. One Hall sensor acts as a monitor for diagnostic purposes, while the other is sent to a PID servo that stabilizes the current. Four high-current MOSFETs (E250NS10) for switching fields on and off are arranged in parallel to distribute the current in order to prolong the life of the MOSFETs. These are heat sunk to a thermal exchange plate with copper pipe running through it for water cooling. The thermal exchange plate is then mounted to a large (2" in. fins) heat sink, and a fan constantly blows air over the circuit. With all of these precautions, the devices stay below 50° C when running up to 100 A.

### 2.5.3 Shim coils

The shim coils consists of 100 turns each of 22 AWG wire around circular aluminum forms. Table 2.2 lists the dimensions, resistances, and inductances of the three pairs of coils in orthogonal directions. X refers to the axis perpendicular to the MOT coils, Y is the axis along the MOT coils, and Z is the vertical axis relative to the optical table (see Fig. 2.17). One experimental shortcoming is the use of continuous aluminum forms to hold the coils, as they can carry eddy currents when changing fields quickly. This can be ameliorated by cutting a gap into the aluminum so there is no continuous path for current to flow, but we have not found this to be necessary given the typical timescales and currents in our experiment.

Direction	Inner radius (in.)	Separation (in.)	Resistance each coil (ohm)	Inductance each coil (mH)
X	8	8 11/16	6.9, 7.0	5.10, 4.08
Y	4	5 13/16	3.4, 3.4	2.65, 2.61
Z	9	11 1/2	7.6, 7.7	5.68, 5.85

Table 2.2: Dimensions, resistances, and inductances of three shim coils used to cancel spurious fields in our system.

### 2.5.4 Shim coil driver

A high-voltage, high-current op-amp (Texas Instruments OPA549T) drives each of the shim coils. Because they are all drawing current from the same, 6-A power supply, each op-amp is limited to 2 A with a clamping resistor. We set the current with analog outputs from our DAQ cards (see Sec. 2.8.1), with the output current varying linearly with the voltage set point.

## 2.6 Optics

This section briefly discusses the two imaging systems used to diagnose and align our atom cloud, as well as the optics used to generate our trapping beams.

### 2.6.1 Imaging

Two cameras (Point Grey, Flea3 FW-03S1M-C, 5.6  $\mu$ m pixels, 648x488 array) positioned in roughly orthogonal directions allow us to measure atom cloud temperature, as well as the relative position between nanofiber and cloud. The Flea3 is compact and triggerable, allowing it to be synchronized to our experimental timing

sequences. The camera mounted in the horizontal direction has a magnification of 0.4, verified by tracking the position of a cloud falling under the influence of gravity and by imaging well-known lines on the 1951 USAF test pattern. Demagnifying affords us more expansion time in TOF measurements before the cloud size exceeds that of the CCD.

The vertical imaging system is a standard  $f - 2f - f$  relay configuration, with pairs of matched 100-mm achromat lenses (Thorlabs MAP10100100-B) for each leg of the relay, as shown in Fig. 2.18. An adjustable iris halfway between the two sets of matched pairs can filter stray light from the chamber. There is a lens-tube-compatible tray housing a 780-nm bandpass filter that can be easily removed if other wavelengths need to be imaged. Because the filter is not placed between the matched pairs, its presence or absence shifts the imaging system focal length, which we can adjust using a micrometer stage to which the whole setup is attached. We also added a 70:30 (R:T) beamsplitter to send light in two orthogonal directions, one for imaging and the other for a polarization-dependent measurement. The linear polarizer and photodetector in transmission allow us to determine polarization of light on the nanofiber waist by detecting Rayleigh scattering (discussed further in Chap. 3). This detection system is also easily removable, and we have interchanged it with a multimode fiber coupler to send photons to an SPCM for free-space atomic lifetime measurements (see Chap. 5).

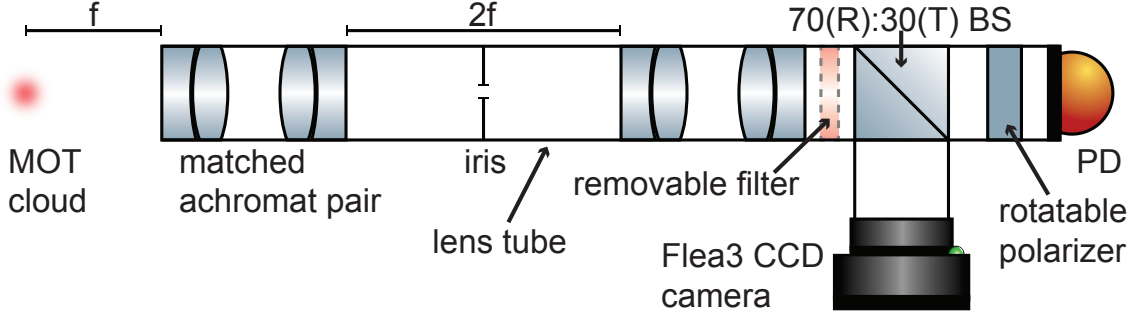


Figure 2.18: Schematic of the vertical imaging system (rotated 90 degrees for clarity). The collected light is split in a 70:30 ratio in reflection (R) and transmission (T) by a beamsplitter (Thorlabs BS023) to divide light between an imaging CCD and a polarization-sensitive photodetector. The filter (dashed lines) is easily removable.

## 2.6.2 MOT beams

MOT and repump light are coupled into a 2-to-3 PM fiber splitter (Evanescence Optics), with even splitting of the MOT beam and a ratio of 4:1:1 for the repump beam. In this way, both beams are spatially overlapped when sent into the chamber. A 75-mm focal length achromat lens (Thorlabs AC254-075-B-ML) directly collimates the output from PM fiber, achieving a waist diameter of approximately 13.5 mm. At the initial peak of the MOT laser's performance, we could send up to 40 mW per beam, but after a few years of use we typically have 19 mW ( $I = 13.3 \text{ mW} \cdot \text{cm}^{-2}$ ) per beam, which is sufficient for cooling atoms.

## 2.7 Photon counting

Due to small mode area of the evanescent field outside of the nanofiber waist, the saturation power of atoms trapped there is very small, on the order of tens of picowatts or less. We use SPCMs (Laser Components COUNT-250C) operating in

Geiger mode to detect these low light levels. We have three modules on the optical table, each with dark counts lower than the specified  $250 \text{ counts}\cdot\text{s}^{-1}$ . The photon detection efficiency at 780 nm is  $\gtrsim 60\%$ , and the chips have pre-aligned GRIN lenses to efficiently couple multimode fibers. Black-clad fibers prevent stray room light from coupling into the fibers and reaching the detectors.

The SPCMs output a transistor-transistor logic (TTL) pulse for each incident photon (afterpulsing probability is less than 0.2%), making photon counting easy. We use field-programmable gate arrays (FPGAs) for this purpose; one operates as a MCS and the other time-tags and correlates clicks. The multichannel scaler (MCS) FPGA (National Instruments 779363-01) interfaces with a LabView software developed by Michael Tandecki of the FrPNC collaboration and expanded and modified in our lab. We can set bin widths as narrow as 12.5 ns and as wide as 3.2 ms, offering wide functionality. This module is primarily used for nanofiber absorption measurements (see Chap. 3), as we can see shot-to-shot experimental runs to diagnose the quality of our nanofiber trap before accumulating histograms for analysis.

The second FPGA (KNJN Xylo-EM) uses firmware, C++ code, and LabView VIs written by Joffrey Peters and Sergey Polyakov at NIST Gaithersburg<sup>3</sup>. An internal clock of 48 MHz sets a 21.83 ns window for performing photon coincidence or time-tagging measurements. We used this setup to record the data presented in Chap. 4.

Finally, we sometimes use a digital oscilloscope (Tektronix DPO7054) for pho-

---

<sup>3</sup>See <http://www.nist.gov/pml/div684/grp03/multicoincidence.cfm> for documentation and all necessary downloads.

ton counting measurements requiring finer time resolution. Working in its fast acquisition mode, we can histogram clicks with bin sizes as low as 100 ps. We used this oscilloscope with a bin size of 1 ns to acquire the data in Ch. 5.

## 2.8 Electronics and control

Experimental sequences are controlled via a program written in LabView by JQI Fellows Trey Porto and Ian Spielman (and continually updated by students) called CycleX. It is a highly configurable interface that can set digital and analog line levels, as well as set ramps based on common functions (e.g. linear, exponential, Blackman, etc.).

### 2.8.1 Timing and DAQ cards

A PulseBlaster (SpinCore PB24-100-32k) with 24 digital lines determines the clock of the experiment. The internal 100 MHz clock sets a minimum timing resolution of 10 ns. Each additional DAQ card in the control system has a PulseBlaster channel fed into a PFI input to sync their clocks with that of the PulseBlaster. Additional lines from the PulseBlaster are used as triggers within an experimental sequence, but only for devices that do not need to hold TTL HIGH when a cycle finishes, as a firmware upgrade to the PulseBlaster sets all channels to TTL LOW at the end of a cycle.

Three DAQ cards (National Instruments PCIe-6353, PCI-6733 (x2)) provide the other digital triggering lines and analog levels. They offer a total of 20, 16-bit

analog output channels for setting, e.g., coil currents and AOM RF powers. An external box of analog buffers (Texas Instruments BUF634P) allows these channels to drive  $50\ \Omega$  loads. A small fraction of the available digital lines are broken out from the DAQ cards so that some devices can receive logical HIGH even when the cycle stops.

RF signals up to 171 MHz originate from three, four-channel direct digital synthesis (DDS) boxes (Novatech 409B-AC) to drive our AOMs. Signals within each Novatech are phase-synchronized, which is important for the AOMs that set the frequency for the 1064-nm beams of the nanofiber trap. Frequencies on two of the channels in each box can be changed in steps as small as  $100\ \mu\text{s}$ ; faster switching will require a voltage-controlled oscillator.

## 2.9 Conclusions: improvements and laboratory relocation

Soon the laboratory will relocate to the basement of the new Physical Sciences Center. This move will offer numerous improvements simply by virtue of the new location. The humidity and temperature control of the new space will eliminate the frequent realignments we must carry out in the current lab; even over the course of a few hours we can detect marked polarization drift in our nanofiber trap. Dismantling and reassembling things will also grant us the opportunity to upgrade some part of the apparatus during the down time. Most notably will be a new fiber with an optimized waist diameter for  $^{87}\text{Rb}$  (see the end of Chap. 5) and a new UHV mount that will eliminate vibrations that affect trap loading (see Appendix B).

## Chapter 3: Optical nanofiber trap

### 3.1 Introduction

The small mode volume of evanescent field atom traps engenders strong atom-light interactions without the need for a cavity [97]. The recent demonstration of trapping  $^{133}\text{Cs}$  with an optical nanofiber (ONF) [21, 23] - and a state-insensitive variant [22] - mark an important experimental realization of these systems. Their high optical depth (*OD*) allows for efficient dispersive readout [98] and strong non-linear interactions. The regime of strong coupling opens the door to the study of long-range interactions and the formation of so-called atomic mirrors [99] or the observation of self-crystallization [100, 101]. Furthermore, these ONFs are a crucial element of our proposed hybrid quantum system to couple atoms to superconducting circuit elements [49, 61, 64].

Optical dipole trapping of atoms is a well-developed technology applied to numerous atomic species. The extension of optical trapping to evanescent fields of an ONF shares similarities with dipole trapping with free space beams, but has one distinction - the evanescent field may have a substantial longitudinally polarized component of the electric field. This can lead to surprisingly large differences in the absorption of probe light for two different species, even when they are both alkali

atoms (e.g. Rb and Cs), due to the effects of the vector light shift.

Our system traps atoms with two lasers, achieving trap depths of a few hundreds of microKelvin. We cannot simply determine atom number by the absorption of a probe beam by an optically thick medium with a Lorentzian line shape. Distinct asymmetries are observed that we trace to the effects of the vector light shifts associated with the optical trapping fields, and their inherent elliptical polarization with an appreciable component along the direction of propagation. Although Rb and Cs are nominally atoms with very similar atomic structure, the light shifts can in fact be quite different, with differential light shifts much larger in Rb than Cs, leading to a modified absorption profile.

This chapter is organized as follows. Sec. 3.2 outlines the experimental setup. We present experimental confirmation of our trap in Sec. 3.3. We introduce a theoretical model based on light shifts, finite atom temperature, and population redistribution in Sec. 3.4, and use it to study the inhomogeneous absorption profile. Sec. 3.5 summarizes our findings and provides an experimental outlook.

## 3.2 Setup

The data presented in this section are taken using an ONF with a waist diameter of  $500 \pm 50$  nm and length of 7 mm, with tapering regions of 28 mm in length. A MOT loaded from a background vapor of  $^{87}\text{Rb}$  produces a cloud of  $\sim 10^8$  atoms. We overlap the cloud with the ONF waist using magnetic field shim coils and the UHV manipulator. Two orthogonal imaging systems ensure alignment. Atoms fall

into the ONF trap (on throughout the experiment) after 90 ms of increased MOT detuning and a 1-ms-duration optical molasses stage. The sub-Doppler cooling during this loading stage yields MOT temperatures of  $\sim 15 \mu K$ , as determined by TOF measurements.

An ONF trap requires light tuned red of resonance (with respect to the  $^{87}\text{Rb}$   $D_2$  line) to provide an attractive potential and light tuned blue of resonance to prevent atoms from striking the ONF surface (see Fig. 3.1). A 750 nm wavelength laser provides the repulsive force, and a 1064 nm wavelength beam in a standing wave configuration (to produce longitudinal confinement) provides the attractive potential. A potential minimum of a few hundred  $\mu K$  in depth is formed  $\sim 200$  nm from the fiber surface, as calculated with a simple two level atom and only scalar shifts (see Fig. 3.1 (e)). The 750-nm beam and the near-resonant probe beam are intensity-stabilized. The lock for the probe beam requires a sample-and-hold system to maintain stable powers when pulsed on for short (10  $\mu$ s to 10 ms) times.

To verify the polarization of each beam on the nanofiber waist, we take polarization-sensitive measurements of Rayleigh scattering from the waist using the system in Fig. 2.18 [22, 102]. Fig. 3.2 displays one instance of this measurement for a 1064-nm beam, utilizing the CCD camera instead of the PD. We rotate a HWP before the input of the nanofiber to vary the input polarization of the light, and we then image the Rayleigh scattering as this polarization changes. The contrast in the oscillations of the Rayleigh scattering gives the degree to which the light is linearly polarized (which we optimize with other bulk optics). Using the CCD camera and integrating over 280- $\mu$ m regions allowed us to confirm that polarization does not

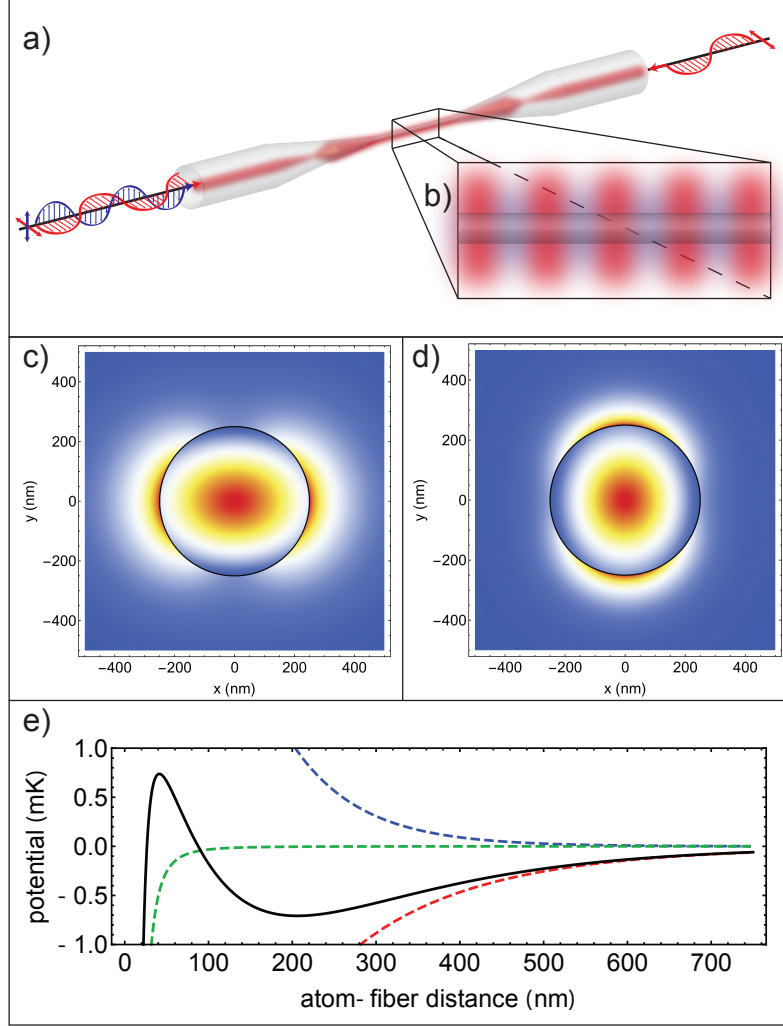


Figure 3.1: (a) Schematic of ONF with counter-propagating 1064-nm beams and an orthogonally-polarized 750-nm beam. (b) Illustration of potential at the ONF waist with lattice formed by 1064-nm beams. (c) Intensity plot of 1 mW of linearly-polarized, 1064-nm light in an ONF with diameter 500 nm. The color scale indicates increasing intensity from blue to red. (d) Intensity profile of vertically-polarized 750-nm light through the same ONF. (e) Total trapping potential (black) for a 500-nm diameter ONF with contributions from 3 mW in each 1064-nm beam (red dashed), 6.5 mW of 750-nm power (blue dashed), and van der Waals (green dashed). The potentials are calculated from only the scalar shifts. (figure adapted from Ref. [78])

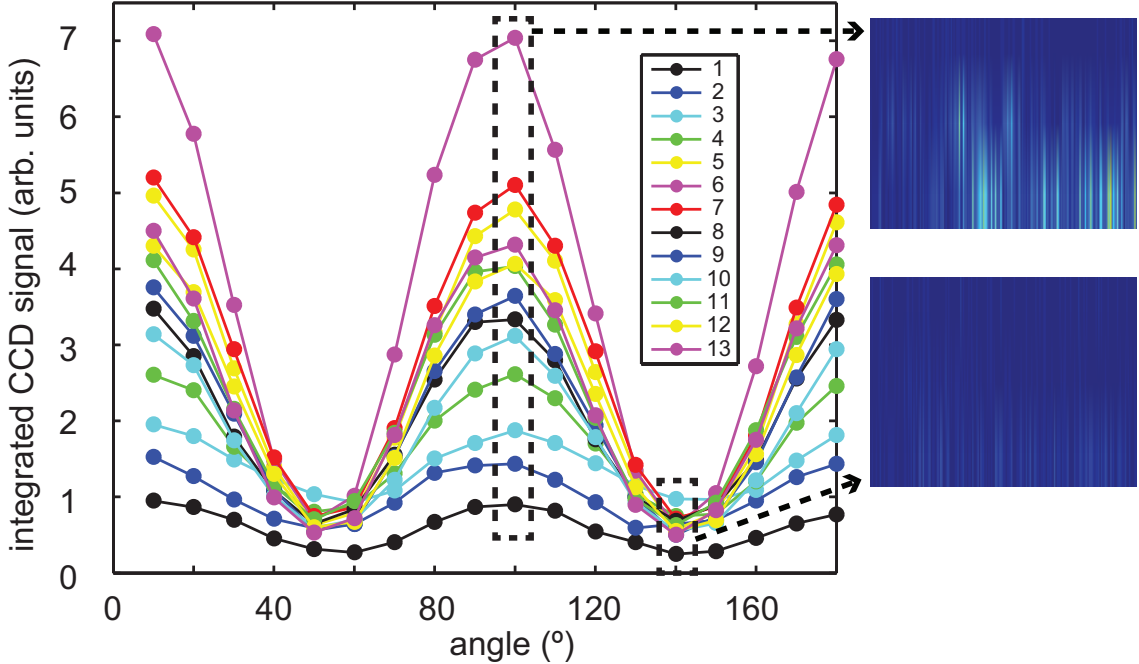


Figure 3.2: An example of the characterization of Rayleigh scattering to determine polarization of 1064-nm light on the nanofiber waist. The integrated CCD signal is plotted as a function of input HWP angle for 13 regions spanning about 3.6 mm of the nanofiber waist. The two pictures show the CCD images for the points outlined by the dashed boxes. The integration is performed along 13 vertical cuts of the images, each cut being 50 pixels (280  $\mu$ m) wide.

rotate over a length of 3.6 mm on the nanofiber waist. We then can confidently use just a PD for later polarization adjustments, as this will integrate the signal over that entire 3.6 mm length.

We measure atomic absorption with a weak, near-resonance beam (780 nm) coupled through the ONF, counting transmitted photons with SPCMs. Because light levels near 10 pW saturate the APDs, great care must be taken to filter stray light and maintain low probe power. Three narrow-line volume Bragg gratings (VBG, OptiGrate BP-785, 0.01 pm bandwidth at 785 nm) filter amplified spontaneous emission from the Ti:Sapphire laser near 780 nm. A fourth VBG at the output

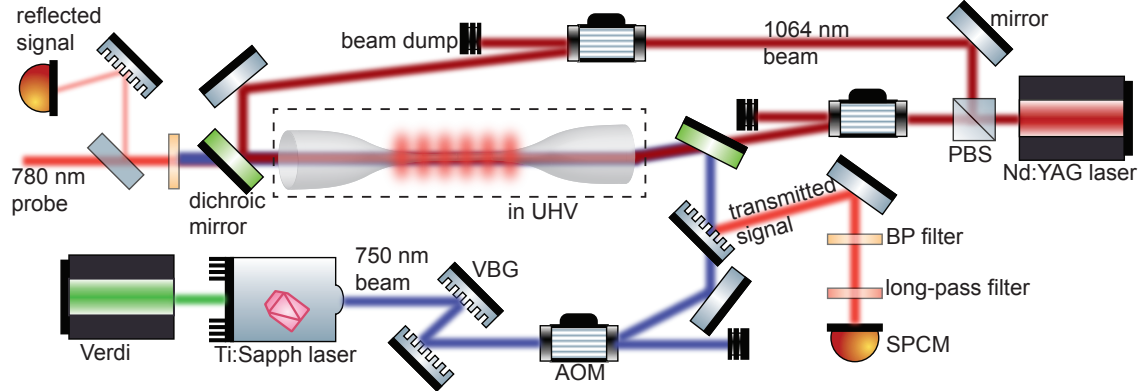


Figure 3.3: Experimental schematic. Beams from the Nd:YAG laser (1064 nm) and the Ti:Sapph laser (750 nm) are coupled onto the nanofiber using dichroic mirrors. Thru-fiber absorption signals are measured with SPCMs. Volume Bragg gratings (VBGs) offer narrow-line filtering of spurious background the Ti:Sapph laser as well as fluorescence from impurities in the fiber glass. See text for details.

of the nanofiber serves as a mirror to direct signal to the APDs and as another filter to block in-fiber background induced by the blue trapping beam. This light due to fluorescence from impurities in the glass is the main source of background in the experiment. Two more bandpass filters further reduce background counts, and finally long-pass color filters (Thorlabs, FGL645) directly in front of the APD fiber couplers reduce short-wavelength background from stray light. A series of ~~different optical depth~~ neutral density filters before and after the nanofiber allow us to vary the probe intensity while keeping light levels within the dynamic range of the APDs. TTL pulses from the APDs are counted with a FPGA and processed to extract absorption signals and full photon counting statistics.

### 3.3 Experiment

The absorption profiles are measured via an in-fiber analog of standard absorption spectroscopy. We use two probe pulses; the first pulse measures the atomic absorption signal ( $P_{at}$ ), and the second pulse is a reference signal with no atoms ( $P_0$ ). In between the two probe pulses, the 1064 nm trapping beam is turned off and a slightly blue-detuned laser from the MOT beam paths kicks away the trapped atoms. Based on the ratio of these probe signals, we calculate the measured transmission,

$$T = \frac{P_{at} - P_{bg}}{P_0 - P_{bg}}, \quad (3.1)$$

where  $P_{bg}$  is the background APD signal with no probe light, with contributions from detector dark counts and fiber-induced fluorescence. For a single Lorentzian lineshape with width  $\Gamma$ , one can easily estimate the optical depth  $OD$  by fitting the data to

$$T(\omega) = \exp \left[ -OD \frac{1}{1 + 4(\omega - \omega_0)^2 / \Gamma^2} \right], \quad (3.2)$$

where  $\omega_0$  is the angular frequency of a resonant photon. The total number  $N$  of trapped atoms is then given by  $OD/OD_1$ , where  $OD_1$  is the single-atom optical depth. We calculate  $OD_1$  to be  $\sim 2.8\%$  by comparing the atomic cross section to the optical nanofiber mode area. Fig. 3.4 displays a transmission spectrum, averaged over 50 experimental runs, where the probe detuning is given relative to the bare atomic resonance. Our measured transmission profile displays a markedly asymmetric lineshape. Because of this asymmetry it is not trivial to estimate the

number of trapped atoms. Note that the maximum absorption sets a lower limit on the OD and number of trapped atoms, i.e.  $OD_{low} = -\ln[T]$ . Based on our lowest transmission of 96.8% ( $OD = 3.44$ ) at a probe-detuning of 10 MHz, the absolute lower bound of trapped atom number is  $N = 123$ . Any broadening mechanisms only serve to reduce the maximum absorption for a given number of atoms. We will discuss this more in Sec. 3.4, where we develop a method to estimate the number of trapped atoms based on these asymmetric absorption profiles.

We perform the photon-counting equivalent of TOF imaging in this 1-dimensional geometry and observe trapping lifetimes (without any additional cooling) of approximately 23 ms (see Fig. 3.5). The lifetimes are shorter than expected based on background gas collisions, atom temperature, trap depth, and understood scattering rates. Ref. [103] observes fiber torsional modes of several hundreds of kilohertz, close to the trap frequencies of an ONF trap. They posit that this might be a source of parametric heating in these traps. While we have not studied in detail these modes in our system , do observe that our ONF can exhibit large-amplitude transverse vibrations near 550 Hz and the manipulator mount oscillates at a frequency of 28 Hz (see Chap. B). These are too low in frequency to cause parametric heating as the motion is adiabatic in terms of the optical trapping potential. The acceleration of the fiber, on the other hand, may be high enough at times to affect loading, as the macroscopic motion of the trap is no longer adiabatic relative to the mean atomic motion. This lifetime is typical of ONF traps, which are generally shorter-lived than standard optical dipole traps.

We also study two different polarization configurations of the red- and blue-

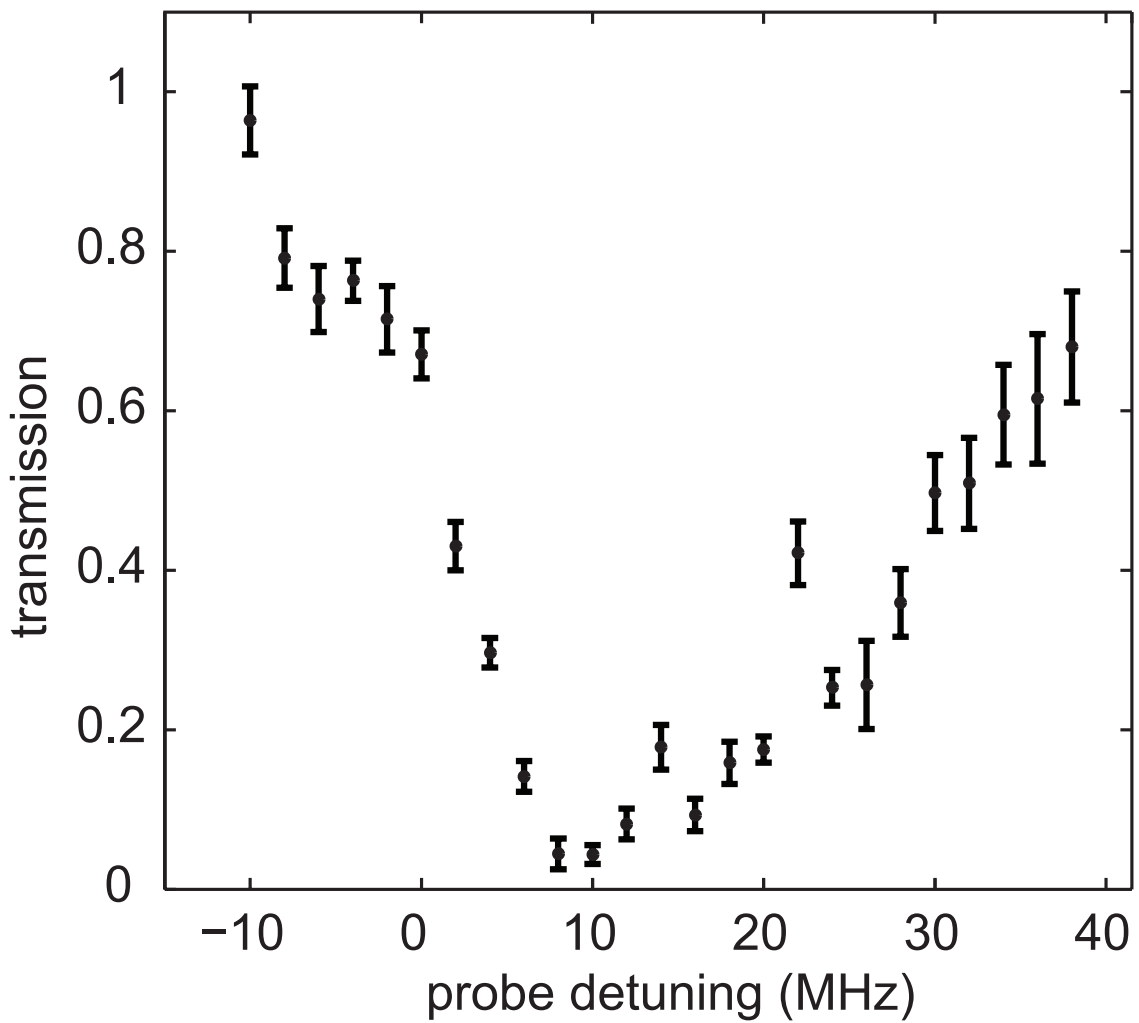


Figure 3.4: Atomic transmission spectra as a function of probe detuning. The detuning is defined relative to the bare atomic resonance, so the overall shift of the transmission dip is due to Stark shifts from the trapping beams. Each dot is average from 50 experimental runs, and the error bars represent  $1\sigma$  statistical errors in the photon counting statistics.

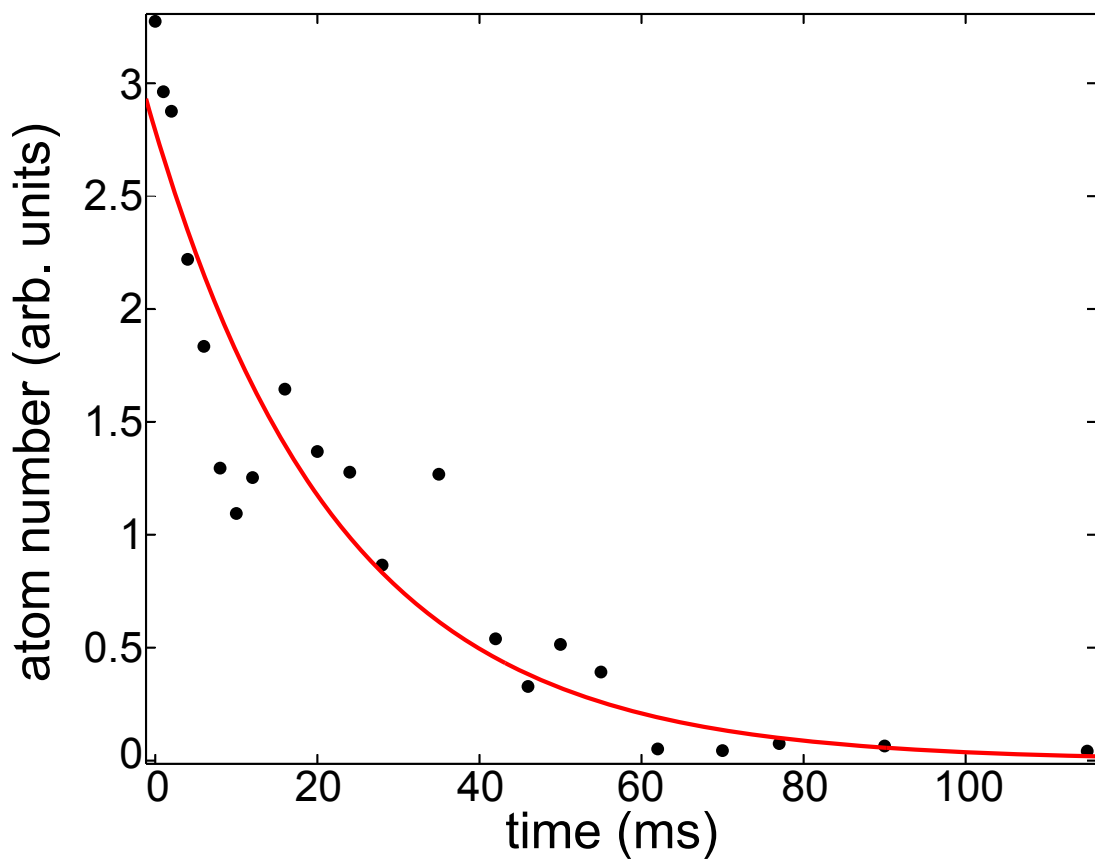


Figure 3.5: Measurement of the trap lifetime based on resonant absorption probing. The extracted  $1/e$  lifetime is 23 ms.

detuned trapping beams, one with parallel polarizations and one with cross polarizations. The parallel case requires lower intensities of blue-detuned light, but it generates larger vector light shifts and produces shallower traps. The cross-polarized configuration results in a deeper trap than the parallel case, and the potential landscapes differ. The parallel trap creates a ring-shaped potential around the nanofiber, but the **orthogonal** case has deep, localized trap sites on either side of the nanofiber. This chapter presents results with a trapping geometry with an angle ( $23.5^\circ$ ) between the polarizations of red- and blue-detuned beams because we measure a higher optical depth at the lowest point with this configuration.  do not have a reason that this particular polarization angle should produce optimal trapping.

### 3.4 Fitting asymmetric absorption curves

To calculate the inhomogeneous broadening of the absorption line, we need to include the differential light shifts for atoms trapped in the optical fiber potential. This requires appropriate weighting over the polarization of the modes, the m-state distribution of the atoms, and the location of the atoms within the trap due to thermal motion. A larger fraction of circular polarization shifts the profile to the blue due and broadens the blue-side of the profile due to the contributions of the vector light shifts.

A complete description of the atomic absorption has contributions from homogeneous (natural linewidth) broadening  $\mathcal{L}_0(\omega - \omega')$  and inhomogeneous broadening

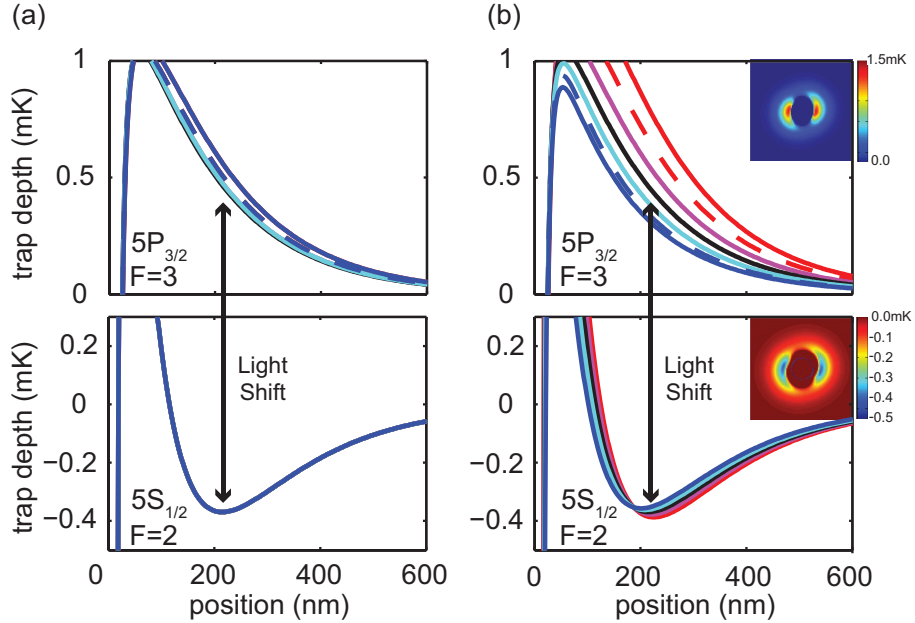


Figure 3.6: Calculated light shifts for Zeeman sublevels with 1064-nm ( $3.35\text{ mW} \times 2$ , standing wave) and 750-nm ( $7.4\text{ mW}$ ) trapping beams. (a) Potentials with linearly polarized trapping beams (top)  $5P_{3/2}$ ,  $F=3$  (radial-axis), where the lines with the color of red, red-dashed, purple, black, cyan, blue-dashed, and blue correspond to  $m_f = +3, +2, +1, 0, -1, -2, -3$ , respectively. (bottom)  $5S_{1/2}$ ,  $F=2$  states (radial-axis); Zeeman sub-levels are degenerate because there are no vector or tensor light shifts. (b) Potential shifts with circularly polarized trapping beams (top)  $5P_{3/2}$ ,  $F=3$  states (radial-axis) where the lines with the color of red, red-dashed, purple, black, cyan, blue-dashed, and blue correspond to  $m_f = +3, +2, +1, 0, -1, -2, -3$ , respectively. (bottom)  $5S_{1/2}$ ,  $F=2$  states (radial-axis), where the lines with the color of red, purple, black, cyan, and blue correspond to  $m_f = +2, +1, 0, -1, -2$ , respectively.

$n(\omega')$ , generally resulting in the symmetric Voigt profile [104] as follows:

$$I(\omega) = I_0 \int n(\omega') \mathcal{L}_0(\omega - \omega') d\omega', \quad (3.3)$$

where  $I(\omega)$  is the convolution of Lorentzian and Gaussian profiles. For the optical transition of  $^{87}\text{Rb}$  atoms, we study inhomogeneous broadening resulting from the atomic temperature distribution, Zeeman-sublevel-dependent population distribution, and all the light shifts from  $5S_{1/2}$  and  $5P_{3/2}$  to other upper transitions. This requires considering scalar, vector, and tensor light shifts, which can be large due to a non-negligible axial-direction electric field component in the fundamental mode  $\text{HE}_{11}$ . For a ground state  $|n, F, m_f\rangle$  and an excited state  $|n', F', m'_f\rangle$  represented by  $i$  and  $j$ , the inhomogeneous term  $n_{ij}(\omega)$  can be defined for trapped atoms having a temperature  $T$  as follows:

$$n_{ij}(\omega) = \int_{V_{eff}} \frac{1}{Z} \exp\left(-\frac{U_{ij}(\vec{r})}{k_B T}\right) \delta(\omega - \omega_{ij}(\vec{r})) dV, \quad (3.4)$$

where  $Z = \int_{V_{eff}} \exp(-U_{ij}(\vec{r})/(k_B T)) dV$ ;  $U_{ij}(\vec{r})$  is the trapping potential of hyperfine ground states ( $5S_{1/2}$ ); and  $\omega_{ij}(\vec{r})$  is the light-shifted optical transition frequency of  $5S_{1/2}$  to  $5P_{3/2}$  ( $n$  to  $n'$ ).  $U_{ij}(\vec{r})$  and  $\omega_{ij}(\vec{r})$ , dependent on powers and polarizations of the two trapping beams, have spatial dependence and need to be integrated over the effective volume of a trap site. The atoms with a temperature  $T$  higher than a local trap potential  $|U_{ij}(\vec{r})|/k_B$  are truncated in the calculation.

Here, we define a homogeneous profile including light shift broadening as follows:

$$\mathcal{L}(\omega - \omega') = \frac{1}{1 + (\omega - \omega')^2 / (\Gamma/2 + \Delta\Gamma(\omega')/2)^2}, \quad (3.5)$$

where  $\Delta\Gamma(\omega')/2 = \Delta\omega'$  is the broadened width of an optical transition  $\omega'$ ; the standard deviations of state-dependent light-shifted optical transitions at each location  $\vec{r}$  are calculated for a frequency  $\omega'$  and averaged over all  $V_{eff}$ .

We define transmission  $T(\omega)$  (Sec. 3.3) based on our definition of the inhomogeneous broadening of the optical transition as follows:

$$T(\omega) = \exp[-OD \sum_{i,j} |\tilde{d}_{ij,q}|^2 f_i \int n_{ij}(\omega') \mathcal{L}(\omega - \omega') d\omega'], \quad (3.6)$$

$$\approx \exp[-N \cdot OD_1 \int n_{ij}(\omega') \mathcal{L}(\omega - \omega') d\omega'], \quad (3.7)$$

where  $n_{ij}(\omega')$  and  $\mathcal{L}(\omega - \omega')$  are defined in Eqs. 3.4 and 3.5,  $f_i$  is determined by optical Bloch equations during optical pumping from the probe beam,  $|\tilde{d}_{ij,q}|^2$  is the relative strength of the atomic dipole moment related to the polarization state of the probe and the population of Zeeman sub-levels, and the optical depth per atom is  $OD_1 = \sigma_0/A_{eff}$  ( $A_{eff}$ : effective mode area,  $\sigma_0$ : scattering cross-section). This can be regarded as a constant for a given  $i, j, q$ , and assumes no light shifts from the low intensity probe.

Given the uncertainties in the exact polarization profile of the optical modes where the atoms are trapped, the m-state distribution of the atoms, and the degree to which a truncated Boltzmann distribution is a correct assumption, we qualitatively use the asymmetric profiles to estimate trapped atom number (see Fig. 3.7). We calculate an atom number of  $N \simeq 300$  for  $T = 55 \mu\text{K}$  using the left and right tails of the absorption profile; this corresponds to  $OD = 8.4$  with our calculated  $OD_1 = 0.028$ .

More recently  have achieved good traps with the beams in the proper orthogonal configuration. Fig. 3.8 displays the transmission curve of that data, and the dashed line is a fit to the symmetric Lorentzian in Eq. 3.2. The goodness of the fit –  $(\chi^2)_{\text{red}} = 1.04$

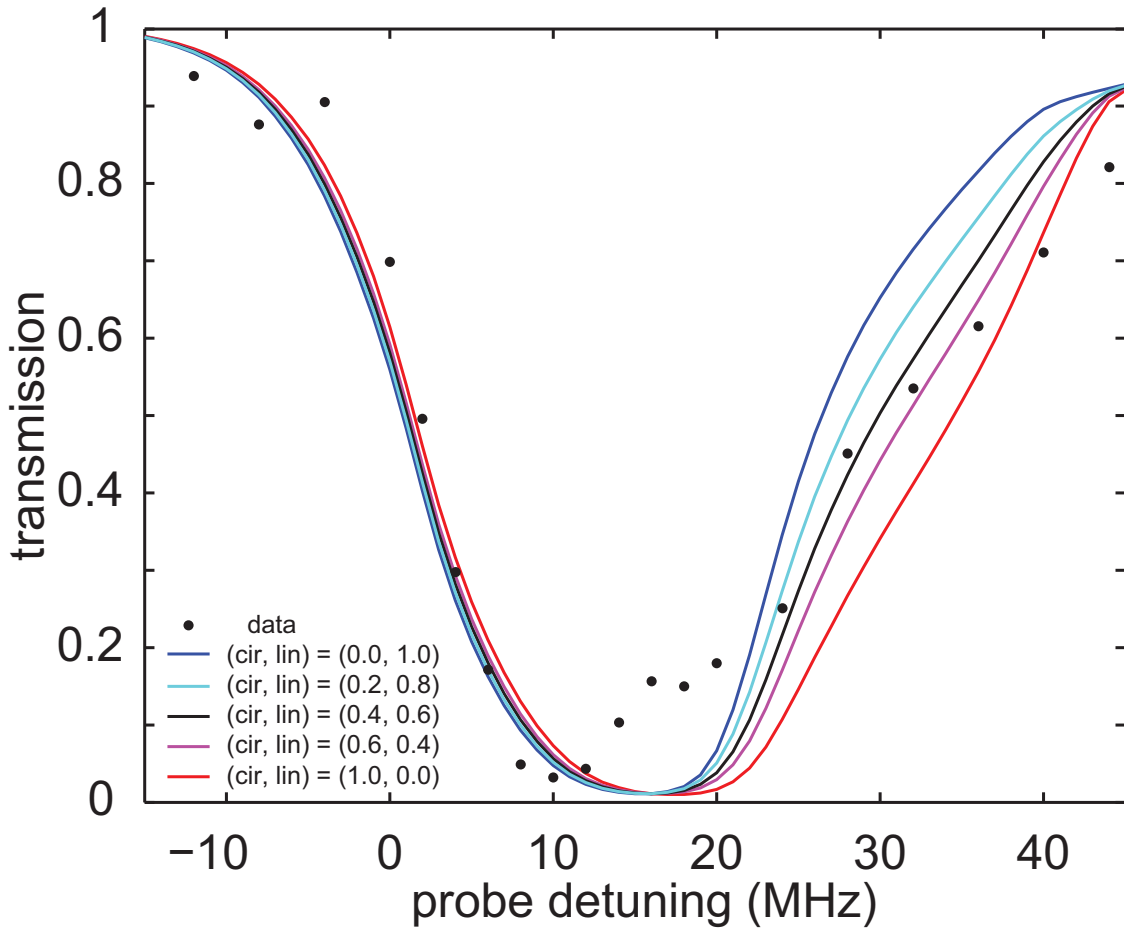


Figure 3.7: Simulated spectra (red-, magenta-, black-, cyan-, blue-line) for the asymmetric absorption measurement data (black dots) are represented with the ratio,  $(\text{cir}, \text{lin})$ , of circularly polarized light and linearly polarized light. We use 3.35 mW of power in each leg of the red-detuned standing wave and a single 7.4-mW blue-detuned beam.

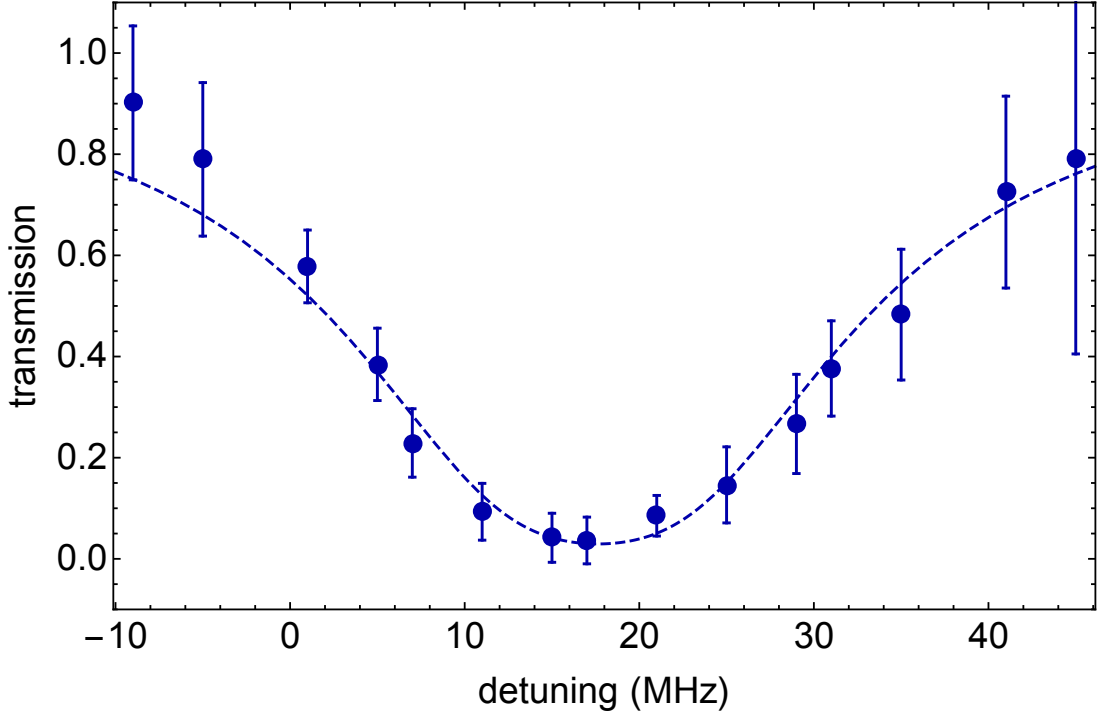


Figure 3.8: Transmission spectrum for atoms trapped in orthogonally-polarized configuration. Better polarization alignment yields a more symmetric line-shape. The dashed line is a fit to the symmetric Lorenztian in Eq. 3.2, with  $(\chi^2)_{\text{red}} = 1.04$ . The extracted *OD* of 3.52 gives an approximate atom number of 125.

— suggests that the asymmetry caused by vector light shifts has been largely eliminated.

The optical depth of 3.52 corresponds to about 125 atoms for this dataset.

### 3.5 Conclusions

This chapter presented data that confirms optical trapping of  $^{87}\text{Rb}$  atoms around an optical nanofiber. We can confine  $\sim 300$  atoms in the evanescent mode of the ONF with typical trap lifetimes around 23 ms. Future work will include adding additional cooling protocols (e.g. polarization-gradient cooling or Raman sideband cooling) to prolong the trap lifetime. We also want to sensitively probe fictitious and real, external magnetic fields

using Faraday spectroscopy with trapped atoms, which we discuss further in Sec. 7.1. A longer-term effort will be to remove the axial confinement from the red-detuned standing wave and drive the atoms with an external laser beam. The long-range atom-atom interactions mediated by the guided mode will lead to interesting collective effects such as self-organization [100, 101]. We elaborate on this in Sec. 7.4.

## Chapter 4: Photon correlation measurements

### 4.1 Introduction

The intensity autocorrelation function,  $g^{(2)}(\tau)$ , measures fluctuations ~~on~~ the light intensity, ~~e.g.~~ the photon statistics [105], and can reveal both classical and quantum aspects of the light and its sources. We ~~propose and~~ demonstrate a temperature measurement method using the correlations of atomic fluorescence emitted into the guided mode of the nanofiber. When the emitters are not stationary, the intensity autocorrelation function is sensitive to their dynamics as well as the geometry of the mode into which they emit [106, 107]. Systems such as atomic beams [108, 109], single atoms in a MOT [110, 111], and a single trapped ion [112] were used to measure these transit-time effects. While bunched and antibunched photon statistics have been observed in the light emitted into the ONF guided mode [113–116], the correlations related to classical atomic dynamics near the ONF have not been studied. Here we measure the transit-time envelope of the correlations for different atomic temperatures and various potentials. The dependence of this timescale on temperature allows for a simple model to extract the MOT temperature directly from the correlations.

This chapter is organized as follows. Sec. 4.2 provides a general overview of intensity autocorrelations; Sec. 4.3 outlines the nanofiber mode structure, optical dipole potential, light shifts, and coupling strength of the system; Sec. 4.4 briefly discusses the theoretical

considerations for calculating and simulating correlations; and in Sec. 4.5 we present the experimental results and comparisons to simulations.

## 4.2 Intensity autocorrelations

The intensity autocorrelation function,

$$g^{(2)}(\tau) = \frac{\langle I(t) I(t + \tau) \rangle}{\langle I(t) \rangle^2}, \quad (4.1)$$

measures the conditional probability of measuring a photon at a time delay of  $\tau$  from recording the first photon at time  $t$ . Here  $\langle \cdot \rangle$  denotes time average. At its core, the intensity autocorrelation function looks at the fluctuations in the intensity,  $I(t)$ . To see this, we write the classical intensity  $I(t)$  in terms of its average value and fluctuations about the mean,  $I(t) = \bar{I} + \delta I(t)$ . Consider  $g^{(2)}(0)$ , the autocorrelation at zero time delay:

$$g^{(2)}(0) = \frac{\langle I^2(t) \rangle}{\langle I(t) \rangle^2} \quad (4.2)$$

$$= \frac{\langle \bar{I}^2 + 2\bar{I}\delta I(t) + \delta I^2(t) \rangle}{\bar{I}^2} \quad (4.3)$$

$$= 1 + \frac{\langle \delta I^2(t) \rangle}{\bar{I}^2}, \quad (4.4)$$

where we have used the definition  $\langle \bar{I} \rangle = \bar{I}$  and the fact that the expectation value of the fluctuations is zero ( $\langle \delta I(t) \rangle = 0$ ). We see that the autocorrelation function measures the variance of the noise in the system.

This function contains contributions from different sources including single-atom field-field correlations, single-atom intensity-intensity correlations, different-atom field-field correlations, etc. Neglecting correlations between the fields of different atoms, we

can write  $g^{(2)}$  as [106]

$$g^{(2)}(\tau) = 1 + \left|g_A^{(1)}(\tau)\right|^2 + \frac{1}{\bar{N}}g_A^{(2)}(\tau), \quad (4.5)$$

where  $\bar{N}$  is the average atom number in a given time, and  $g_A^{(2)}(\tau)$  and  $g_A^{(1)}(\tau)$  are the single-atom intensity-intensity and field-field correlations, respectively. Thus for small atom number, we can observe the antibunching term  $g_A^{(2)}(\tau)$  (note for large  $\bar{N}$  that the correlation function reduces to the power spectral density of the light,  $|g_A^{(1)}(\tau)|^2$ ).

It is worth making a note regarding the term “anitbunching” and what we mean by it. Sub-Poissonian statistics ( $g^{(2)}(0) < 1$ ) and antibunching ( $g^{(2)}(0) < g^{(2)}(\tau)$ ) readily go hand in hand, so there is often a conflation between the terms in the literature [117]. In the absence of atom-number fluctuations, antibunched photon statistics will in general also be sub-Poissonian [118]. With atom-number fluctuations, however,  $g^{(2)}(0)$  can be greater than one, but one can still observe increasing coincidence dates with increasing delay time, and this constitutes a violation of a Cauchy-Schwarz inequality for classical fields [118]. This is precisely the situation encountered in this chapter, where a thermal source of atoms around the fiber generates antibunching on top of super-Poissonian statistics.

### 4.3 The system

The experiment relies on two main parts: a source of cold atoms and an ONF. A MOT provides a constant source of slowly moving atoms whose fluorescent light can couple into the guided mode of the optical nanofiber. The nanofiber serves two purposes, as it collects the light from the atoms and also modifies the local potential landscape through which the atoms move, with typical velocities of  $10 \text{ cm} \cdot \text{s}^{-1}$ . Sending far-off-resonant, red-

detuned light with a wavelength of 1064 nm through the nanofiber adds a further confining potential that we can controllably vary to systematically study atomic dynamics near the fiber surface.

### 4.3.1 Nanofiber mode structure

We consider only single-mode nanofibers, i.e. they are pulled to a small enough diameter such that all higher-order modes are cut off. The mode (HE<sub>11</sub>) of such an optical nanofiber has an intensity profile given by [19]

$$|\mathbf{E}(\mathbf{r})|^2 = \mathcal{E}(\mathbf{r})^2 [K_0^2(qr) + uK_1^2(qr) + wK_2^2(qr)] , \quad (4.6)$$

where  $\mathcal{E}$  is the complex field amplitude;  $K_i$  is the modified Bessel function of the second kind of order  $i$ ;  $u$  and  $w$  are constants obtained from Maxwell's equations; and  $q = \sqrt{\beta^2 - k^2}$  describes the radial field decay, with  $\beta$  being the field propagation constant in the nanofiber and  $k = 2\pi/\lambda$  the free-space wavevector.



### 4.3.2 Potentials

For a two-level atom, which we assume throughout this work, the optical dipole potential produced by a far-off-resonant evanescent field is given by [119]

$$U_{dip}(\mathbf{r}) = \frac{3\pi c^2 \Gamma}{2\omega_0^3} |\mathbf{E}(\mathbf{r})|^2 \times \sum_i \frac{c_i^2}{\Delta_i} , \quad (4.7)$$

where  $\omega_0/2\pi$  is the atomic transition frequency (384.23 THz for the  $D_2$  line of <sup>87</sup>Rb),  $\Gamma/2\pi$  is the natural linewidth of the  $5P_{3/2}$  state (6.06 MHz),  $\Delta_i = \omega_i - \omega_0$  is the trap

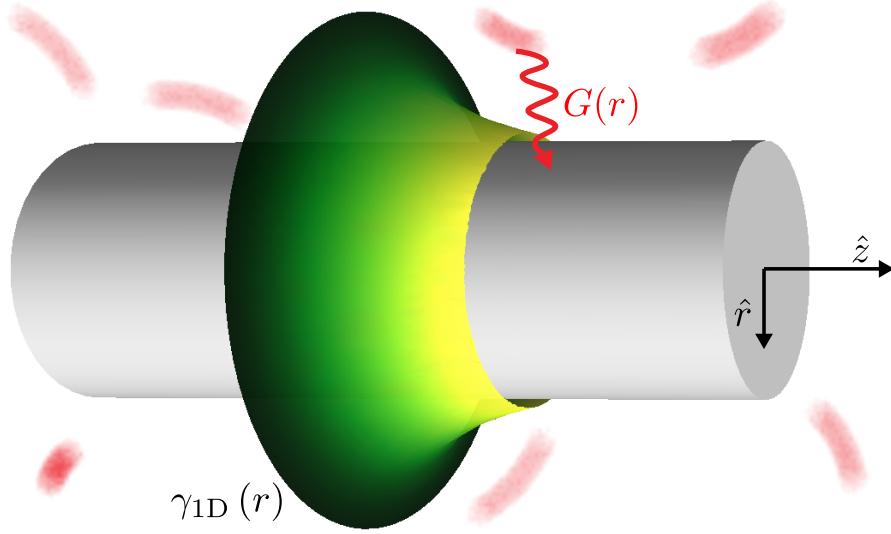


Figure 4.1: Schematic diagram of moving atoms (red streaks) near a nanofiber waist, denoting the position-dependent coupling,  $G(r)$ . This coupling is proportional to the scattering rate into the guided mode,  $\gamma_{1D}(r)$ , which is represented by the color plot.

laser detuning from excited state  $|e_i\rangle$ ,  $c_i$  is the line strength between the ground state and excited state  $|e_i\rangle$ , and  $|\mathbf{E}(\mathbf{r})|^2$  is given by Eq. 4.6. We treat our ground state as uniformly populated in the  $F = 2$  manifold and consider coupling to both the  $5P_{1/2}$  and  $5P_{3/2}$  states when calculating Eq. 4.7. We approximate the nanofiber as an infinite dielectric plane and use the Lennard-Jones form when calculating the van der Waals potential [120–122], so that  $U_{\text{vdW}}(d) = C_3 \times d^{-3}$  with the  $C_3$  coefficient equal to  $4.94 \times 10^{-49} \text{ J} \cdot \text{m}^{-3}$  for the  $5S_{1/2}$  level of  $^{87}\text{Rb}$ . The infinite-plane approximation is accurate to within 20% for atom-fiber distances less than 200 nm [19].

### 4.3.3 Light shifts

The combined dipole and van der Waals potentials shift the atomic levels, and they each depend on position. The shifts produce a spatially-varying absorption probability:

$$p_{\text{abs}}(\mathbf{r}, P) = \frac{s}{1 + s + 4 \left( \frac{d\omega(\mathbf{r}, P) + \delta}{\Gamma} \right)^2}, \quad (4.8)$$

where  $s = I/I_{\text{sat}}$  is the saturation parameter ( $I_{\text{sat}} = 3.58 \text{ mW} \cdot \text{cm}^{-2}$  for a uniform sublevel population distribution [123]),  $\delta = \omega_L - \omega_0$  is the detuning of the driving beam from atomic resonance, and  $d\omega(\mathbf{r}, P)$  is the scalar light shift from a beam with power  $P$  (with a wavelength of 1064 nm in our experiment) and van der Waals assuming a two-level atom. Note that for the quantitative atomic cloud temperature measurement, no 1064-nm power is used so that the shift in Eq. 4.8 arises entirely from the van der Waals interaction. Our simulations of this temperature measurement reflect this fact. Later we demonstrate experimentally that this timescale decreases as 1064-nm light is sent through the nanofiber. Though no quantitative comparisons between simulation and experiment are made in this case, we do use the simplified level shift treatment of this section to observe the same qualitative behavior.

### 4.3.4 Coupling strength

The coupling strength of an atom to the ONF is the fraction of spontaneous emission that couples into the fiber versus into free space [124, 125],

$$G(\mathbf{r}) = \gamma_{1D}(\mathbf{r}) / \gamma_0. \quad (4.9)$$

Fermi's golden rule determines the form of  $\gamma_{1D}$ , which follows the spatial variation of Eq. 4.6 since the scattering rate is intensity-dependent.

Photon detection in the experiment is a joint process of absorbing a photon from the MOT beams and emitting into the nanofiber mode, and we multiply the coupling strength by the photon absorption probability in Eq. 4.8.

## 4.4 Theoretical background

The correlation function from resonance fluorescence emitted into the fundamental mode exhibits transit-time effects related to the geometry of that mode, as atoms act as beacons signaling their position while passing through it. We write down the full guided-mode structure and then make a series of approximations to fit experimental data, which is an average over many atomic trajectories. We then discuss an efficient classical method of simulating correlation functions by modeling random trajectories, taking into account the full potential landscape Eq. 4.7, the position-dependent coupling strength Eq. 4.9, and the position-dependent light shifts Eq. 4.8 due to dipole and surface potentials.

### 4.4.1 Transit-time effects

Laser-cooled atoms are not stationary emitters. Accounting for the motion of atoms amounts to adding a temporal envelope,  $f(\tau)$  to Eq. 4.5:  $g^{(2)}(\tau) = 1 + |f(\tau)g_A^{(1)}(\tau)|^2 + f(\tau)g_A^{(2)}(\tau)/\bar{N}$  [108]. This function generally depends on the environment and how the emitted light couples to the detection apparatus - it is the shape of this temporal envelope that will allow us to extract information regarding the dynamics of atoms moving near an ONF.

#### 4.4.2 Relating correlations to temperature

We can relate the width of the correlation function to the temperature of the atomic cloud because the velocity of the atoms determines the timescale of the interaction with the nanofiber. The ONF mode described by Eq. 4.6 possesses a characteristic length scale of  $1/q$ . Dividing this length by the most probable velocity of a Maxwell-Boltzmann distribution of atoms at a temperature  $T$ ,  $v_p = \sqrt{2k_B T/m}$ , yields a simple relationship between transit time and temperature:

$$\tau_0 = \frac{a}{q} \sqrt{\frac{m}{2k_B T}}, \quad (4.10)$$

where  $a$  is an overall scale factor based on the geometry of the problem. We are unable to find an analytical form for  $a$  from physical considerations, but discuss its variation with simulations in Sec. 4.5.5.

#### 4.4.3 Simulating atomic trajectories

Due to the timescales and parameter regime considered in this paper, we can safely neglect a few effects that are present. We approximate the ONF as an infinite plane when calculating the surface potentials, which is valid since the curvature of the ONF becomes important only far away from the surface where the coupling strength is small. We also ignore momentum diffusion as the recoil velocity ( $\sim \text{mm} \cdot \text{s}^{-1}$ ) is small compared to typical atomic velocities ( $\sim \text{cm} \cdot \text{s}^{-1}$ ), and scattering events are not frequent enough on microsecond timescales to appreciably affect the speed of the atom. We neglect velocity-dependent forces, as the Doppler shifts ( $\sim 100 \text{ kHz}$ ) are small compared to the light shifts

produced by the various potentials ( $\sim$  tens to hundreds of MHz).

Trajectories are inserted into the position-dependent coupling strength in Eq. 4.9 and the position-dependent absorption probability in Eq. 4.8, which are then multiplied together. This yields a time-dependent detection probability for each trajectory. Time-correlating a detection probability trajectory with itself produces a signal proportional to the intensity autocorrelation for a single atom.

## 4.5 Experiment and results

### 4.5.1 Apparatus

We load the MOT from the low-velocity tail of a background vapor of  $^{87}\text{Rb}$  atoms produced by a dispenser (see details in [77]). We change the intensity and detuning of the cooling beams in order to controllably vary the temperature of the atomic cloud between  $\sim 200 - 800 \mu\text{K}$ , as measured by time-of-flight expansion through fluorescence imaging. The high atomic cloud temperatures explored in this work are limited by the particular time-of-flight (TOF) imaging system in our setup, where atom numbers for colder MOTs were too low to accurately fit the cloud width. We see no fundamental limitation to the correlation measurement technique, but present only temperatures with which we could provide calibration to a known technique.

The optical nanofiber (ONF) is produced via the flame brushing technique, as explained in Chap. 2. [74, 81]. We do not have an accurate measure of the transmission of the fiber used for this experiment, but it supported 40 mW of 760-nm light in UHV without breaking. We glue (EPO-TEK OG116- 31) the fiber to a titanium u-shaped mount for stability, and attach the mount to a UHV-compatible manipulator system (VG Scienta

Transax). The manipulator consists of a motorized stepper motor along one axis and 2D manual translations stages along the other axes. This manipulator works in conjunction with three pairs of magnetic shim coils to optimally overlap the nanofiber waist with the region of highest atomic density in the cloud.

The ONF in our setup has a diameter of  $500 \pm 50$  nm, uniform over a length of 7 mm, where the uncertainty in diameter likely arises from air currents changing the location of the fiber in the flame near the end of the pull [74]. This fiber geometry with the stated uncertainty accepts only one guided mode, described by Eq. 4.6 above, at both experimentally relevant wavelengths of 780 nm and 1064 nm. Light that couples into this mode is filtered by a volume Bragg grating (VBG, OptiGrate BP-785), a narrow-line interference filter (Semrock LL01-780-12.5), and a long-pass color filter (Thorlabs FGL645) before being sent to the two fiber-coupled SPCMs, as shown in Fig. 4.2. A FPGA stores and time-tags output TTL pulses from the SPCMs, which are then post-processed in software and correlated. An internal clock of 48 MHz sets the minimal time resolution to 20.83 ns. The use of two SPCMs circumvents problems near zero time delay related to detector dead time, typically 50 ns.

Aside from varying the atom temperature, changing the local potential near the nanofiber surface acts as the main experimental knob. An additional attractive potential formed with a red-detuned, 1064-nm beam accelerates atoms as they approach the fiber surface, modifying their interaction time with the nanofiber guided mode and decreasing the local atom density near the fused silica surface [126]. We couple a 1064-nm beam from the Nd:YAG laser in one direction along the nanofiber, providing confinement only in the radial and azimuthal directions. The polarization of the beam is circular in order to create an azimuthally-symmetric potential, and the polarization on the waist is verified

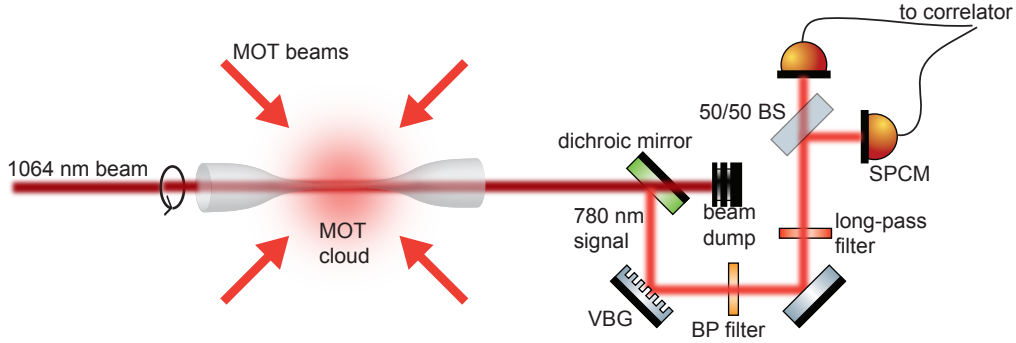


Figure 4.2: Experimental schematic. A MOT is spatially-overlapped with a nanofiber, and the MOT beams drive resonance fluorescence that couples into the guided mode. This signal is filtered by a volume Bragg grating (VBG), bandpass (BP) filter, and long-pass filter before being split by a 50/50 beamsplitter (BS) and sent to two SPCMs. TTL pulses from the SPCMs are time-tagged by an FPGA and correlated in software.

by performing a polarization-sensitive measurement of the Rayleigh scattering of 1064-nm light on the waist [22, 102]. We vary the power of this beam between 0 – 8 mW, as measured at the output of the nanofiber. The resulting dipole potential has a shape that closely resembles a decaying exponential but strictly speaking is a sum of modified Bessel functions of order 0, 1, and 2 (see Eq. 4.6) [19]. At powers larger than 8 mW, the density near the fiber decreases such that the thermal bunching peak at zero time delay is unresolvable within our signal-to-noise ratio.

### 4.5.2 Data and fitting

The MOT beams drive spontaneous emission in the atoms and are on continuously during data acquisition. We collect  $\sim 2.5 \cdot 10^7$  photon counts for each experimental run, corresponding to about 45 min of averaging per data point. Time-of-flight imaging measures the temperature of the atomic cloud before and after a full scan of 1064-nm laser powers. The correlation measurements can be extended to colder clouds by averaging for

longer times, but we had trouble confirming colder temperatures via TOF due to low atom number in our MOT.

We calculate a correlation function from the list of times corresponding to photon detection events. We do not do any further binning of the data, so that the timing resolution is 20.83 ns set by the internal clock of the FPGA. While this obscures details on atomic spontaneous emission timescales (tens of nanoseconds), it provides good resolution on the few microseconds where the classical dynamics imprint their signature on the correlation function. Measurements using an oscilloscope (Tektronix DPO 7054) with finer time resolution allowed us to observe antibunching for low atom number. The Rb dispenser current controls the number of atoms in the MOT, so that we can change the average number of atoms interacting with the nanofiber mode. Fig. 4.3 shows the transition from antibunched (increasing slope after  $\tau = 0$ , estimated atom number is  $\sim 1.4$ ) to bunched (decreasing slope after  $\tau = 0$ , estimated atom number is  $\sim 6$ ) correlations as we increase the number of atoms fluorescing into the mode of the ONF. We can control the MOT to have, on average, only a small number ( $\sim 1$ ) of atoms interacting with the nanofiber mode on these timescales, confirming a similar result observed in [115].

Fig. 4.4 displays an example of  $g^{(2)}(\tau)$  extracted from data for an atom temperature of 463  $\mu\text{K}$  and 1064-nm power of 0 mW (note the very different timescale than in Fig. 4.3). The broad bunching feature centered around zero time delay suggests a thermal signal on top of coherent background from MOT light that couples into the nanofiber guided mode. This signal has a characteristic width based on transit-time effects, which is the result of a position-dependent atom-fiber coupling strength combined with moving atoms. An atom at a particular point of the mode will sample it with probability proportional to its intensity at that position, and averaging over many atomic trajectories will sample the

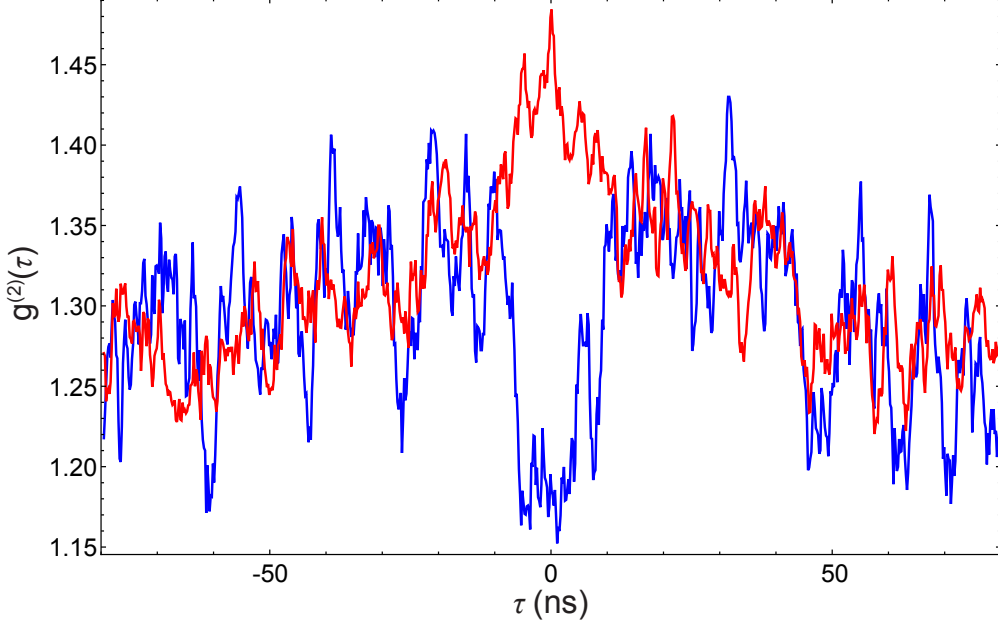


Figure 4.3: Unnormalized second-order correlation function,  $G^{(2)}(\tau)$ , as a function of delay time. The curves show data for low (blue) and high (red) Rb dispenser currents.

entire mode. In this way, the autocorrelation function contains information about the mode in question (the shape of  $g^{(2)}(\tau)$ ) and about the dynamics of the atoms (the decay time of  $g^{(2)}(\tau)$ ).

We make a series of approximations to fit this mode structure to the observed transit-time broadening in our data. The factors  $u$  and  $w$  in Eq. 4.6 are small for a fiber radius of 250 nm and wavelength of 780.24 nm (0.166 and 0.00875, respectively), so we neglect them and keep only the first term proportional to  $K_0^2$ . As a further approximation we also take the asymptotic form of  $K_\alpha$  [127],

$$K_\alpha(z) \sim \sqrt{\frac{\pi}{2z}} e^{-z} \left( 1 + \frac{4\alpha^2}{8z} + \dots \right), \quad (4.11)$$

where  $\alpha$  is the order of the Bessel function, and  $z$  is a complex argument satisfying  $|\arg z| < 3\pi/2$ . This yields a field intensity around the nanofiber proportional to  $\exp[-2qr]/2qr$ .

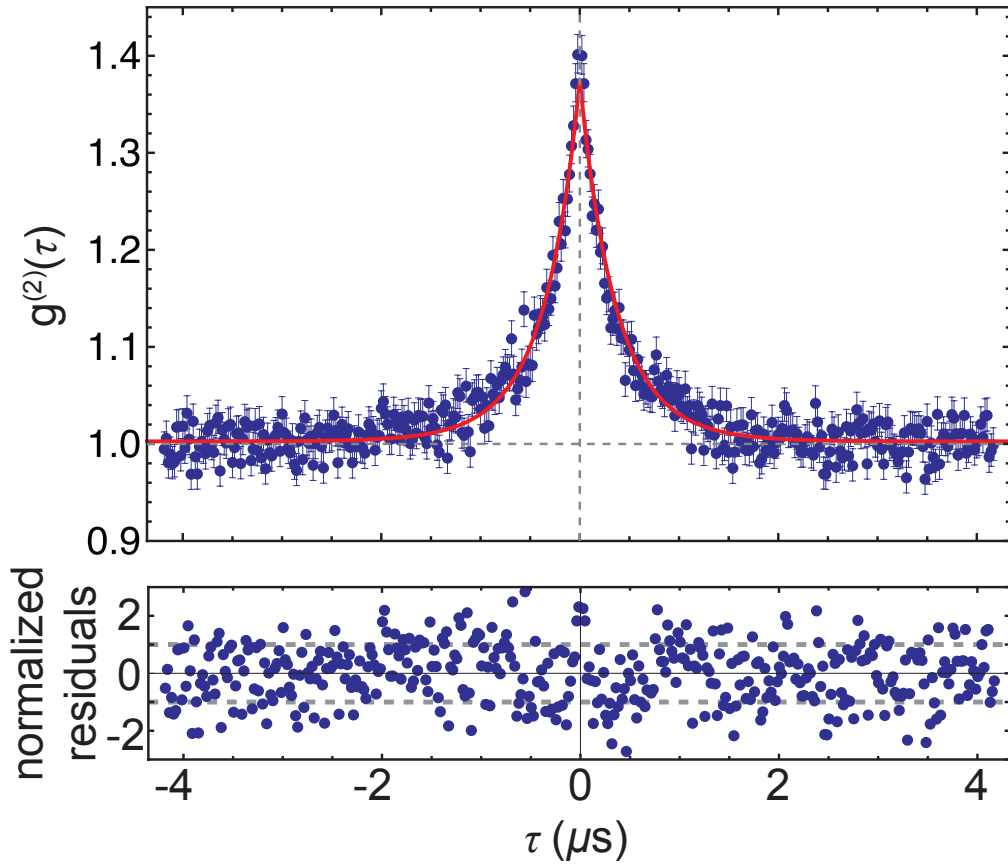


Figure 4.4: Second-order correlation function,  $g^{(2)}(\tau)$ , as a function of delay time for an atom temperature of  $463 \mu\text{K}$  and for  $0 \text{ mW}$  of  $1064\text{-nm}$  light. The data (blue dots) are fit (solid red line) to Eq. 4.12, with the normalized residuals displayed in the lower plot.

Defining an effective index of refraction,  $n_{\text{eff}} = \beta/k$ , we can rewrite the propagation constant so that the decay parameter becomes  $q = k\sqrt{n_{\text{eff}}^2 - 1}$ , which evaluates to  $0.62k$  for our nanofiber. We then recast the spatial dependence of the intensity into a temporal function in order to fit the measured correlations as  $g^{(2)}(\tau) = 1 + f(\tau)g_A^{(2)}(\tau)$  in Eq. 4.5 [108,109], neglecting the field-field correlations that vanish on the timescales measured in our experiment. This yields

$$f(\tau) = A \frac{e^{-2(|\tau|/\tau_0 + 0.62k r_0)}}{(|\tau|/\tau_0 + 0.62k r_0)}, \quad (4.12)$$

where  $r_0 = 250$  nm is the fiber radius, and the absolute value reflects the time-symmetric nature of the autocorrelation function for stationary processes. Here the fitting parameter  $A$  is an overall amplitude determined by the signal-to-background ratio and the average number of atoms interacting with the nanofiber mode. The parameter  $\tau_0$  represents a characteristic width of the correlation function.

The red line in Fig. 4.4 illustrates the quality of this fitting function for an atomic temperature of approximately  $463 \mu\text{K}$ , with a reduced  $\chi^2$  of 1.02 for this set of data. We note that this functional form leads to statistically better fits than other standard functions (e.g. exponential decay or Gaussian) as measured by the reduced  $\chi^2$ .

### 4.5.3 Temperature extraction

We measure correlations and extract the width  $\tau_0$  for various atomic temperatures in order to verify Eq. 4.10, with each temperature also measured by standard TOF imaging. Fig. 4.5 shows a plot of these data, where the vertical error bars are the standard errors in the fit, and the horizontal error bars originate from uncertainty in the magnification

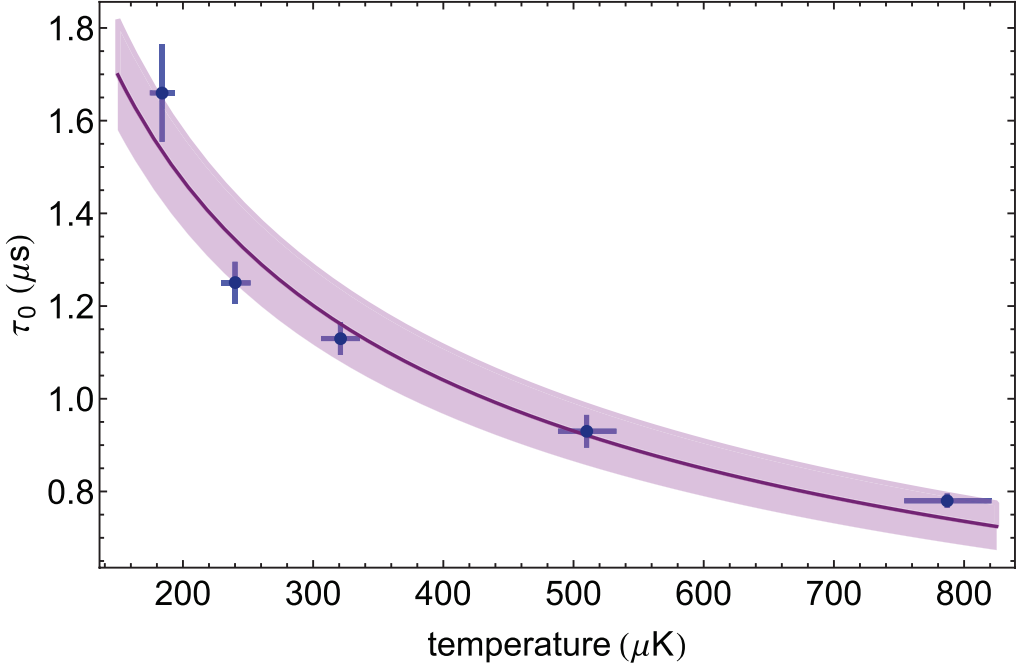


Figure 4.5: Extracted timescale,  $\tau_0$ , vs. temperature (measured via TOF). The vertical error bars indicate standard error in the fit of Eq. 4.12, and the horizontal error bars arise from uncertainty in the magnification of the imaging system. The purple line is a fit to Eq. 4.10, and the shaded regions are 95% confidence bands. The reduced  $\chi^2$  is 1.65.

of the imaging system. We confirm that the horizontal uncertainties are similar (few percent) to the errors obtained directly from the TOF fits. The purple line in Fig. 4.5 is a fit to Eq. 4.10, and the shaded areas represent 95% confidence bands. We observe good agreement between the model and the data, as the fit has a reduced  $\chi^2$  of 1.65, and the overall scale parameter is  $a = 1.44 \pm 0.04$ . The ~~deviation~~ of this scale factor ~~from 1~~ is discussed further in Sec. 4.5.5.

#### 4.5.4 Atomic dynamics

The measurements in Sec. 6.1.2 utilized the ONF as a passive probe, as the fiber modifies the local environment only over short distances where the surface potential is strong. Varying the power of 1064 nm light propagating through the ONF offers us the

ability to change the potential landscape near the nanofiber and consequently change the atomic dynamics. Given the longer-range interaction of this attractive dipole potential, the atomic trajectories are affected over longer timescales, whose change we can observe with the same correlation measurements.

Fig. 4.6 displays the correlation width for the three different temperatures as a function of 1064 nm laser power, where the error bars are the  $1-\sigma$  errors in the fits. We determine these  $\tau_0$  using the fit displayed in Fig. 4.5. There are some interesting features in the data worth noting. The initial decrease in timescale is due to acceleration of the atoms as they experience the increasingly strong confining potential of the 1064 nm beam. Atomic temperature determines the slope of this decrease, as slower atoms are more easily “captured” by the potential, and we see that the magnitude of the slope decreases as the atom temperature increases. We discuss the saturation behavior at higher 1064 nm laser power in more detail in the next section.

#### 4.5.5 Simulations

We simulate data by generating classical atomic trajectories subject to Newton’s equations of motion [128]. These simulations include the potentials and light shifts discussed in Sections 4.3.2 and 4.3.3. The classical nature of the simulations is justified because the smallest angular momenta present in the system are still  $\sim 100$  times larger than the Planck constant.

The atoms start at a radial distance of 1500 nm away from the fiber surface, where the coupling is weak due to the rapid decay of the mode with length scale  $1/q$ . Symmetry of the problem allows us to restrict trajectories to the x-y plane with initial velocities pointing in one quadrant, making sure to sample the speeds from a 3D Maxwell-Boltzmann

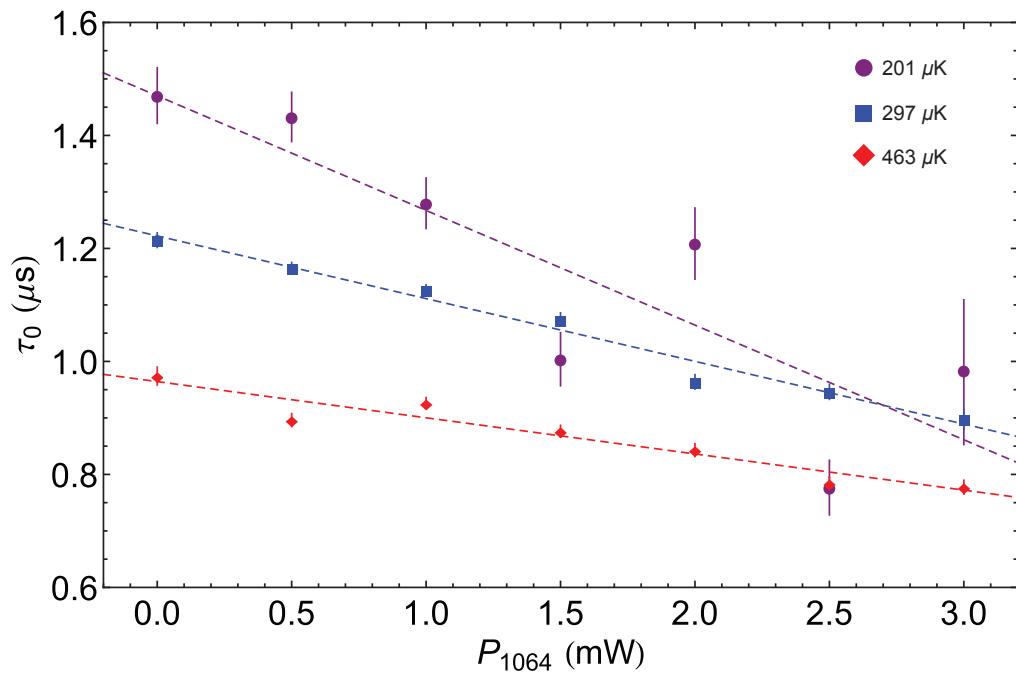


Figure 4.6: Extracted correlation function width,  $\tau_0$ , as a function of  $P_{1064}$  for atom temperatures of 201  $\mu$ K (purple dots), 297  $\mu$ K (blue squares), and 463  $\mu$ K (red diamonds). The error bars indicate standard error in the fit. Dashed lines are linear fits to the displayed points to illustrate the increasing effect of the 1064-nm beam as atom temperature decreases.

distribution before projecting onto this plane. Trajectories evolve for either  $50 \mu\text{s}$  or when the atom strikes the fiber surface, whichever happens first.

The dipole potential used in the simulations is a numerical fit to the full, scalar solution in order to ease integration. Similarly, the coupling strength in Eq. 4.9 is a fit to the complete solution for a two-level atom [125]. We also assume that the orientation of the atomic dipoles relative to the fiber surface is random, so that the coupling strength is an effective ensemble average. Independent measurements confirm that minimal optical pumping occurs in our MOT, and this assumption of random orientations is valid.

Once a trajectory is calculated and fed into the detection probability, we discretize these time-dependent probabilities onto a mesh of  $50 \text{ ns}$  resolution so that calculating the correlation function becomes a simple array operation. Experimentally measured values for atom temperature and  $1064 \text{ nm}$  laser power are fed into the simulation, which is averaged over  $10^4$  randomly sampled speeds and directions. The resulting correlation function is fit to Eq. 4.12 in order to extract the decay time  $\tau_0$ , as shown in Fig. 4.7.

We first utilize the simulations to address the deviation from unity of the scale factor in Eq. 4.10. Fig. 4.8 displays the dependence of the transit time on the angular spread of the atomic trajectories for a distribution with temperature  $90 \mu\text{K}$ . For an atomic beam aimed directly at the fiber, we extract a transit time of  $1.48 \mu\text{s}$ , which matches well the calculated time of  $1.53 \mu\text{s}$  using Eq. 4.10 with  $a = 1$ . The transit time increases slowly as we increase the angular distribution of trajectories, until it hits a critical value of  $\arctan(250/1500) = \arctan(1/6)$ , corresponding to the point after which not all paths will intersect with the nanofiber. Atoms can then interact with the fiber over distances longer than  $1/q$ , and the transit time consequently increases further. There is a saturation at angles approaching  $\pi/2$ , as the rapid decay in the atom-fiber coupling strength ensures

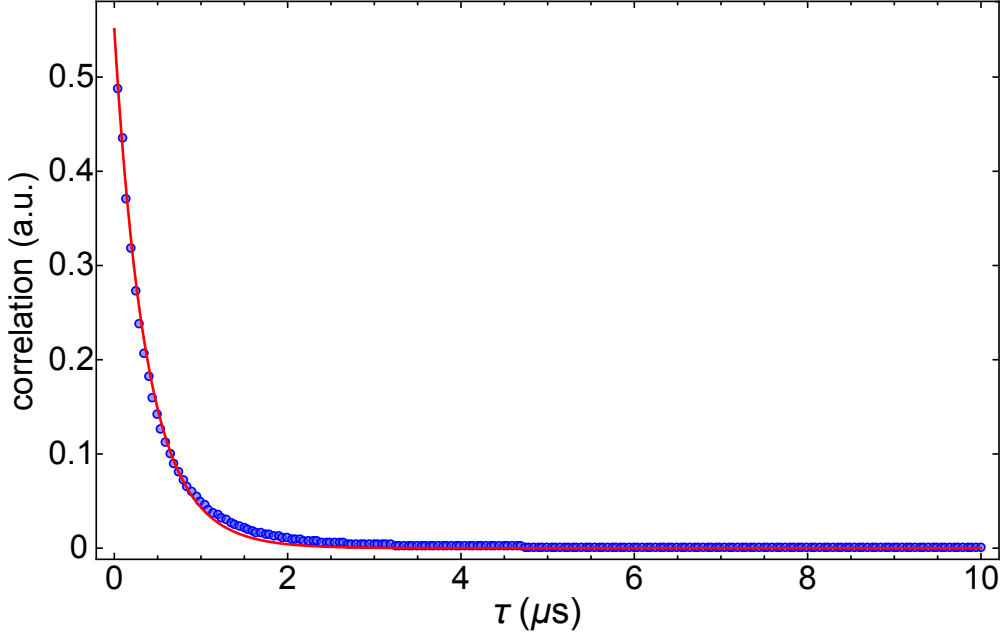


Figure 4.7: Simulated correlation vs. delay time for an atomic temperature of 787  $\mu\text{K}$ . The red line is a fit to the simulated data (blue circles) using Eq. 4.12.

that atoms remaining many decay lengths away from the fiber surface will contribute little to the correlation signal. Fig. 4.8 illustrates that the simulation fully samples the interaction region with an angular spread of at least  $\pi/6$ . Moreover, we note that the ratio of the transit time for the fully-sampled simulation to the effective one-dimensional simulation with no angular spread is 1.7, motivating our measured scale parameter of  $a = 1.44 \pm 0.04$ .

We complete this calculation for the same temperatures measured in the experiment (see Fig. 4.5) and plot the results in Fig. 4.9. The red line displays a fit of the simulated data to Eq. 4.10, yielding a scale parameter of  $a = 1.88$ . We observe qualitative agreement between the simple model and full simulation of the dynamics. We also plot for comparative purposes the fit to experimental data from Fig. 4.5 as a purple line. The discrepancy between data and simulation can be partially explained by a residual mag-

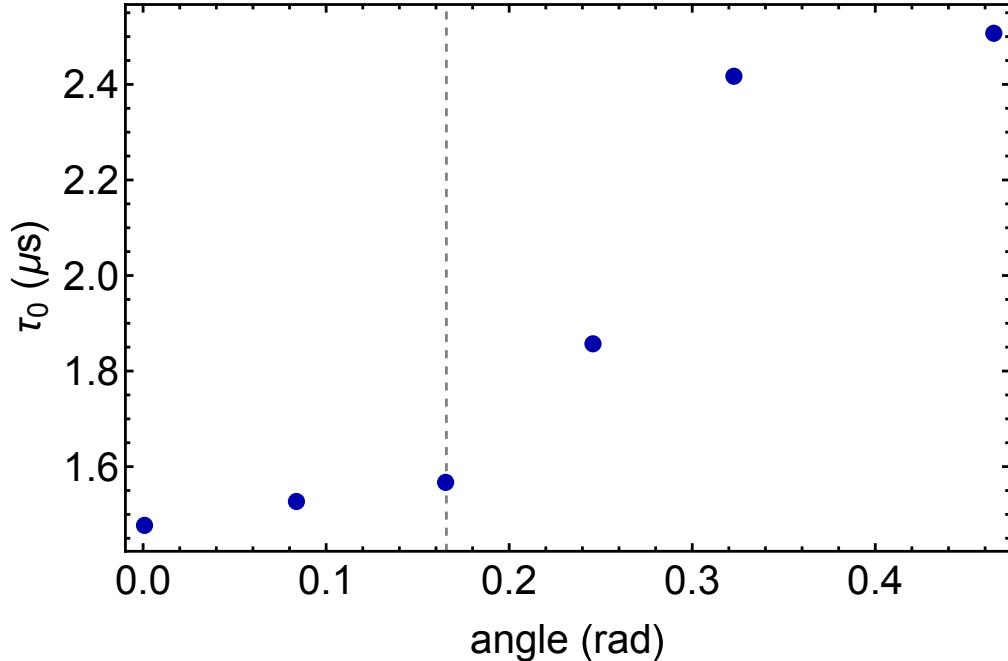


Figure 4.8: Simulated correlation function width vs. sampling angle range for an atomic temperature of  $90 \mu\text{K}$ . The dashed gray line indicates the critical angle  $\arctan(1/6)$  in the simulation at which not all atoms hit the fiber.

netic field gradient that persists during time of flight, slightly compressing the MOT and modifying the TOF. This leads to a systematically lower measured atom temperature, so the apparent gap between theory and experiment should be smaller. Uncertainty in the fiber diameter also affects the characteristic transit time of an atom through the mode, as indicated by the open circles in Fig. 4.9. We performed the same simulation for an atomic cloud temperature of  $240 \mu\text{K}$  and fiber diameters of 450 nm (green circle) and 550 nm (brown circle), which represent the diameters at the stated lower and upper uncertainty bounds. We have observed that fibers can have systematically larger diameters than our design due to the flame pushing the thin fiber at the end of a pull [74]. This suggests a potentially better agreement between experiment and simulation. Even so, the 30% difference between the experimental data and the lower confidence band of the fit to simulated data is comparable to other temperature measurement methods using optical

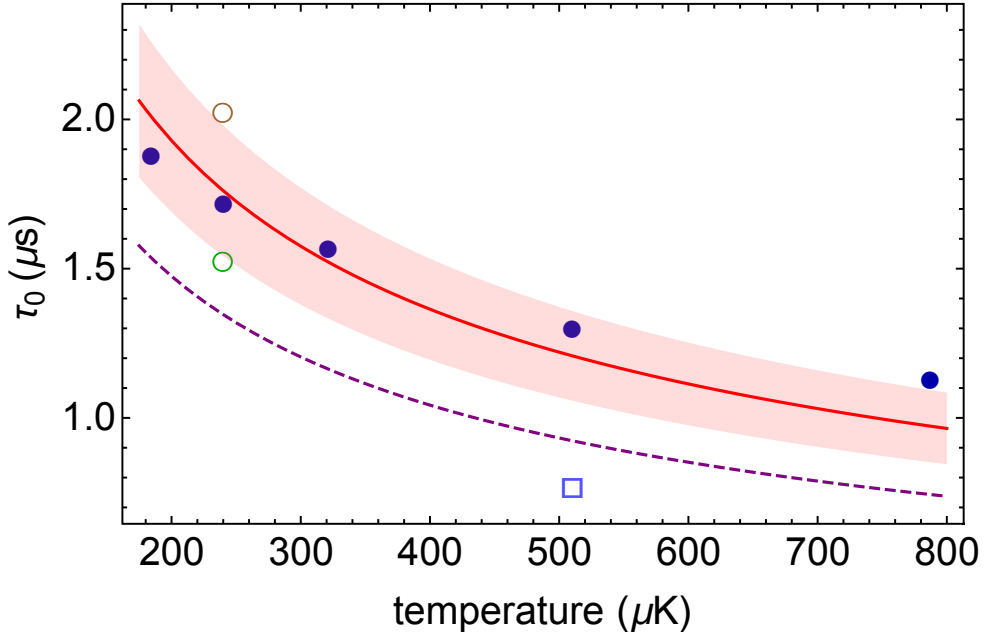


Figure 4.9: Simulated correlation function width vs. atom temperature. The red line is a fit to the simulated data (blue dots) using Eq. 4.10, with the shaded areas representing 95% confidence bands. The open circles represent a sensitivity analysis of the fiber diameter, plotting the transit time for a temperature of  $240 \mu\text{K}$  and diameter of 450 nm (brown) and 550 nm (green). The open square is a sensitivity analysis of the angular distribution, showing the transit time for the  $510 \mu\text{K}$  case for zero angular spread. The dashed purple line is the corresponding fit to experimental data shown in Fig. 4.5.

nanofibers [129].

Simulations also confirm that the decay time decreases for the first few milliwatts of 1064 nm laser power, after which it saturates. The saturation originates from two effects: the interplay of faster speeds and longer trajectories, and atomic level shifts due to surface and dipole potentials. While the atoms attain faster speeds due to the increasing strength of the attractive potential for higher laser power, they experience a larger number of orbiting trajectories that increase the interaction distance. These classical dynamics partially offset each other, but do not fully account for the saturation we see in the data. The light shifts alter the probability to absorb a photon from the MOT beam in such a

way that the interaction region broadens relative to the nanofiber mode structure.

## 4.6 Conclusions

We have presented a technique to measure the temperature of a laser-cooled atomic cloud that is applicable to experiments with restrictive environments, such as hybrid quantum systems using superconducting circuits. The method uses intensity autocorrelation functions to extract dynamics of atoms as they pass through the ONF mode and is easily extendable to other photonic devices with different optical mode geometries. This mapping of mode structures could be useful when using the next family of higher-order modes to trap atoms near an optical nanofiber [88, 130–133].

## Chapter 5: Measurement of the lifetime of the $5P_{3/2}$ state of $^{87}\text{Rb}$ near a nanofiber

Correlation measurements need not be restricted to intensity autocorrelations. We can instead correlate photon arrivals with a given trigger event to measure the spontaneous decay of an atom, a method already employed to great accuracy with, for instance, rubidium [134], cesium [135], and francium [136]. In this chapter we apply this technique to measure the lifetime of the  $5P_{3/2}$  state of  $^{87}\text{Rb}$  near an optical nanofiber.

A dielectric surface modifies the dipole moment of a proximal atom, in turn changing its rate of spontaneous emission [137, 138]. Moreover, the mode structure of a waveguide enhances the decay rate of the atom in a manner analogous to the Purcell effect, in which the rate  $\gamma$  becomes  $\gamma(1 + 2C)$  (where  $C$  is the cooperatively discussed in Chap. 1). The spectral properties of atomic emission near surfaces and waveguides have been studied extensively theoretically [97, 124, 138–142] and measured in the frequency domain [128, 143–147]. By using time-correlated single-photons to determine the emission rate [27], we avoid broadening issues that can complicate linewidth measurements. Our setup also allows us to measure both the free-space and fiber-modified rates so that we can make a direct comparison with the same method, mitigating the influence of systematics.

## 5.1 Theoretical overview

We first present the familiar result of spontaneous emission for an atom in free space, as it will inform our discussion about how the presence of a nanofiber can change this rate. Fermi's Golden Rule states that for an atom spontaneously decaying into a continuum of states, the transition rate  $W_{fi}$  between some initial state  $|i\rangle$  and a final state  $|f\rangle$  is

$$W_{fi} = \frac{2\pi}{\hbar} |\langle f | H_{int} | i \rangle|^2 \rho_f(\hbar\omega_0), \quad (5.1)$$

where  $H_{int}$  is the interaction Hamiltonian between the electromagnetic field and the atom,  $\rho_f$  is the density of final states, and  $\hbar\omega_0$  is the transition energy between states  $|i\rangle$  and  $|f\rangle$ . Note that we have already integrated over the possible photon energies. Evaluating Eq. 5.1 in free space for a transition between states of electron angular momentum  $J$  and  $J'$  yields

$$\gamma_0 = \frac{\omega_0^3}{3\pi\varepsilon_0\hbar c^3} \frac{|\langle J || D || J' \rangle|^2}{2J' + 1}, \quad (5.2)$$

where  $\varepsilon_0$  is the permittivity of free space and  $\langle J || D || J' \rangle$  is the reduced electric-dipole matrix element, and we have taken into account the two polarizations. For  $^{87}\text{Rb}$ , this evaluates to  $\tau_0 = 1/\gamma_0 = 26.24$  ns [123].

Fermi's Golden Rule contains two factors that can be modified by the presence of the fiber: the interaction Hamiltonian matrix element and the density of states. The interaction Hamiltonian within the dipole approximation takes the form  $H_{int} = -\mathbf{d} \cdot \mathbf{E}$ . The proximity of the dielectric surface modifies the dipole moment  $\mathbf{d}$ , which we discuss in the next section. A waveguide and its mode structure alter the decay rate in three ways. First it decreases the mode volume of the quantized electric field,  $|\mathcal{E}| = \sqrt{\frac{\hbar\omega}{2\varepsilon_0 V}}$ , leading

to a stronger single-photon electric field strength. Secondly the new dimensionality of the waveguide changes the density of states, which scales as  $\omega^{\mathcal{D}-1}$ , where  $\mathcal{D}$  is the system dimension. And finally the dispersion relation changes due to the non-unity propagation constant of a mode in the waveguide. These issues will be addressed in Sec. 5.1.2.

### 5.1.1 Dipoles near surfaces: calculating $\gamma_{\text{rad}}$

When a radiating dipole is brought near a surface, the reflection and absorption of the radiated field will modify the decay of the dipole [137, 138, 148]. Consider an two-level atom (modeled as a classical dipole) in a medium with dielectric constant  $\varepsilon_1$  placed a distance  $d$  away from an infinite dielectric surface (with dielectric constant  $\varepsilon_2$ ). Calculating the decay rate of this atom amounts to finding the reflected electric field at its location. Refs. [138–140] solve Maxwell's equations and the appropriate boundary conditions to arrive at the following rates for a dipole oriented either parallel or perpendicular to the dielectric:

$$\frac{\gamma_{\text{rad}}^{\parallel}}{\gamma_0} = 1 + \frac{3}{4} \text{Im} \left[ \int_0^{\infty} d\kappa \frac{\kappa}{\mu_1} (R_{\perp} + \mu_1^2 R_{\parallel}) e^{-i2\mu_1 d} \right] \quad (5.3)$$

$$\frac{\gamma_{\text{rad}}^{\perp}}{\gamma_0} = 1 - \frac{3}{2} \text{Im} \left[ \int_0^{\infty} d\kappa \frac{\kappa^3}{\mu_1} R_{\parallel} e^{-i2\mu_1 d} \right], \quad (5.4)$$

where  $\mu_{1,2} = \sqrt{\varepsilon_{1,2}/\varepsilon_0 - \kappa^2}$ , the reflection coefficients  $R_{\parallel}$  and  $R_{\perp}$  are given by

$$R_{\parallel} = \frac{\varepsilon_1 \mu_2 - \varepsilon_2 \mu_1}{\varepsilon_1 \mu_2 + \varepsilon_2 \mu_1} \quad (5.5)$$

$$R_{\perp} = \frac{\mu_1 - \mu_2}{\mu_1 + \mu_2}, \quad (5.6)$$

and  $\hat{d}$  is a normalized distance scaled by the wavelength of the radiation and the index of refraction of medium 1,  $n_1 = \sqrt{\varepsilon_1/\varepsilon_0}$ ,

$$\hat{d} = \frac{2\pi}{\lambda} \sqrt{\frac{\varepsilon_1}{\varepsilon_0}} d. \quad (5.7)$$

Fig. 5.1 displays the evaluation of Eqs. 5.3 (blue curve) and 5.4 (red curve) for a  $^{87}\text{Rb}$  near a fused silica surface [121] (see Appendix C for a discussion of the index of refraction of fused silica). The oscillations in the scattering rates arise from interferences between the original radiated field and the reflected one, with length scale given by  $\lambda/2\pi$ . This calculation ignores absorption (i.e. non-radiative corrections to  $\gamma$ ), which would cause a the atomic lifetime to go to zero at small distances [138]. This is an important effect, but because the van der Waals potential accelerates atoms as they approach the fiber surface, their interaction time in this regime is negligible [121].

### 5.1.2 Dipoles near waveguides: calculating $\gamma_{1D}$

We will briefly outline the derivation for a two-level atom near a waveguide presented in [125], introducing definitions for the sake of notational clarity and considering only the fundamental  $\text{HE}_{11}$  mode. Refs [97, 124] provide a more complete treatment for multilevel atoms, but their complicated analysis is beyond the scope of the discussion here.

We decompose the electric field  $\mathbf{E}$  into quantized modes of the nanofiber as

$$\mathbf{E} = \sum_k \mathcal{E}_k a_k + \text{h.c.}, \quad (5.8)$$

where  $k$  represents the mode index,  $a_k$  is the single-photon annihilation operator in mode  $k$ , and  $\mathcal{E}_k$  is the single-photon electric field of mode  $k$ . The electric fields have the form [105,

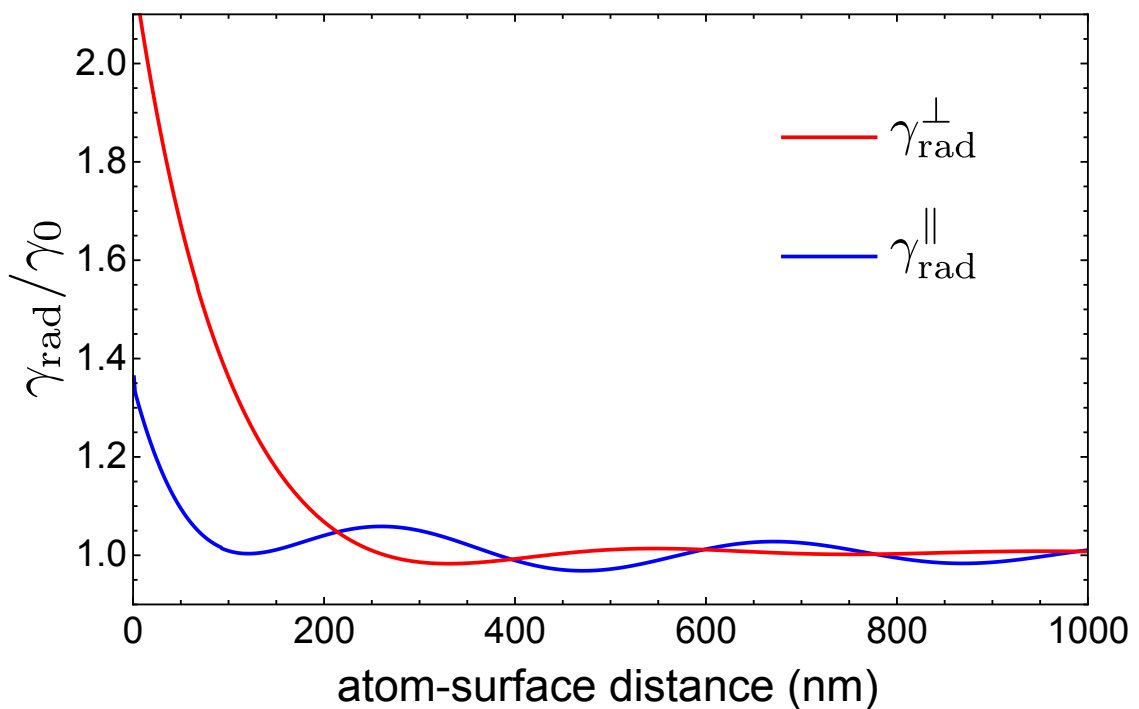


Figure 5.1: Radiative decay rate (normalized to the free-space rate  $\gamma_0$ ) of an atomic dipole with resonant wavelength  $\lambda = 780$  nm near a fused silica surface. The two curves represent perpendicular (red) and parallel (blue) orientations of dipole relative to the silica surface.

$$\mathcal{E}_k = i\sqrt{\frac{\hbar\omega_k}{2\varepsilon_0 L}} \tilde{\mathcal{E}} e^{i(\beta_k z + m\varphi)}, \quad (5.9)$$

where now the quantization box is only one-dimensional and has length  $L$ ;  $\tilde{\mathcal{E}}$  represents the normalized electric field of the nanofiber mode, carrying both spatial and polarization information;  $\beta_k$  is the propagation constant of mode  $k$  (see Appendix A); and  $m$  represents the angular momentum of the mode (classically, the handedness of the mode polarization).

Carrying out the standard Wigner-Weisskopf treatment of spontaneous emission, we arrive at the following equation for the spontaneous emission rate into the fundamental mode

$$\gamma_{1D} = \gamma_0 \times \frac{3\lambda^2\beta'}{8\pi} |\tilde{\mathcal{E}}|^2, \quad (5.10)$$

where  $\beta' = d\beta/dk$  is the derivative of the propagation constant with respect to wavenumber. Note that the factor  $3\lambda^2/2\pi$  represents the resonant cross section of a two-level atom. That the dependence on the propagation constant is given only by  $\beta'$  is a consequence of the system being one-dimensional.

We plot Eq. 5.10 in Fig. 5.2, normalized to the free-space value  $\gamma_0$ , for a  $^{87}\text{Rb}$  atom near a nanofiber with radius  $r_0 = 250$  nm. It reaches a maximal value of  $0.18\gamma_0$  at the fiber surface and decays to zero with radial dependence determined by the mode intensity  $|\tilde{\mathcal{E}}|^2$  (see Appendix A). For atoms trapped 200 nm away from the fiber, the corresponding increase in the decay rate due to guided-mode coupling is around 1 – 2%.

### 5.1.3 Atom density near surfaces

The modifications to spontaneous emission discussed in Secs. 5.1.1 and 5.1.2 are position-dependent relative to the nanofiber, and so we must have knowledge of the po-

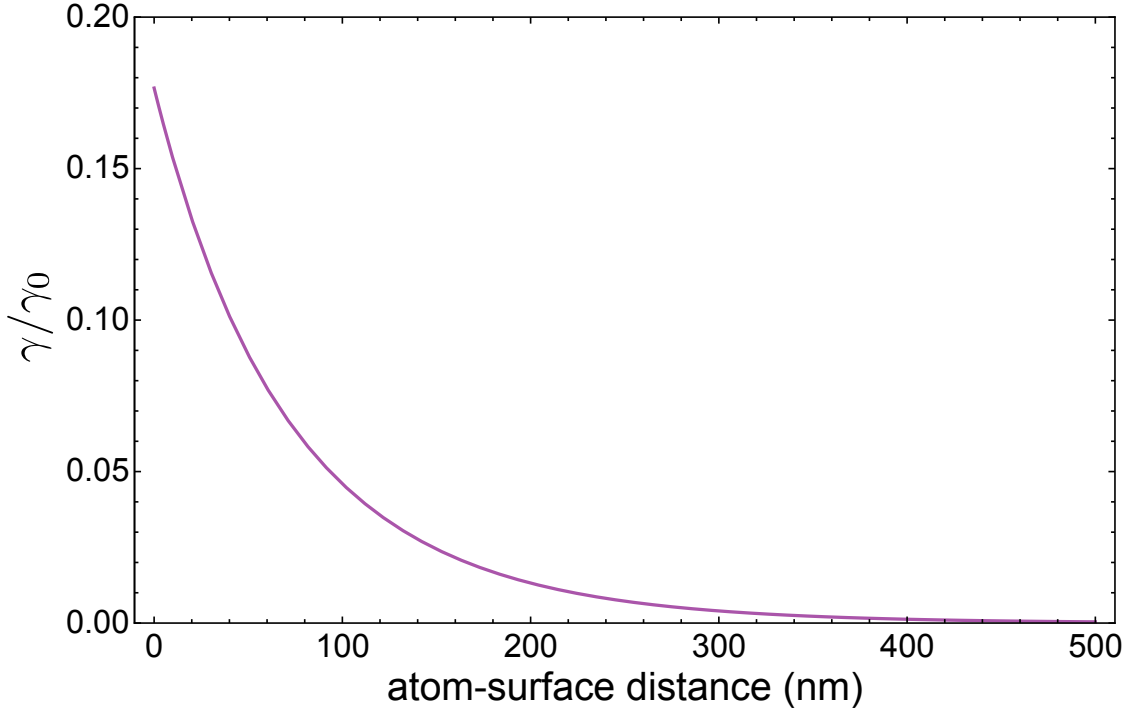


Figure 5.2: Radiative decay rate (normalized to the free-space rate  $\gamma_0$ ) of a  $^{87}\text{Rb}$  atom into a 500-nm diameter optical nanofiber.

sition distribution of atoms over which to average these effects. Of course, the nanofiber trap localizes the atoms to a particular separation from the nanofiber surface, with some dispersion in the position due to quantum mechanical and thermal effects. A first measurement in the pursuit of the changes for a trapped atom is to use a thermal distribution, then understanding this it will be possible to move in the future to measurements with trapped atoms.

Ref. [126] provides a thorough theoretical treatment of the problem, considering quantum-mechanical scattering of atoms off of the surface potential. We will instead focus on a classical motivation followed by a thermodynamic derivation of the population distribution, discussing why this is valid given our atom temperatures and comparing to the quantum results in [126].

The potential arises from a van der Waals interaction between the silica surface and

the atom, mediated by virtual photon pair exchange between two dipoles (REF). At larger distances from the fiber, the van der Waals interaction transitions to a Casimir-Polder interaction, which takes into account retardation effects in this virtual photon exchange. An approximate way to smoothly connect these two regions is given by [126, 142]

$$U(r) = -\frac{C_4}{r^3 (r + C_4/C_3)}, \quad (5.11)$$

where  $r$  is the radial distance of the atom from the fiber surface, and  $C_3 = 746 \text{ Hz} \cdot \mu\text{m}^3$  and  $C_4 = 67 \text{ Hz} \cdot \mu\text{m}^4$  are the van der Waals and Casimir-Polder coefficients for  $^{87}\text{Rb}$  and fused silica, respectively (see Appendix C). Note that Eq. 5.11 ignores the short-range, repulsive wall included in Ref. [126], as we are not considering quantum reflections off of the silica surface.

This attractive potential accelerates atoms as they approach. As a result of the increased speed of the atoms, the atomic density near the fiber decreases. To quickly illustrate this fact, consider a flux of atoms,  $\Phi$  moving with an average velocity  $v$  in the  $x$ -direction. Then the density of atoms is given by  $\Phi/v$ , so that the density is inversely proportional to their velocity.

In order to quantify this change of density, consider the ideal gas law:

$$PV = Nk_B T, \quad (5.12)$$

where  $P$  is the pressure,  $V$  is the volume of our system,  $N$  is the number of atoms,  $k_B$  is Boltzmann's constant, and  $T$  is the system temperature. Assuming constant pressure, any change in thermal kinetic energy,  $k_B T$ , must be balanced by an opposite change in the local atomic density,  $\rho = N/V$ . Denoting the total energy of an atom by  $E$ , we can

write it as a sum of the potential and kinetic energy in the system,  $E = k_{\text{B}}T + U(r)$ , with  $U(r)$  being the surface potential in Eq. 5.11. Then Eq. 5.12 can be recast as

$$P = \rho(E - U(r)) . \quad (5.13)$$

We now solve for the density, and normalize it such that it equals one at large distance - we can safely assume that the MOT cloud density is constant far away from the fiber surface, as its size ( $\sim \text{mm}$ ) is much larger than length scale over which the atom-fiber coupling is appreciable ( $< \mu\text{m}$ ). This yields

$$\tilde{\rho}(r) = \frac{1}{1 - U(r)/E} , \quad (5.14)$$

where  $\tilde{\rho}(r)$  is the normalized position density. Fig. 5.3 displays a plot of this function for an atom temperature of  $200 \mu\text{K}$ , and we can see the sharp decrease in density near the surface, as expected. Comparing this treatment to the exact quantum-mechanical results of Ref. [126], we see that it follows the average of their oscillatory solutions quite well for typical MOT temperatures (tens to hundreds of microKelvin). The oscillations are so rapid in space because of the short de Broglie wavelength,  $\lambda = 2\pi\hbar/\sqrt{2m[E - U(r)]}$  ( $\approx 17 \text{ nm}$  at a distance of  $50 \text{ nm}$  and temperature of  $200 \mu\text{K}$ ), and ignoring them is justified.

#### 5.1.4 Expected decay rate

The measured decay rate will be an average of the position-dependent rates calculated above, weighted by the population density of the atoms. Writing this average yields

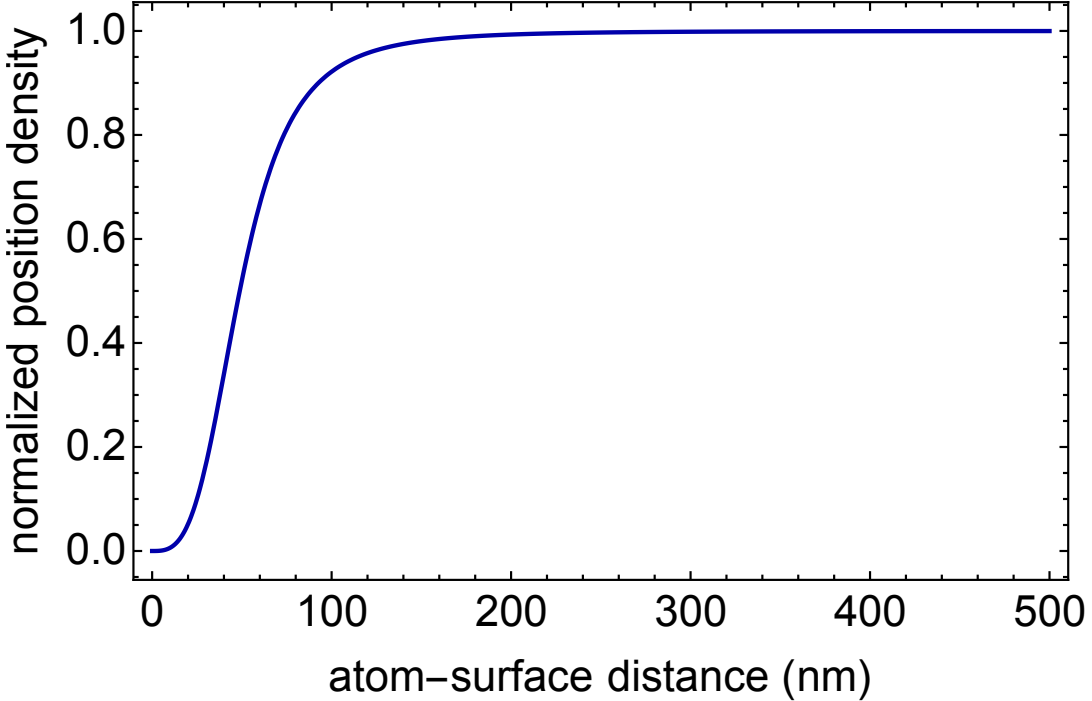


Figure 5.3: Position density of thermal rubidium atoms ( $T = 200 \mu\text{K}$ ) near a silica surface.

$$\frac{\gamma'}{\gamma_0} = \frac{\int dr (\gamma_{1\text{D}} + \gamma_{\text{rad}}) \eta(r) \tilde{\rho}(r) p_{\text{abs}}(r)}{\int dr \eta(r) \tilde{\rho}(r) p_{\text{abs}}(r)}, \quad (5.15)$$

where  $\eta(r) = \gamma_{1\text{D}}(r)/\gamma_{\text{tot}}(r)$  defines the coupling efficiency into the guided mode, and  $p_{\text{abs}}(r)$  is the probability for an atom to absorb a photon from probe pulse. This absorption probability depends on the atom-fiber separation, as the van der Waals interaction shifts the atomic levels out of resonance with the driving beam (see Sec. 4.3.3).

## 5.2 Experimental setup

The experiment employs the same 500-nm diameter fiber used for the measurements presented in Chaps. 3 and 4. A MOT is prepared around the nanofiber waist, as shown in Fig. 5.4. The MOT and repump beams are extinguished by turning off the RF power

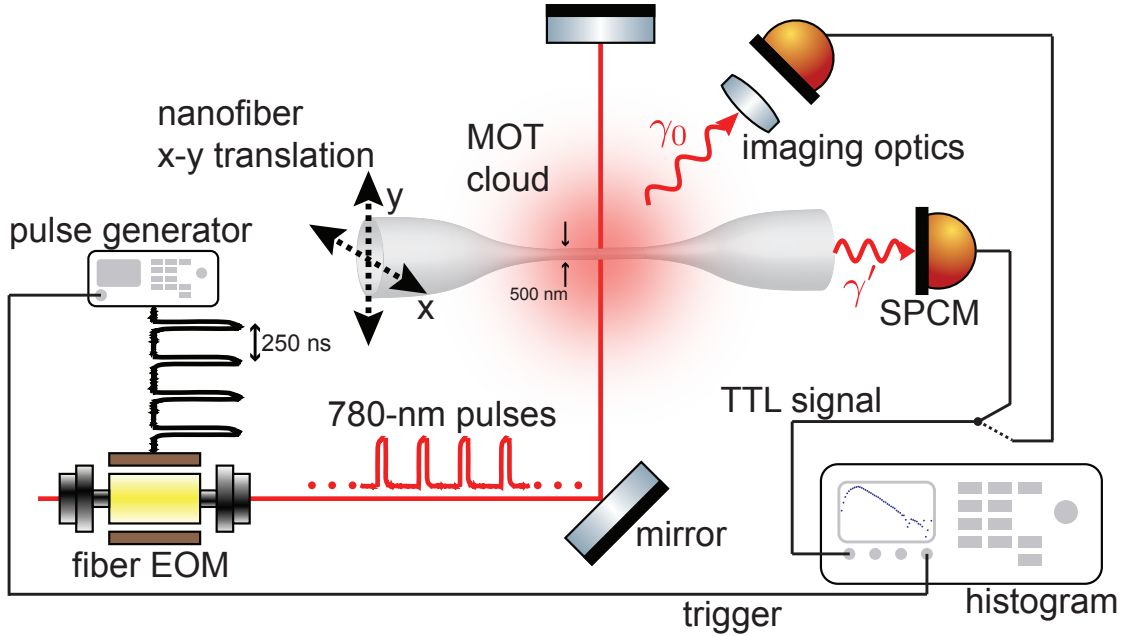


Figure 5.4: Schematic for the atomic lifetime measurement. Resonant pulses 50 ns in length are generated via a fiber EOM and interact with atoms in the MOT. We detect free-space decay ( $\gamma_0$ ) by moving the nanofiber out of the cloud and collecting photons on a SPCM from the side. The fiber-modified decay ( $\gamma'$ ) is measured through the nanofiber.

to their respective AOMs, with the repump kept on for a few microseconds longer to replenish any atoms that fell into the dark  $F = 1$  state. After ~~we trigger~~ the repump ~~to turn off~~, we wait 500  $\mu$ s for the background light from these beams to go below 1% of their “on” levels (see Fig. 5.5). The pulsing sequence then begins. A digital delay generator (Stanford Research Systems DG645) outputs a train of 50-ns-wide square pulses with a repetition rate of 4 MHz. These pulses are sent to a fiber-EOM (EOSPACE AZ-2K1-10-PFA-PFA-800-UL) in a Mach-Zehnder configuration that is locked to the null point by a microcontroller (YY Labs), which feeds back to the EOM bias port. The electronic pulse amplitude, roughly 2.3 V, is chosen to drive a 180° phase shift in the EOM and maximize the optical pulse size. Light for the optical pulses originates from our cooling laser, and the AOM used for switching also sets the frequency so that the light is on resonance.

The probe beam bath is orthogonal to the nanofiber waist in order to minimize coupling of probe photons into the guided mode and to the detector. We also have a mirror to retroreflect the beam, which helps to keep the atoms in the region of interest near the nanofiber for longer periods of time. The train of pulses repeats for 1 – 2 ms before the cooling and repump beams turn back on for 15 – 25 ms to reload the MOT before the next measurement sequence (see Fig. 5.5). The SPCMs are gated to take data only during the pulse sequence, and we maintain low count rates ( $\lesssim 10^4 \text{ counts} \cdot \text{s}^{-1}$ ) to avoid photon pileup [149, 150].

~~There are different approaches to histogramming the arrival times of the photon pulses, here the sync output from the delay pulse generator triggers our oscilloscope (Tektronix DPO7054, see Chap. 2) to start the histogram, which correlates the decay measurement with a known start time. We typically use a bin size of 5 ns, which balances well our measurement resolution with the necessary averaging time to accumulate good statistics.~~

Measuring the free-space decay follows the same general procedure, except the photons are collected with an imaging system that couples to the multimode fiber for the SPCM (see Fig. 5.4 as well as Fig. 2.18, where the polarizer and PD are replaced with fiber-coupling optics). We also use the UHV manipulator to move the nanofiber out of the MOT and the imaging plane of the optical system so that the fiber will not influence the atomic decay or scatter probe light into the detection path.

For all measurements, the size and density of the MOT is reduced by lowering the magnetic field gradient and the current of the atomic dispensers. Lowering the optical thickness of the sample allows us to minimize radiation trapping effects [151], which can artificially lengthen the apparent lifetime of the atom due to multiple, successive absorption and emission events before photon detection. The parameters for normal, nanofiber-

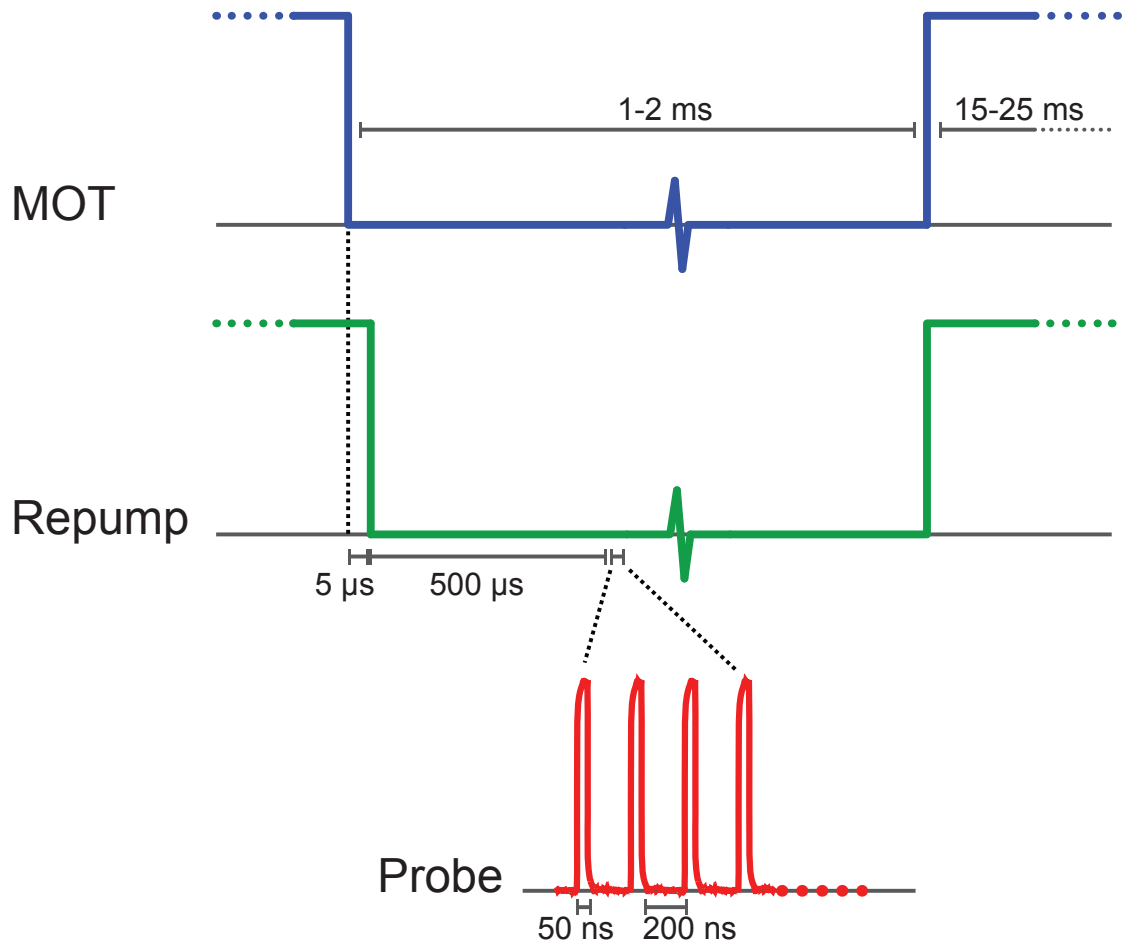


Figure 5.5: Timing sequence for MOT (blue), repump (green), and probe (red) light to conduct lifetime measurements. The MOT and repump beams are turned off within  $10 \mu\text{s}$  of one another, and there is a delay before the pulsing begins. 50-ns-wide pulses with a repetition rate of 4 MHz excite the atoms for  $1 - 2 \text{ ms}$  before the MOT is loaded again ( $15 - 25 \text{ ms}$ ). The relevant timescales are denoted for clarity.

trapping conditions (Chap. 3) yields measured lifetimes of  $\sim 32$  ns, so we decrease the optical thickness until we achieve measurements close to the accepted value of 26.23 ns.

### 5.2.1 Optical pulse generation and improvement

We use fiber EOMs to generate short ( $\sim$ ns) pulses with low-voltage drivers, which are a mature technology from the telecommunications industry. The curve in Fig. 5.6 is a fast photodiode signal of a 50-ns pulse at the output of the EOM. A “foot” at the level of 10% between 50 and 80 ns is clearly visible. While the structure on the rising edge is unimportant to us, lifetime measurements of this nature require as clean of a falling edge as possible so that the decay is “free” and can be fit easily by an exponential. Mathematically, the detected signal,  $f(t)$ , is a convolution of the excitation and the expected decay:

$$f(t) = \epsilon(t) \otimes (e^{-\gamma t} \Theta(t)) , \quad (5.16)$$

where  $\epsilon(t)$  is the excitation applied to the atom,  $\otimes$  denotes convolution,  $\gamma$  is the expected decay rate, and  $\Theta(t)$  is the Heaviside function.

The limited input power ( $< 10$  mW) and low efficiency ( $\sim 10\%$ ) of this model of EOM do not allow for concatenating devices in series to suppress low-amplitude artifacts and still have usable power at the output. We successfully use a wideband analog pulse multiplier (Analog Devices ADL-5391) to suppress undesired structure in the electronic pulses from the delay [pulse](#) generator. The quality of the optical pulses, however, is limited by the EOM itself, so the improvement in electrical pulses did not result in a proportional improvement optically. We are currently exploring optical alternatives to the fiber-EOM, such a double-passed AOM in bowtie path to produce zero frequency shift, that can

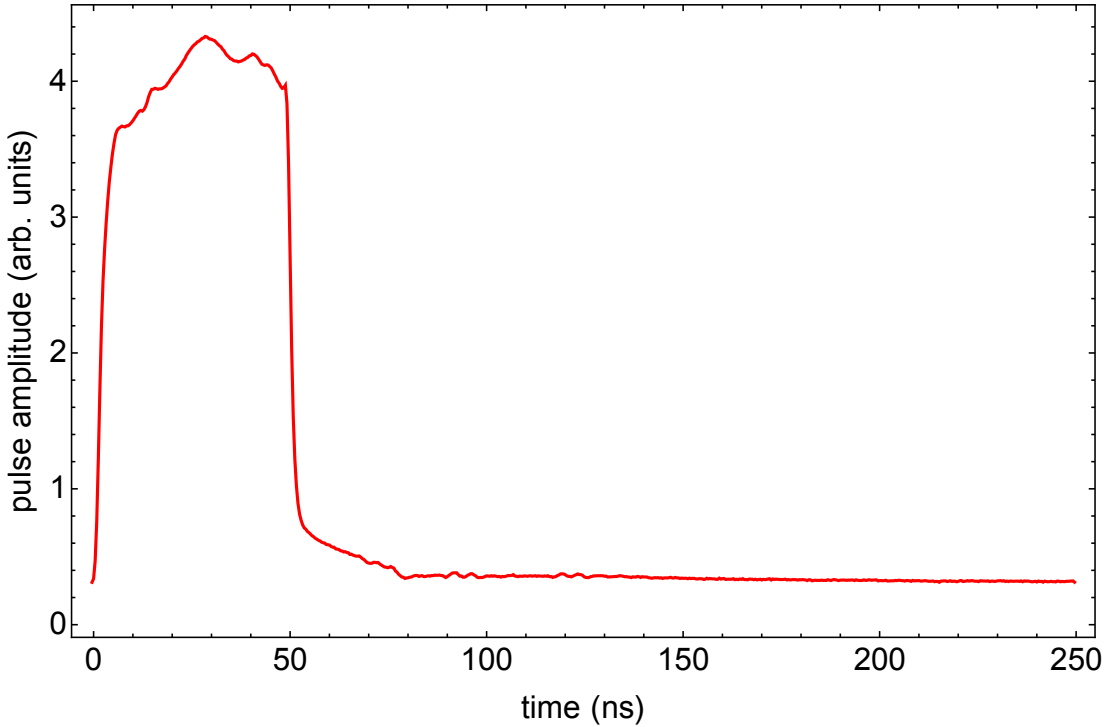


Figure 5.6: Optical pulse at the output of the fiber-EOM, driven by the delay pulse generator and measured on a fast photodiode.

generate clean, fast pulses from a CW source.

### 5.3 Data and results

Our analysis relies on exponential fitting of the decay, which measures a statistically significant difference between the free-space and fiber-modified cases, but does not capture all of the physics due to imperfect pulse shapes. We collect data until the difference between signal and background is more than  $10^4$  counts per 5-ns bin. Analyzing the background for both the fiber and free-space configurations, we find that the background is flat, so background subtraction is done primarily for better visualizing the decay in the plots. We assume that the statistical uncertainty of each data point is  $\sqrt{N_i}$ , where  $N_i$  is the number of counts in bin  $i$ , and we use this to properly weight the fits.

### 5.3.1 Exponential fitting

Free atomic decay follows an exponential with an offset due to background counts:

$$f(t) = A \exp\left(-\frac{t-t_0}{\tau}\right) + B. \quad (5.17)$$

In order to effectively fit only this free decay, we start our fits at least a few time bins after the end of the 50-ns excitation pulse. We choose the start and end points of the fit such that they result in the reduced chi-squared closest to 1 and so that they are in a regime where the extracted value of  $\tau$  is least sensitive to truncation [152]. Figs. 5.7 and 5.8 display both the data (points) and fits (red lines) for the free-space and fiber-modified case, respectively. We extract timescales of  $\tau_0 = 26.5 \pm 0.8$  ns and  $\tau' = 24.6 \pm 0.2$  ns for the respective measurements. Our free-space measurement agrees well with the reported value of  $\tau_0 = 26.20 \pm 0.09$  ns reported in Ref. [134], which contains a much more detailed analysis of systematic errors.  will then use this literature value to compare our fiber-modified measurement. This yields a ratio of decay rates of

$$\frac{\gamma'}{\gamma_0} = 1.065 \pm 0.009. \quad (5.18)$$

This compares with a theoretical prediction of 1.07 from the analysis in Sec. 5.1.4. In calculating this number we assume that the atoms are primarily parallel to the fiber surface, as our probe beam was linearly polarized in that orientation, preferentially driving the atoms to align this way. If we orient the polarization of the probe to be orthogonal to the fiber, then the effect will be averaged over the two polarization contributions, and the enhancement can be as high as 19%.

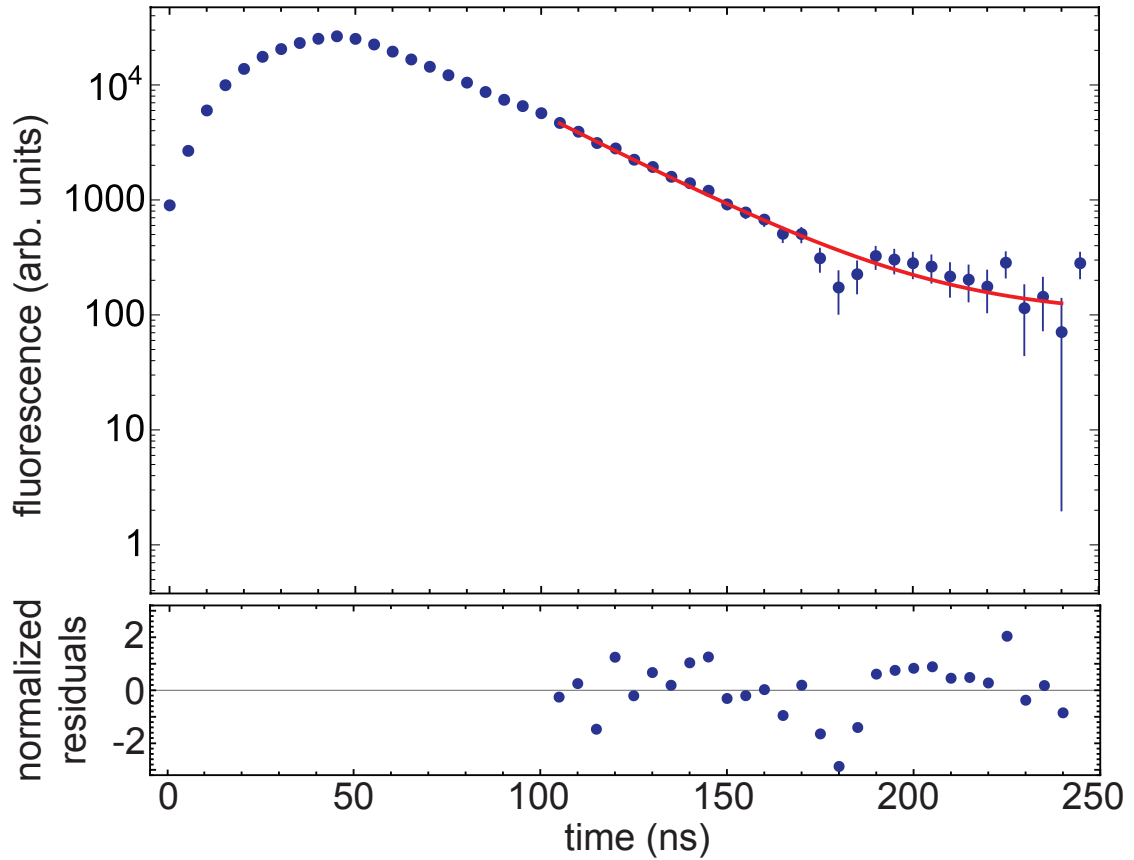


Figure 5.7: Histogram of the free-space decay measurement with bin size of 5 ns. The red line is a fit to Eq. 5.17, with  $(\chi^2)_{\text{red}} = 1.26$ . The bottom plot displays the normalized residuals.

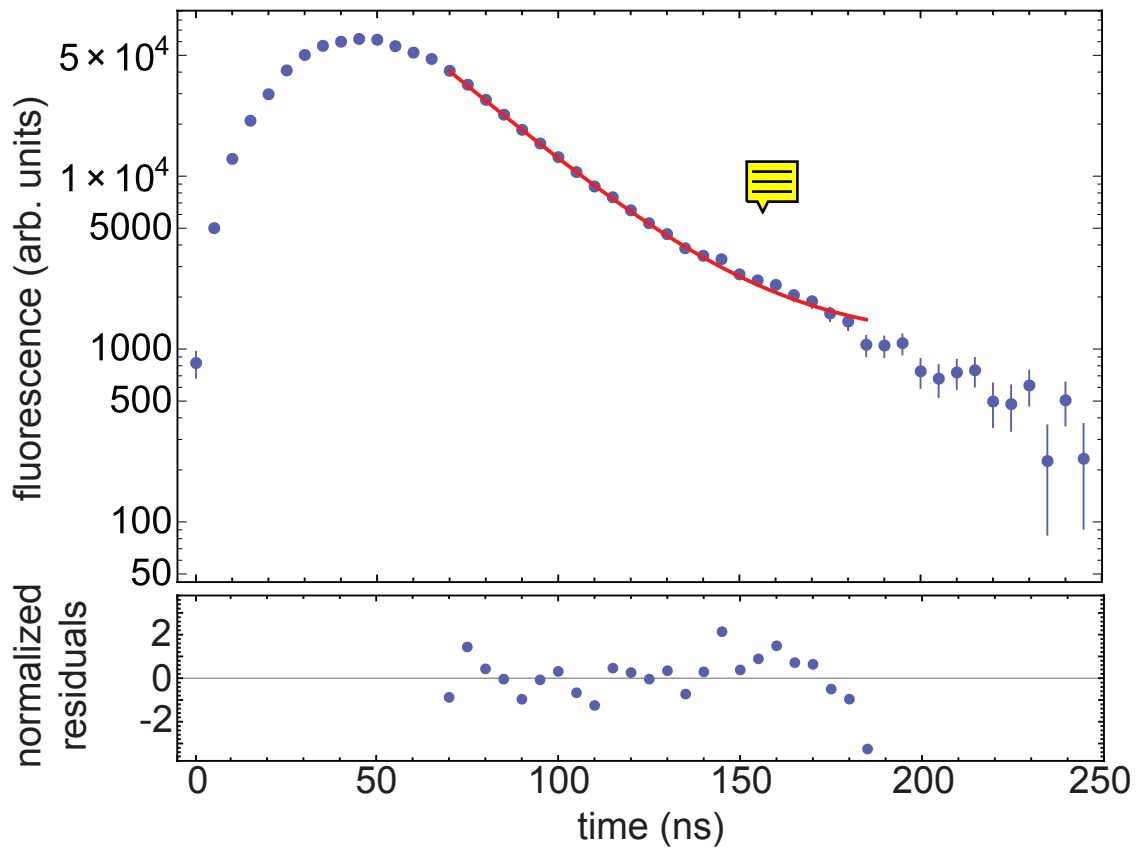


Figure 5.8: Histogram of the fiber-modified decay measurement with bin size of 5 ns. The red line is a fit to Eq. 5.17, with  $(\chi^2)_{\text{red}} = 1.45$ . The bottom plot displays the normalized residuals.

## 5.4 Conclusions

We have directly observed Purcell enhancement of spontaneous emission into the guided mode of an optical nanofiber. While previous experiments have inferred this effect by measuring the spectral linewidth of atoms near a dielectric, this is a direct measurement in the time domain. Our observation of a  $6.5 \pm 0.9\%$  enhancement is consistent with the theoretical prediction of 7%, which takes into account radiative and guided-mode corrections, as well as the density of a thermal distribution of atoms near a silica surface.

Future experiments could explore how the spontaneous emission rate increases as the fiber diameter decreases, as shown in Fig. 5.9. There exists an optimal fiber radius of  $a \sim 0.23\lambda = 180$  nm for the coupling rate at the fiber surface. Not only will this smaller fiber make our measured effect more pronounced, but the increased coupling strength opens the door for studying interesting collective physics (see Sec. 7.4) [27].

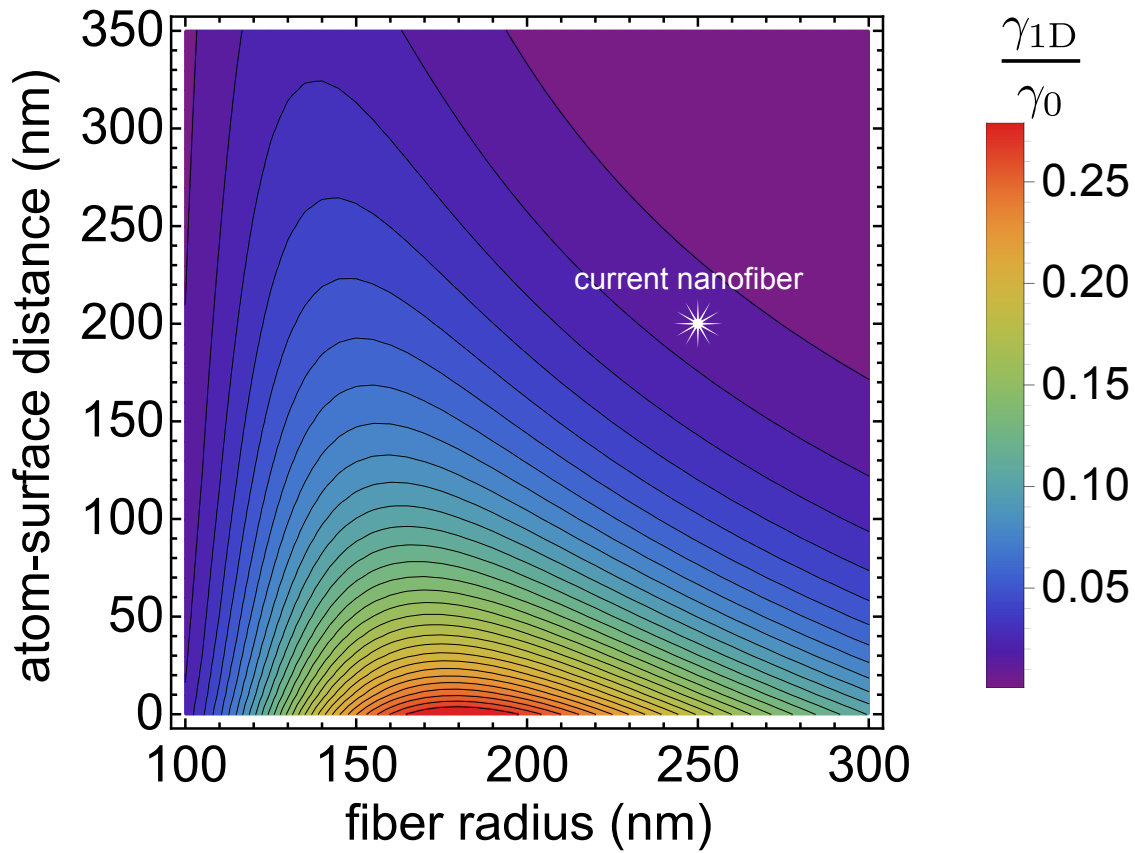


Figure 5.9: Contour plot of  $\gamma_{1D}$  as a function of fiber size and atom-fiber distance. The white star marks the parameters of the nanofiber used in this thesis (with the atom-fiber separation being the typical trap distance).

## Chapter 6: Quantum hybrid system

This thesis presents a part of an overall project whose aim is to coherently couple an atomic ensemble with a superconducting circuit. Optical nanofibers aid this end by providing an atom trap that is in principle compatible with cryogenic systems. They are, however, just one element of the final system. We need a method to introduce rubidium atoms to the 10-mK stage of the dilution refrigerator without putting an undue heat load on the system. These atoms must also be trapped and cooled before they are loaded onto the nanofiber and transported to the superconductor; this necessitates a MOT in some form. Finally, the superconductor and nanofiber must be aligned and positioned to within 10  $\mu\text{m}$  of one another in an environment with no optical access.

Fig. 6.1 represents one conception of what the final system might look like. Atoms are introduced via a cold atomic beam generated from an imbalanced MOT at room temperature. Within the dilution refrigerator, a compact MOT traps and cools atoms from this beam. This MOT is spatially close to the “science” region that houses the superconducting resonator, but thermally anchored to a higher-temperature stage with cooling power on the order of a Watt (as opposed to the 100  $\mu\text{W}$  at base temperature). The nanofiber then bridges the few-cm distance between the MOT and the superconductor so that atoms can be transported to the interaction region. This chapter provides a detailed characterization of a potential compact MOT, a so-called grating-mirror MOT (GMOT).

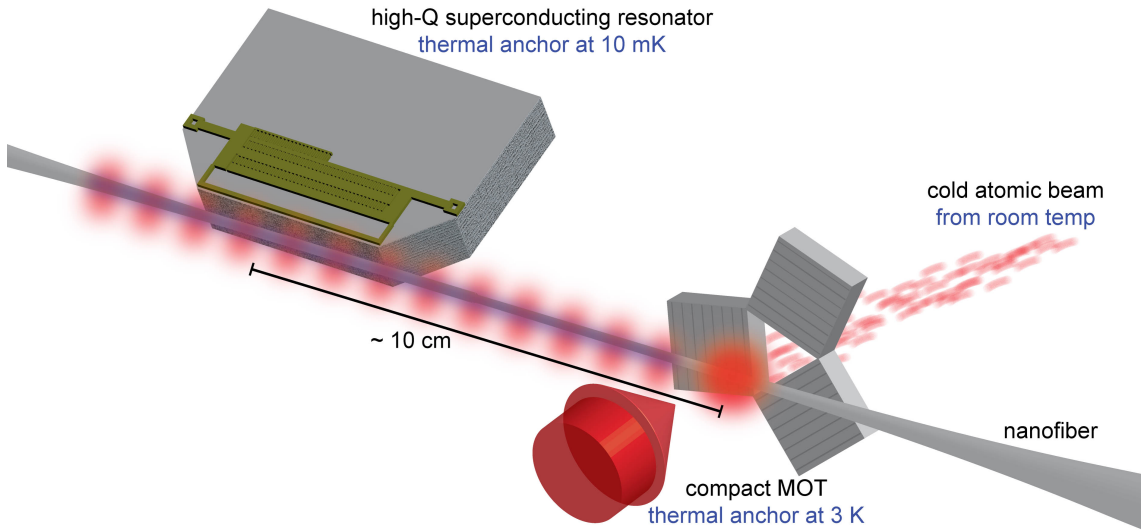


Figure 6.1: A cartoon picture of what the future hybrid system might look like. A cold atomic beam from a 2D MOT in a room-temperature chamber loads a compact grating MOT, thermally anchored to a 3 K stage in the dilution refrigerator. The GMOT transfers atoms to the nanofiber trap, and an optical conveyor belt transports the atoms to within a few micrometers of the superconducting circuit.

## 6.1 Compact atom trap: GMOT

Because the nanofiber trap is a purely conservative trap, it does not cool the atoms. A MOT provides a robust way to introduce dissipation to the system, but standard six-beam configurations are unwieldy for the confined space at the bottom of a dilution refrigerator. The first single-beam MOTs, made with an axicon or pyramid of mirrors [153, 154], are compact and minimize the number of required optical elements, but the trapping volume forms *within* the mirrors so that overlapping the cloud with a nanofiber is difficult. The tetrahedral MOT formed by three mirrors [155], on the other hand, creates a trapping volume above the plane of the mirrors. Replacing the mirrors with diffraction gratings generates the same beam geometry so that a MOT forms a few mm above the gratings [77, 156, 157]. We explore this GMOT geometry, and observe sub-Doppler cooling

despite a polarization arrangement that does not map on to the standard configurations.

### 6.1.1 Experimental setup

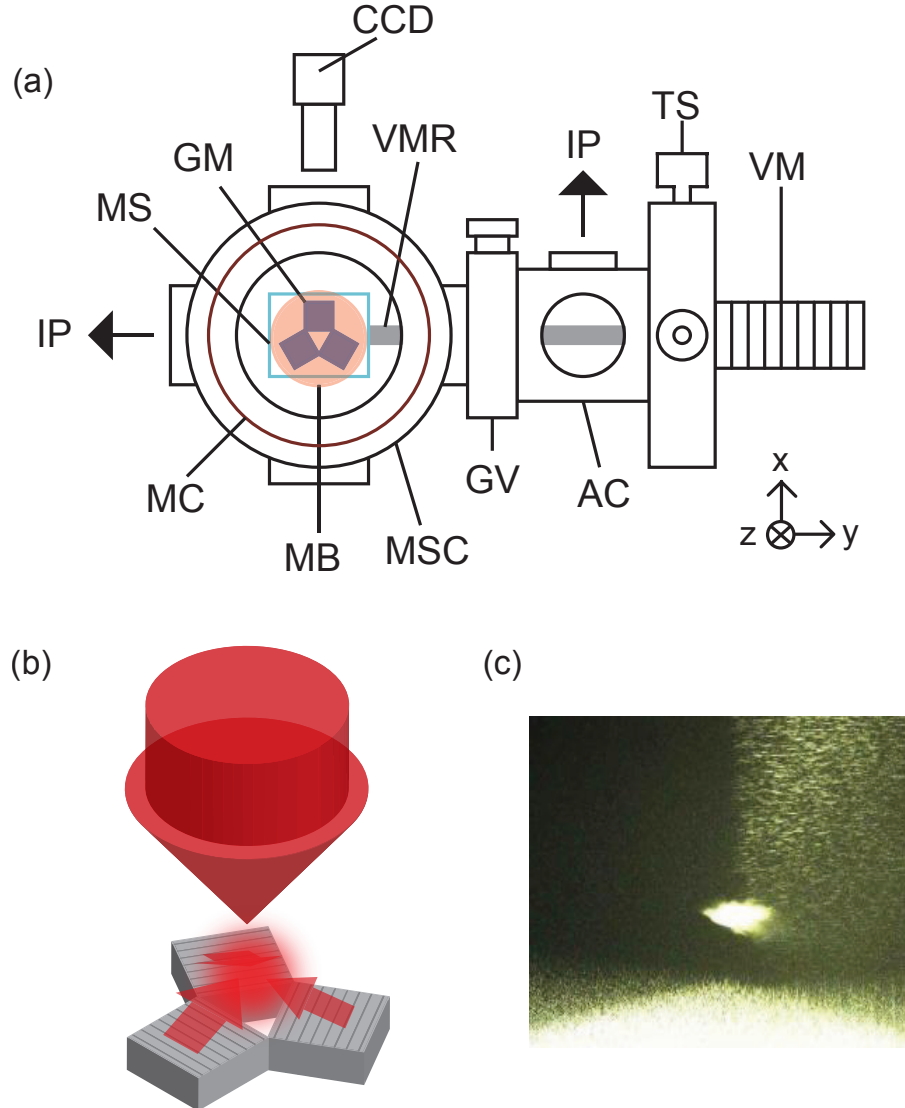


Figure 6.2: (a) Experimental setup. **AC**: Antechamber; **CCD**: CCD camera; **GM**: Grating Mirrors; **GV**: Gate valve; **IP**: Ion pump; **MB**: MOT beam; **MC**: MOT coils; **MS**: Microscope slide; **MSC**: Main science chamber; **TS**: 2-D translation stage; **VM**: Vacuum manipulator; **VMR**: Vacuum manipulator rod. (b) Single-beam GMOT configuration. (c) GMOT atom image with CCD camera. (figure from Ref. [77])

The vacuum manipulator (see Sec. 2.4.4 and Figs. 2.15 and 6.2 (a) ) holds the

gratings and can precisely adjust the position of the gratings (450 mm total z translation with  $5\text{ }\mu\text{m}$  resolution and 25 mm vectorial xy translation with  $5\text{ }\mu\text{m}$  resolution) to find the optimal magnetic field value and beam overlap to reach the lowest temperature. Fig. 6.2 (b) shows the arrangement of the three commercial gratings that we use (12.7 mm  $\times$  12.7 mm  $\times$  6 mm, Edmund NT43-752, 1200 grooves/mm). The incoming beam overlapping with the first-order reflections from the three gratings generates a capture volume of  $\sim 100\text{ mm}^3$  with a single beam that is spatially filtered with a single-mode optical fiber. Three gratings are glued on microscope slides (MS) with UV epoxy (EPO-TEK OG116-31), and the slides are attached to the support rod of the manipulator. The microscope slides are arranged such that there is a gap in the middle of the gratings to prevent reflections that cause force imbalances in the MOT. The cooling beam ( $I = 2.5\text{ mW/cm}^2$ ) is locked to the  $F = 2$  to  $F' = 3$  transition, and the repumper beam ( $I = 0.2\text{ mW/cm}^2$ ) is locked to the  $F = 1$  to  $F' = 2$  transition (see Chap. 2). Both beams are sent through the same fiber. The polarization of the single cooling beam is circular, but the polarization of the first-order diffraction changes. The first-order diffraction efficiency for the MOT beam is 30(5) %, leading to balanced optical molasses [156]. A GMOT requires a large and high quality beam. We expand the beam directly out of a single-mode optical fiber to a diameter to 3.6 cm, and this beam is collimated with a shearing interferometer. We then finely align the beam with a tiltable mount and 3D translation stage to optimize the GMOT.

### 6.1.2 Temperature measurement

Measuring the mean square radius of the two dimensional cloud image versus expansion time allows us to extract the atomic temperature ( $T = m_{Rb}\sigma_v^2/k_B$ ) from fits of

$\sigma^2 = \sigma_0^2 + \sigma_v^2 t^2$ . Fig. 6.3 displays the results of this measurement for different experimental conditions. Fig. 6.3 (a, left) presents atomic cloud temperatures as measured after cooling for 50 ms in a single-stage, far-detuned GMOT (see Table 6.1). The lowest observed temperature for this procedure is  $9.7(0.3)\mu\text{K}$  and occurs at a detuning of  $8.2\Gamma$  (an example of the fit for this detuning is given in Fig. 6.3 (a, right)).

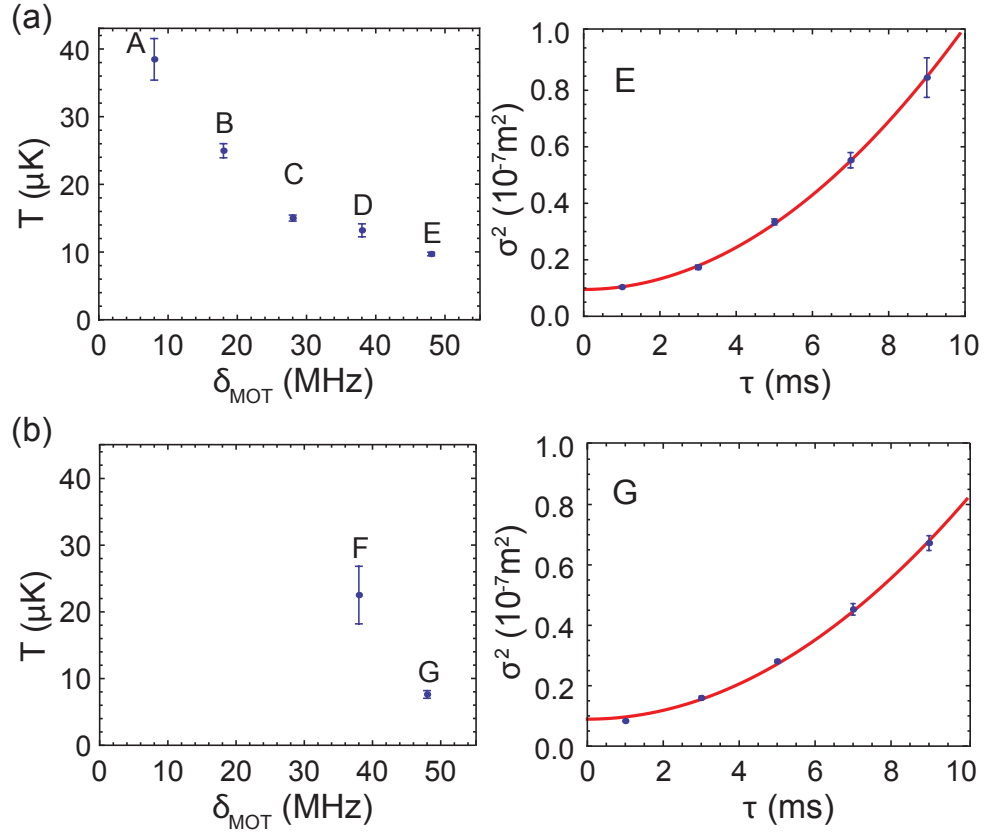


Figure 6.3: (a) Temperature versus the detuning of the cooling beam for a single-stage, far-detuned GMOT (see Table 6.1);  $\sqrt{2}\sigma$  is the  $1/e$  radius of atomic cloud, and we fit 1 – 9 ms time-of-flight data to  $\sigma^2 = \sigma_0^2 + \sigma_v^2 t^2$  (right). We estimate the atomic temperature  $T$  ( $= m_{Rb}\sigma_v^2/k_B$ ) from the fits (left). (b) Temperature versus the detuning of the cooling beam for a multi-stage, far-detuned GMOT with no molasses stage (F) and with a molasses stage (G) (see Table 6.2). (figure from Ref. [77])

Employing a molasses cooling stage after a multi-stage, far-detuned GMOT requires the adjustment of the GMOT position as the magnetic field gradient decreases to zero (Fig. 6.3 (b) and Table 6.2). We optimize our bias magnetic field for each far-detuned GMOT

Cooling time $\tau$ (ms)	$\delta_{MOT}/\Gamma$	$dB/dz$ (G · cm $^{-1}$ )	$I/I_{sat}$
$\tau_{MOT}$	1.5	10.8	1.55
50	1.5 to 8.2	10.8	1.16

Table 6.1: Single-stage, 50 ms far-detuned MOT parameters when scanning the detuning of a single MOT beam (time flows downwards in the table). This table corresponds to Fig. 6.3 (a); in this paper, the cooling process with several stages is represented by the cooling stage time ( $\tau$ ), the detuning of the cooling beam ( $\delta_{MOT}$ , red-detuned from the cooling transition), magnetic field gradient ( $dB/dz$ ), and the relative intensity of the single incident cooling beam ( $I/I_{sat} = 2\Omega^2/\Gamma^2$ ). (figure from Ref. [77])

stage such that the laser-cooled atoms remain in the capture volume for up to 10 ms after turning off the magnetic field. Table 6.2 summarizes the steps in this process. In the multi-stage, far-detuned GMOT procedure without molasses, we measure an atomic temperature of  $22.5(4)$   $\mu$ K (Fig. 6.3 (b, left), F). This temperature can be explained by the final detuning of  $6.5\Gamma$  being closer to the resonance than that of the single-stage, far-detuned MOT. The atomic temperature after the multi-stage, far-detuned GMOT and a 1 ms molasses stage (at a detuning of  $8.2\Gamma$ ) is  $7.6(0.6)$   $\mu$ K (Fig. 6.3 (b, left), G), which is colder than the single-stage, far-detuned GMOT without molasses described above.

Cooling time $\tau$ (ms)	$\delta_{MOT}/\Gamma$	$dB/dz$ (G · cm $^{-1}$ )	$I/I_{sat}$
$\tau_{MOT}$	1.5	10.8	1.61
30	3.2	10.8	1.40
15	4.9	6.6	1.20
15	6.5	4.5	1.20
1	8.2	0	1.20

Table 6.2: Multi-stage, 60 ms far-detuned MOT and 1 ms optical molasses parameters, with time flowing downwards in the table. This table corresponds to Fig. 6.3 (b) G; the same multi-stage far-detuned MOT without 1 ms optical molasses corresponds to Fig. 6.3 (b) F. (figure from Ref. [77])

### 6.1.3 Theory: sub-Doppler cooling

Ref. [155] describes the requirements for magneto-optical trapping in a GMOT. They consist of finding a configuration where the optical forces sum to zero. We are interested in understanding sub-Doppler cooling in the polarization configuration present in the GMOT, as it is neither Sisyphus ( $\text{lin} \perp \text{lin}$ ) polarization gradient cooling, nor  $\sigma^+ - \sigma^-$  orientational cooling. To simplify the theory, we will assume the cold atoms are close enough to the center of the quadrupole field so that we can neglect any Zeeman contribution to the laser detuning. We will consider only 1D laser cooling.

There is a stable polarization configuration (relative phases between beams displace the polarization configuration but do not change its morphology) in a four-beam configuration such as the GMOT. The spatial periodicity of the underlying lattice is determined by the geometry of four beams, with a primitive unit cell ( $\mathbf{k}_i - \mathbf{k}_j$ ) of the reciprocal lattice [158], where  $\mathbf{k}_i$  is the wavevector of the 3D beams (see Fig. 6.4).

The polarization pattern of the GMOT configuration is complicated because of the existence of both linear and circularly polarized light. For a chosen quantization axis along the vertical axis (**z**), when the  $\sigma$ -polarized vertical beam reflects off the diffraction gratings, the handedness of the polarization (seen from the opposite direction of propagating beams with **k**-vectors) is maintained (at the  $\approx 90\%$  level), but in terms of the quantization axis, the reflected beams will have  $\sigma^+$ ,  $\sigma^-$ , and  $\pi$  components. The exact composition can be calculated by a suitable transformation matrix that connects the axes through a rotation. In Fig 6.4 (a-b), a crystal axis parallel to the vertical GMOT beam with its wavevector  $\mathbf{k}_1$  has an angle of  $109.5^\circ$  from three other GMOT beams with their wavevectors of  $\mathbf{k}_2$ ,  $\mathbf{k}_3$ , and  $\mathbf{k}_4$ . For the quantization axis  $\mathbf{q}_z=(0,0,1)$ , the polarization states of the vertical

GMOT beam and the three GMOT beams projected along the vertical axis correspond to 100 %, 0 %, and 0 %; 44.4 %, 11.1 %, and 44.4 % of  $\sigma^+$ ,  $\sigma^-$ , and  $\pi$  respectively. In the horizontal (**xy**) plane, the line at  $60^\circ$  and its perpendicular at  $150^\circ$  from the **y**-axis define crystal axes in the system (Fig 6.4 (c)). For the quantization axis  $\mathbf{q}_{xy} = (\sqrt{3}/2, 1/2, 0)$ , the polarization states of the three beams projected to the horizontal plane with  $\mathbf{k}_2$ ,  $\mathbf{k}_3$ , and  $\mathbf{k}_4$  correspond to 82.5 %, 0.8 %, and 16.7 %; 25 %, 25 %, and 50 %; 0.8 %, 82.5 %, and 16.7 % of  $\sigma^+$ ,  $\sigma^-$ , and  $\pi$  respectively. A simple retroreflection of a circularly polarized beam would result in a standing wave without any polarization gradients and no sub-Doppler cooling. Additional polarization components due to the reflection angles are critical for a sub-Doppler cooling mechanism.

We numerically calculate the force on the atoms versus atom velocity along the **z**-axis of the **xz** plane (Fig. 6.4 (b)) and the diagonal axes of the **xy** plane (Fig. 6.4 (c)). In the simulation, we include the multi-level structure of a  $^{87}\text{Rb}$  atom, such as the transitions from the  $F = 2$  Zeeman sub-states to the  $F' = 3$  Zeeman sub-states. The steady state solution of the master equation,  $\frac{d\hat{\rho}}{dt} = -\frac{i}{\hbar}[\hat{H}, \hat{\rho}] + \Gamma_{\hat{\rho}}$ , is solved by the matrix continued fraction method [159]. Treating the beams as classical optical fields, the raising ( $\hat{A}_+^\dagger$ ,  $\hat{A}_-^\dagger$ ,  $\hat{A}_0^\dagger$ ) and the lowering ( $\hat{A}_+$ ,  $\hat{A}_-$ ,  $\hat{A}_0$ ) operators correspond to the optical pumping and spontaneous emission of the transitions of  $\sigma^{+-}$ ,  $\sigma^{-+}$ , and  $\pi$ -polarized lights, respectively, and the Clebsch-Gordon coefficients for those operators define the transition strength between each hyperfine ground and excited state. The atom-light interaction Hamiltonian is  $\hat{H}_{int} = -\frac{1}{2}(\Omega_+(\mathbf{r})\hat{A}_+ + \Omega_-(\mathbf{r})\hat{A}_- + \Omega_0(\mathbf{r})\hat{A}_0) + h.c.$ , where  $\Omega_+$ ,  $\Omega_-$ , and  $\Omega_0$  are Rabi frequencies for  $\sigma^{+-}$ ,  $\sigma^{-+}$ , and  $\pi$ -polarized lights, respectively. The force operator is  $\hat{F} = -\nabla(\hat{H}_{int})$ . After using the master equation to calculate the expectation value of  $\hat{F}$  as a function of atomic velocity, we observe a sub-Doppler cooling signature (a steep

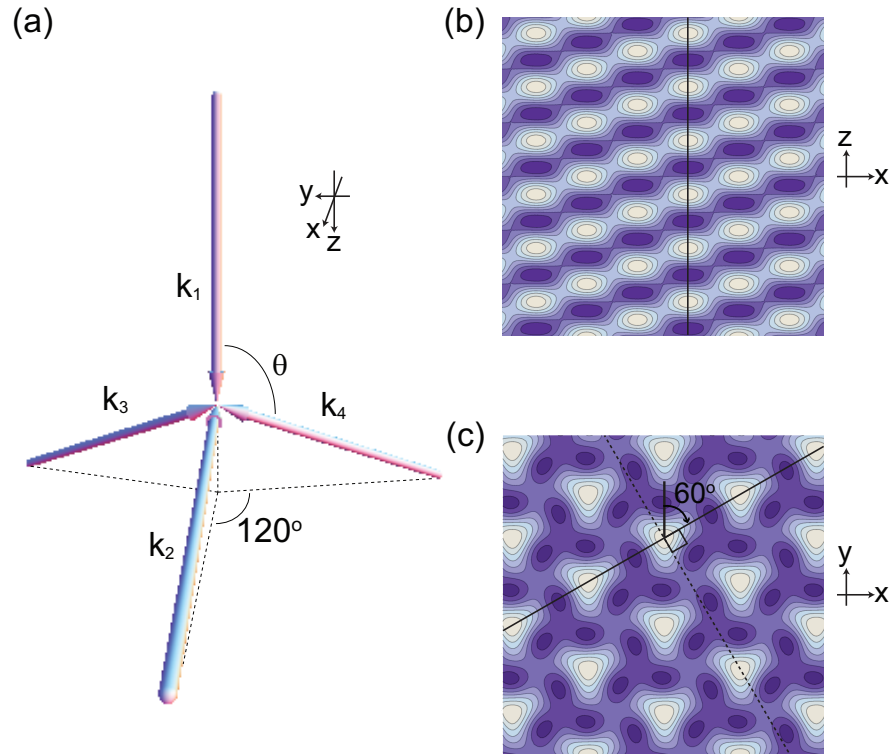


Figure 6.4: (a) Tetrahedral MOT configuration;  $|\cos \theta| = 1/3$  and  $\sum_{i=1}^4 \mathbf{k}_i I_i = 0$ . (b) Optical lattices in the  $\mathbf{xz}$  plane (solid line: 1D optical lattice along the  $\mathbf{z}$ -axis of the  $\mathbf{xz}$  plane). (c) Optical lattices in the  $\mathbf{xy}$  plane (solid line: 1D optical lattice along the diagonal axis with an angle of  $60^\circ$  relative to the  $\mathbf{y}$ -axis, dashed line: 1D optical lattice along the diagonal axis with an angle of  $150^\circ$  relative to the  $\mathbf{y}$ -axis). (figure from Ref. [77])

slope of force vs. velocity) at low atom velocities for both crystal axes (Fig. 6.5 (a) and (b)).

We calculate the force for different combinations of polarization in order to understand its role. If we have imbalanced  $\sigma$ -polarizations with no  $\pi$ -component, the narrow feature is present, but the point of zero force may not be contained within the feature, preventing sub-Doppler temperatures. This can be understood in the following way: there is orientational cooling for the part of the  $\sigma^+$  component that balances the  $\sigma^-$  component present, and then the force versus velocity curve is displaced vertically by the remaining unbalanced  $\sigma^+$  component. When there is  $\pi$  polarization present, we recover a force versus velocity curve that should produce good sub-Doppler cooling with a narrow velocity feature centered on the zero-force point. This arises from coherent, two-photon, velocity-selective resonances between ground-state sublevels, coherent two-photon Raman transitions of  $\sigma^+ - \pi$  and  $\pi - \sigma^-$  that become resonant when the energy difference between two sublevels is equal to the sum of opposite Doppler shifts of the two laser beams. The simulations show that the narrow velocity feature shifts horizontally away from zero velocity when a longitudinal magnetic field is present, similar to traditional  $\sigma^+ - \sigma^-$  orientational cooling [160]. The horizontal shift of the force versus velocity curve is also accompanied by a vertical displacement as the magnetic field increases and negates the sub-Doppler cooling at higher magnetic fields.

Figure 6.5 shows results of our model for different axes and polarization configurations present in the GMOT. The left column of the figure shows the broad features, while the right is a zoom on the region around zero. The atomic temperature  $T$  ( $= D_p/k_B\alpha$ ) is determined by the momentum diffusion coefficient  $D_p$ , related to heating and the momentum friction coefficient  $\alpha$ , related to cooling. If the spacing of the 1D optical lattice

becomes more dense for a constant  $D_p$ ,  $\alpha$  increases because of the more frequent cooling events (note that our simulation does not calculate  $D_p$ , so we are unable to calculate actual temperatures). Assuming an isotropic diffusion constant, we expect the atomic temperature in the vertical direction,  $T_z$ , to be colder than the temperature in the horizontal direction,  $T_{xy}$ , based on the steeper slope of the force curve near zero velocity (see Figs. 6.5 (a-b), where  $I/I_{sat}=1.2$  and  $\delta=-1.5\Gamma$ ).

In the experimental run with a multi-stage, far-detuned GMOT and a 1ms optical molasses (Fig. 6.3 (b) G),  $T_z$  is 1.5(0.25) times lower than  $T_{xy}$ ; a recent GMOT experiment observes similar anisotropic sub-Doppler cooling [157]. Given our 1D simplification, this can be considered a qualitative agreement. As a reference to compare the force vs. velocity features, we simulated the sub-Doppler cooling process of  $\sigma^+-\sigma^-$  orientational cooling and  $\text{lin}\perp\text{lin}$  polarization gradient cooling (Fig. 6.5 (c-d)). The slopes of vertical direction GMOT and  $\sigma^+-\sigma^-$  cooling are similar (Fig. 6.5 (a) and (c)). In addition, the amplitude of the Doppler cooling feature to capture atoms along the horizontal direction is lower than in the vertical direction because the intensities of the three GMOT beams along the horizontal axis are reduced compared to those along the vertical axis. Experimentally, we also observe an atom cloud squeezed along the vertical direction (Fig. 6.2 (c)). If we assume comparable diffusion constants between the GMOT and traditional sub-Doppler mechanisms, our expectations and observations are similar.

#### 6.1.4 Atom number and density

The success of loading cold atoms into the small (order  $\lambda$ ) wells around the nanofiber requires many cold atoms at high density. We next study atom number ( $N_{atom}$ ) and atomic peak density ( $n_{atom}$ ) as a function of magnetic field gradient (Fig. 6.6) after cooling the

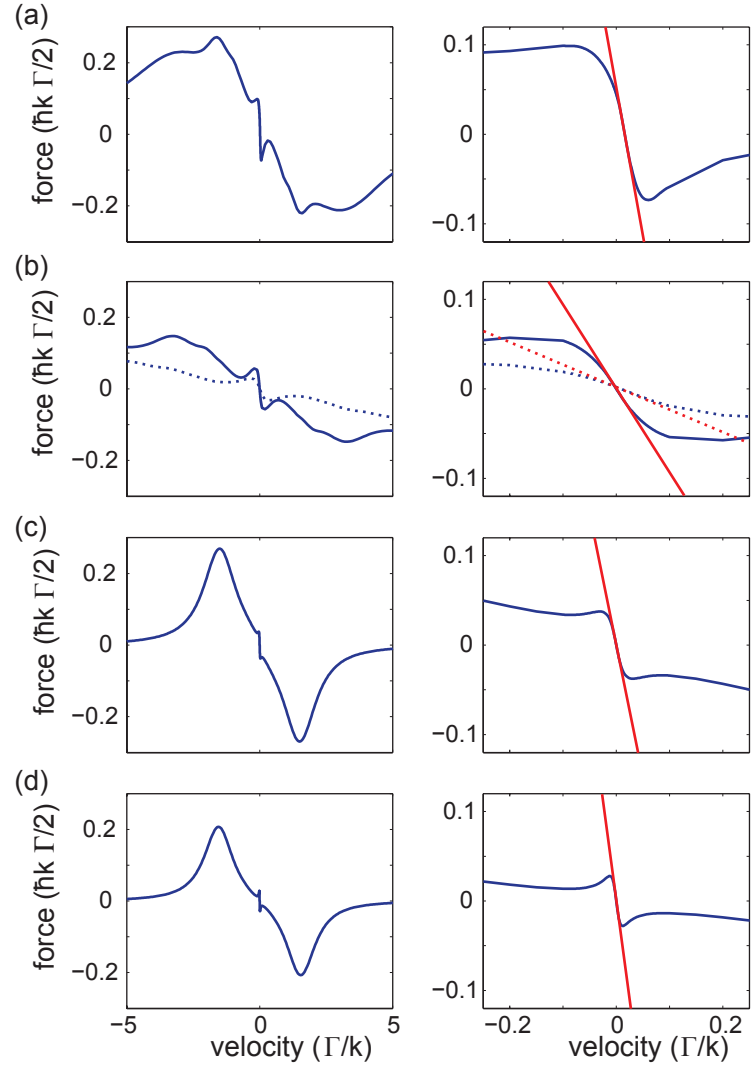


Figure 6.5: Calculated force on atoms as a function of atom velocity for different axes and polarization configurations of the GMOT. (a) Vertical axis of the GMOT, the **z**-axis of the **xz** plane (Fig. 6.4 (b)). (b) Horizontal axes of the GMOT, the diagonal axes of the **xy** plane. solid line: the axis at an angle of  $60^\circ$  relative to the **y**-axis, dashed line: the axis at an angle of  $150^\circ$  relative to the **y**-axis (see Fig. 6.4 (c)). (c)  $\sigma^+$ - $\sigma^-$  orientational cooling. (d) lin- $\perp$ -lin Sisyphus cooling where  $I/I_{sat}=1.2$  and  $\delta=-1.5\Gamma$ . The right column shows a zoom of the region where the slope is largest around zero velocity. (figure from Ref. [77])

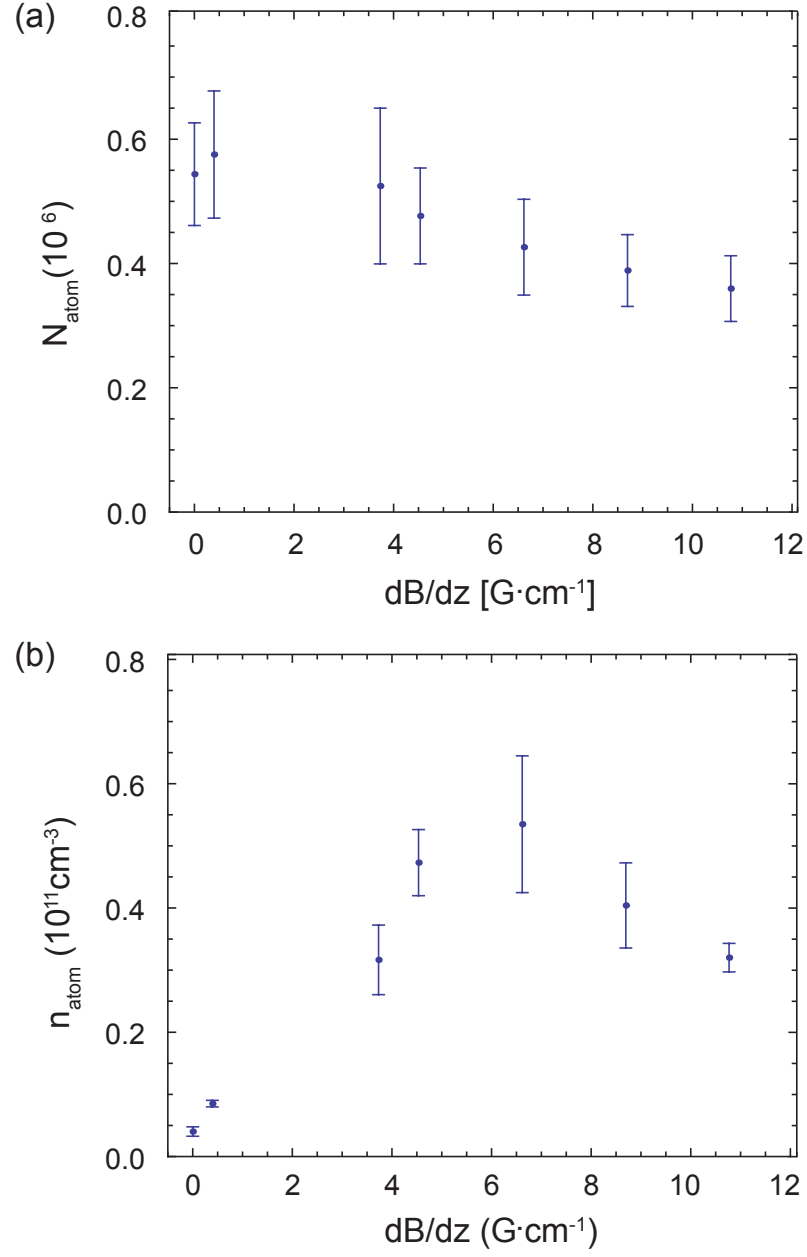


Figure 6.6: Atom number ( $N_{atom}$ ) and atomic peak density ( $n_{atom}$ ) as a function of the magnetic field gradient ( $dB/dz$ ). Each data point has the same initial MOT atom number extracted simultaneously from a series of trials, and we vary  $dB/dz$  during the far-detuned MOT process. (figure from Ref. [77])

atoms for 50 ms in a far-detuned GMOT. The experimental parameters are: ( $\tau$  (ms),  $\delta_{MOT}/\Gamma$ ,  $dB/dz$  ( $\text{G} \cdot \text{cm}^{-1}$ ),  $I/I_{sat}$ ) = ( $\tau_{MOT}$ , 1.5, 10.8, 1.29)  $\rightarrow$  (50, 3.9, 0.4 to 10.8, 0.96). Then, as  $dB/dz$  increases,  $N_{atom}$  decreases, as seen in Refs. [161, 162]. In addi-

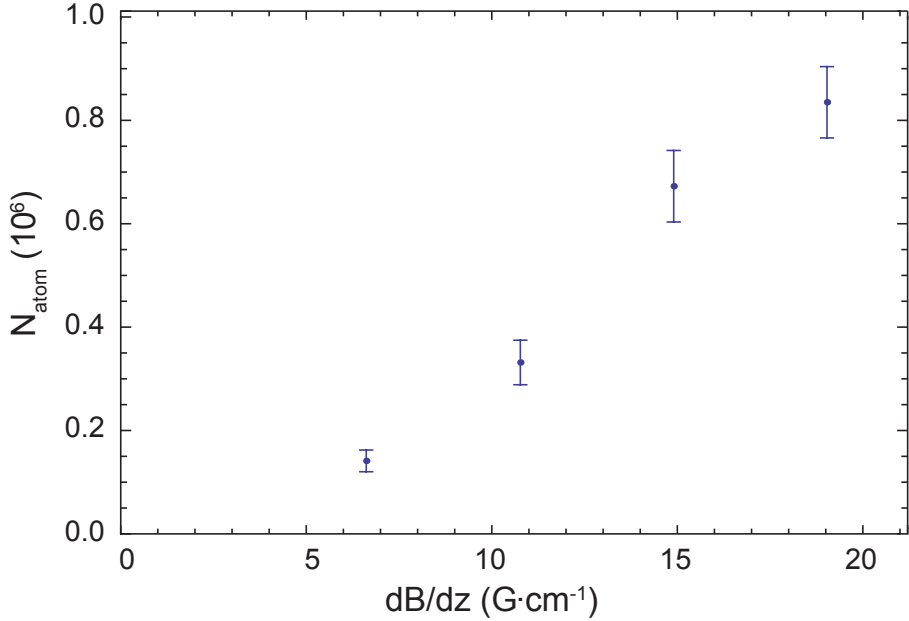


Figure 6.7: Atom number in a GMOT (without sub-Doppler cooling) as a function of the magnetic field gradient. (figure from Ref. [77])

tion,  $n_{atom}$  also increases linearly as a function of  $dB/dz$ , but at a certain peak density, the linear scaling does not work anymore because the light pressure from reradiated photons limits the atomic density [161–163]. Reabsorption of scattered photons within the trapped cloud becomes important above  $10^{11} \text{ atoms} \cdot \text{cm}^{-3}$ . In this regime,  $n_{atom}$ , which is nearly independent of  $N_{atom}$ , cannot be simply modeled due to the effective repulsive force between atoms. The atomic density decreases above the peak density because the multiple scattering of photons prevents further compression of the atomic cloud. Multiple scattering results in the heating of atoms because of increased momentum diffusion and reduced friction even with the restoring and friction forces of sub-Doppler cooling [161].

A GMOT with no sub-Doppler cooling captures more atoms from the background atomic vapor as we increase the magnetic field gradient (see Fig. 6.7). The capture velocity of the GMOT increases when the magnetic fields in the GMOT shift the energy levels of atoms entering the trap from all directions. This is a mechanism similar to that

of a Zeeman slower, which has a spatially-varying magnetic field to tune the atoms back into resonance as they decelerate and their Doppler shift changes. The parameters of the experiments are:  $(\tau \text{ (ms)}, \delta_{MOT}/\Gamma, dB/dz \text{ (G} \cdot \text{cm}^{-1}), I/I_{sat}) = (\tau_{MOT}, 1.5, 6.6 \text{ to } 19, 1.35)$ . The total number of atoms is smaller by two orders of magnitude than in typical MOTs.

## 6.2 Conclusions

The GMOT presents a viable option for laser cooling atoms in a dilution refrigerator due to its simplified optics and compact size. We have reached sub-Doppler temperatures with this system, a criterion that is crucial for the efficient loading of a nanofiber trap. Future work will focus on making a robust structure for use in a cryogenic environment, as well as loading a nanofiber trap from a GMOT. Recent results in Ref. [157] also suggest that atom number can be improved to  $\sim 10^7$  atoms by using nanofabricated gratings optimized for this trap geometry. We present an overview of the other components of the hybrid system in progress in the next chapter.

## Chapter 7: Conclusions and outlook

This thesis presents work with optical nanofibers, focusing on trapping  $^{87}\text{Rb}$  atoms in their evanescent field and using photon-counting techniques to measure atom dynamics and excited-state lifetimes near them. It also outlines an ongoing effort to create a hybrid system consisting of an ensemble of  $^{87}\text{Rb}$  atoms coupled to a superconducting circuit. As part of that effort, the optical nanofiber is a potentially cryogenically-compatible atom trap, and we have demonstrated the functionality of a compact MOT to load atoms onto the nanofiber within the spatially- and optically-constrained environment of a dilution refrigerator.

Much work remains to piece together this hybrid system, but luckily there is an array of exciting physics to explore with nanofibers on their own. In this chapter we outline three ongoing and one future project out of the many possible ones, both known and not yet conceived.

### 7.1 Faraday spectroscopy with nanofibers

The Faraday effect [95], which we use to lock our repump laser (see Chap. 2), also has applications in spectroscopy of magnetic fields. It has been used in both high-precision atomic magnetometry [164], as well as spatial resolution of magnetic field profiles [165,166]. Nanofibers could aid this effort given their ability to be brought close to surfaces and their

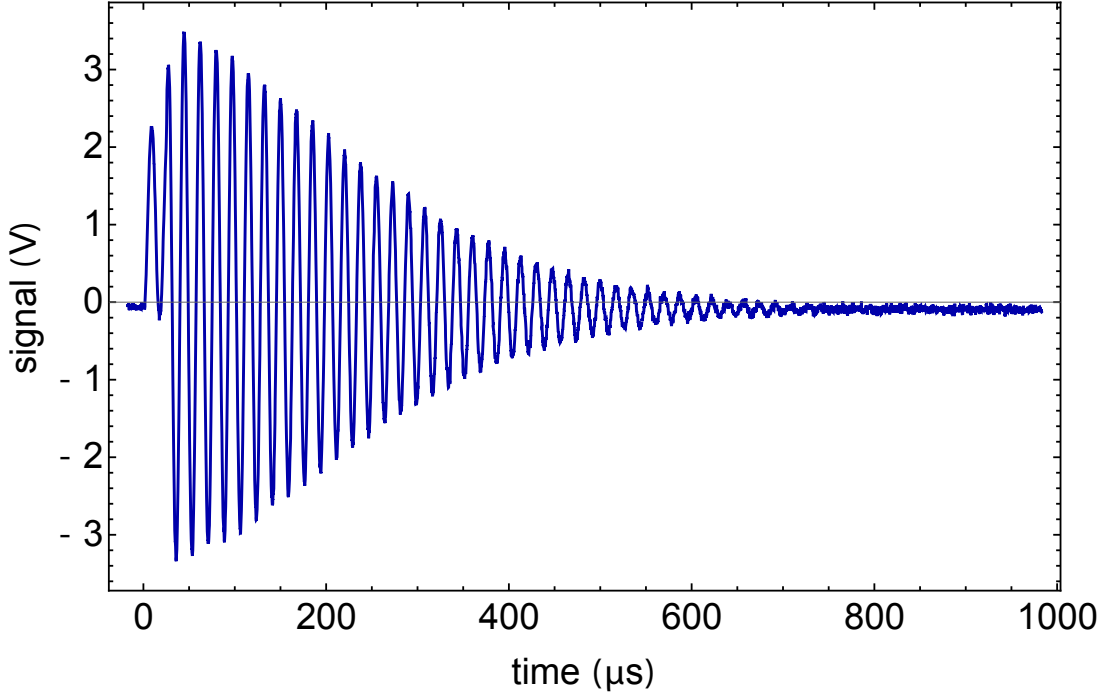


Figure 7.1: Faraday rotation signal of  $^{87}\text{Rb}$  atoms measured on a balanced photodetector. The atoms are optically pumped into the  $|F, m_F\rangle = |2, 2\rangle$  state. The observed frequency of  $58 \pm 2$  kHz corresponds to a field of 85 mG.

large optical depth with only a small number of atoms.

An ongoing collaboration with Fredrik Fatemi of NRL seeks to perform Faraday spectroscopy with nanofiber-trapped atoms. Fig. 7.1 displays a free-space Faraday rotation signal in our setup, with a frequency of  $58 \pm 2$  kHz, corresponding to a field of about 83 mG. We have observed free-space Faraday signals as small as 20 kHz. We are currently working to observe the same signal using atoms trapped around the nanofiber. It is likely that this measurement will also shed light on the longitudinal light polarization present in the nanofiber mode, which creates so-called fictitious magnetic fields [167].

## 7.2 Surface physics

The background vapor generated by our atomic dispensers coats the nanofiber with rubidium. Measuring in real time the transmission of a weak resonant probe reveals interesting dynamics of how atoms adsorb and desorb from the silica surface.

We find that, after a few seconds in a background rubidium pressure of  $\sim 10^{-9}$  mbar, the coating on the nanofiber can extinguish a resonant probe of a few microwatts to the level of the dark counts ( $10^2$  counts  $\cdot$  s $^{-1}$ ) in our SPCM. This represents an extinction of 100 dB, and we posit it is due either to direct absorption by the atomic layer or to the changing of the boundary condition of the waveguide to a metal such that the evanescent wave cannot propagate.

Sending higher powers of 1064-nm (or 750-nm) light through the nanofiber heats the waist such that atoms will desorb from its surface. Fig. 7.2 shows two time traces of count rates of the weak probe after turning on the 1064-nm beam, using powers of 0.48 mW (dark red) and 0.12 mW (blue). There is a clear dependence of the heating time before the onset of desorption occurs,  $t_d$ , on the power of the light propagating through the fiber. We approximately extract those times and plot them in Fig. 7.3. This large change in the desorption time for weak transmitted powers might allow us to quantitatively add to the discussion of thermalization processes of nanofibers in Ref. [168], but in a different parameter regime where the temperature changes are much smaller. A separate experiment involving heterodyne detection, where the local oscillator propagates in free-space and the signal through the nanofiber. This method is able to sensitively detect temperature changes in the fiber by measuring the Doppler shift of the light induced by the varying index of refraction as the nanofiber heats or cools. We can observe temperature

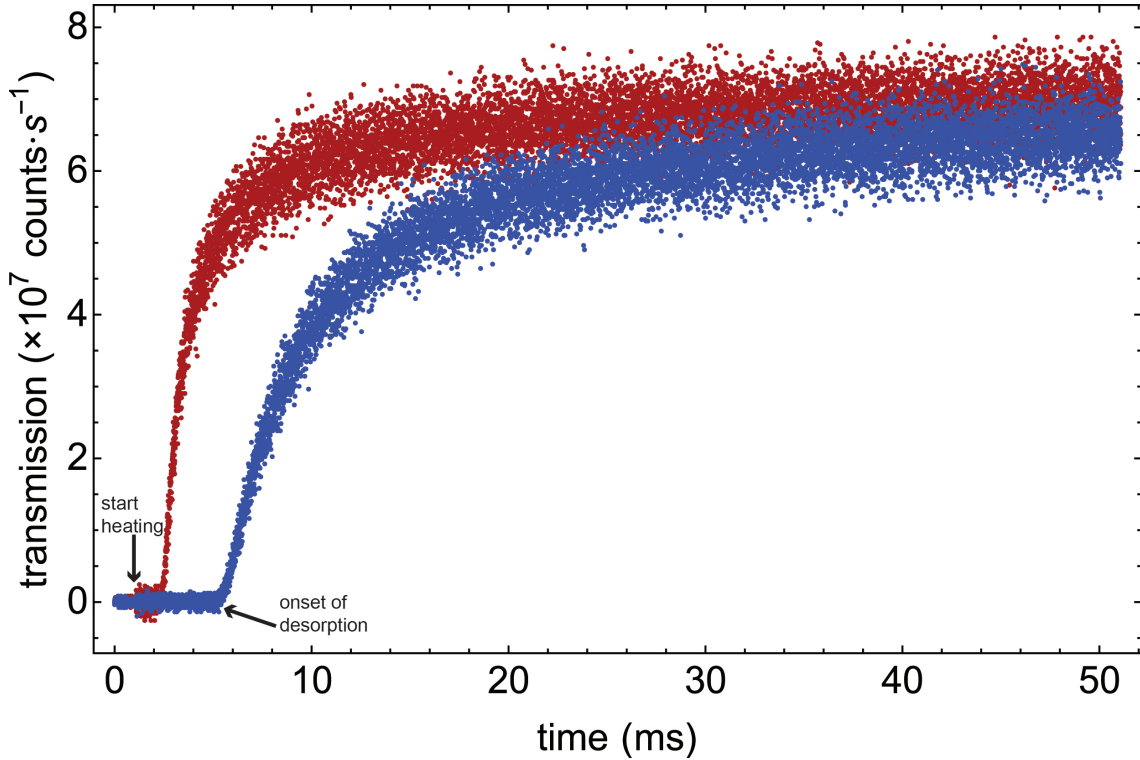


Figure 7.2: Transmission of a weak resonant probe through nanofiber as a function of time after applying 1064-nm light to desorb atoms from the surface. The two datasets correspond to 1064-nm powers of 0.48 mW (dark red) and 0.12 mw (blue).

differences when only microwatts of light are sent through the nanofiber, present another parameter regime to study.

Another experiment in the planning stage seeks to take advantage of the high extinction ratio of weak probe beams in order to create a new kind of optical switch. Placing the nanofiber in a heated vapor cell can decrease the coating times to nanoseconds [96], and we see in Fig. 7.3 that desorption times of microseconds are achievable with modest powers of heating laser.

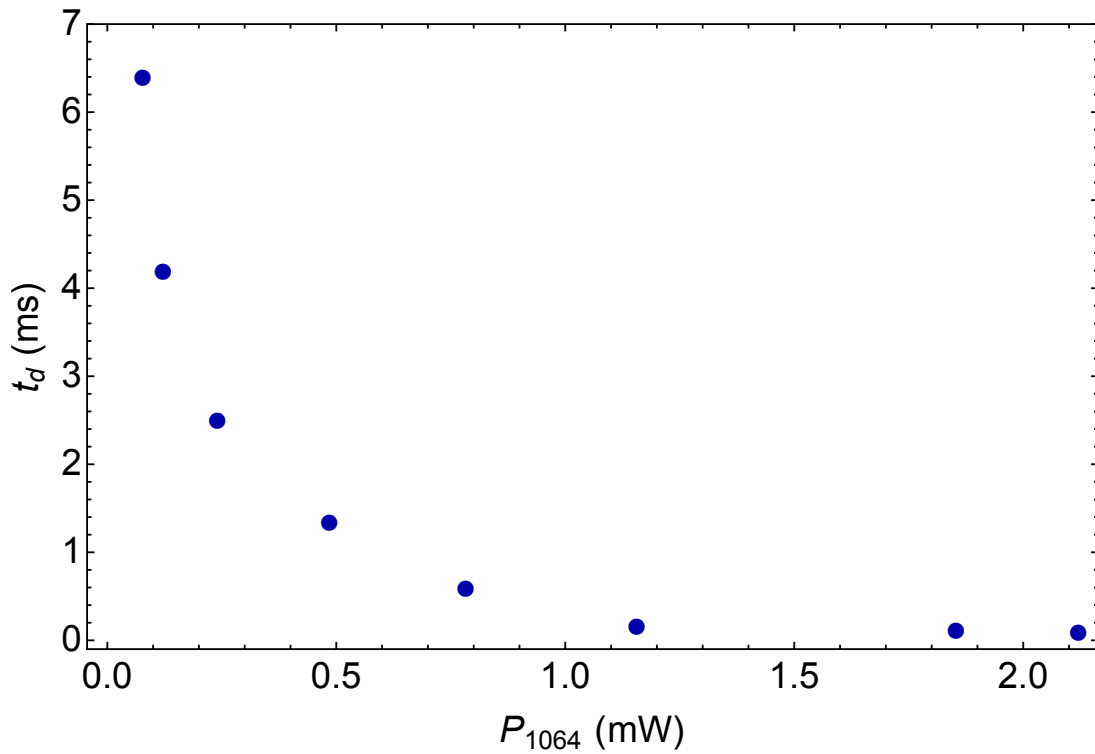


Figure 7.3: Extracted heating time before onset of desorption occurs, as a function of 1064-nm power.

## 7.3 Hybrid system

These next sections sketch two projects within the group aimed at completing the overall hybrid system. The first is a source of  $^{87}\text{Rb}$  atoms from which to load the GMOT described in Chap. 6. It will consist of an atomic beam originating from an unbalanced 2D MOT [169] in a room-temperature UHV chamber. The second is a method to accurately position the fiber relative to the superconducting chip by studying how Rayleigh scattering from the fiber affects the resonance frequency and phase of the *LC* resonator [75].

### 7.3.1 Atomic source: 2D MOT

This project needs a 2D MOT to provide atoms for the cryogenic MOT setup. In this configuration, four laser beams cool atoms only in the transverse directions so that an atomic beam with small divergence emerges along the un-cooled axis [169]. High atomic flux rates of  $\sim 10^9 \text{ atoms}\cdot\text{s}^{-1}$  have been reported experimentally, allowing for the formation of large 3D MOTs with up to  $10^{10}$  atoms tens of centimeters downstream [169–171]. This makes the 2D MOT a simple alternative to the Zeeman slower, as it is more compact and permanent magnets can be used to generate the quadrupole field [171].

### 7.3.2 Interfacing fibers with superconducting circuits

We must place the atoms with a few micrometers of the superconducting chip in order to achieve the strongest magnetic dipole coupling [61, 64]. This requires precise alignment of the optical nanofiber relative to the chip without the aid of optical access. To this end, we have developed a technique to use the effect of scattered light on the resonator to determine the position of the fiber, with details of the setup in Ref. [75].

## 7.4 Self-organization

The strong atom-waveguide coupling in optical nanofibers opens the door to the collective physics of self-organization already observed in traditional cavity-QED experiments [172, 173]. Driving the atoms with a near-resonant laser from the side causes a non-negligible fraction of spontaneous emission to couple back into the guided mode, as we saw in Chap. 5. If the atoms are also trapped along the nanofiber, then this spontaneous emission into the guided mode mediates a long-range interaction between the atoms [99]. Furthermore, if one removes the axial confinement so that atoms can freely move along the fiber axis, then this interaction creates a potential [100, 101],

$$U_{dd} \approx \frac{\gamma_{1D} s_0}{2} \sum_{j,j'} \sin(k_0|z_j - z_{j'}|) , \quad (7.1)$$

where  $s_0$  is the magnitude of the atomic coherences,  $j$  and  $j'$  are the atomic indices,  $k_0 = 2\pi/\lambda_0$  is the free-space wavenumber of the light emitted by the atoms, and  $z_j$  is the position of atom  $j$ . A self-ordered arrangement of  $N$  atoms into a lattice with spacing  $\lambda_0 (1 - 1/2N)$  minimizes this potential [100], as schematically depicted in Fig. 7.4. Observing this collective behavior either in the reflection spectrum or in the correlations of the light emitted by the atoms would be an interesting application of this system and remains a priority of future experiments. An ongoing collaboration with JQI Fellow Alexey Gorshkov and his student also explores interesting ways to engineer center-of-mass cooling by introducing bandgaps and how [33, 174, 175] the chirality of the system could lead to different self-organized arrangements.

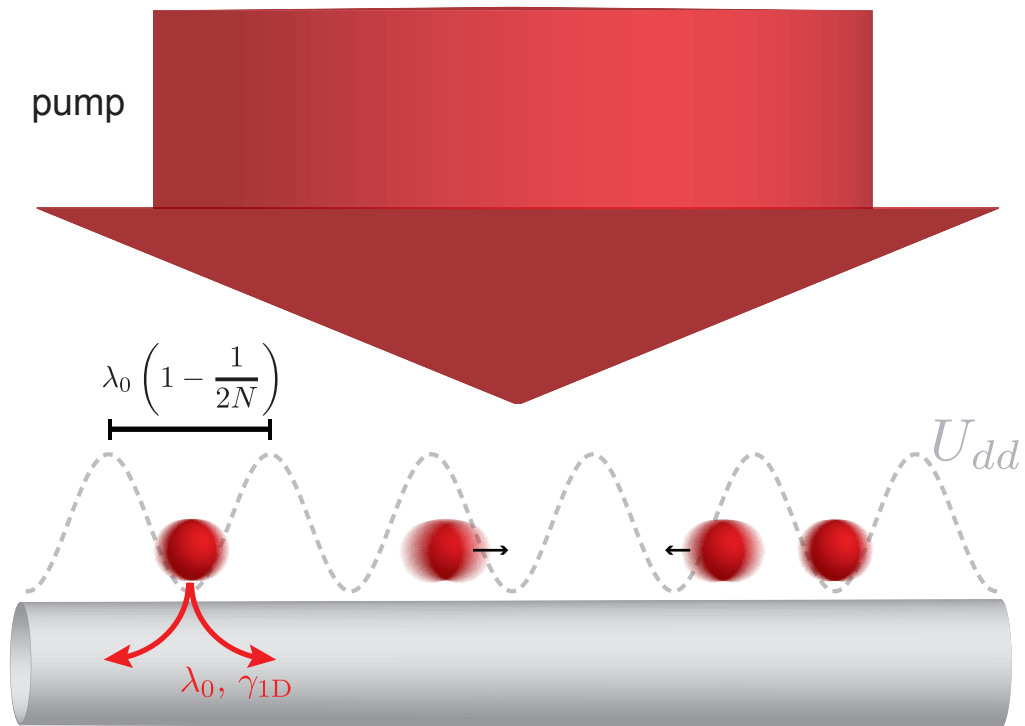


Figure 7.4: Schematic illustration of self-organization of atoms trapped around an optical nanofiber. An external pump beam drives spontaneous emission in atoms trapped around the nanofiber but without axial confinement. The resulting long-range interaction results in a dipole-dipole potential  $U_{dd}$  with lattice spacing  $\lambda_0(1 - 1/2N)$ , where  $N$  is the number of atoms.

## 7.5 Conclusions

Fibers are a potential platform for many interesting quantum optics and quantum many-body studies now that we are gaining control over modes, transmission [74, 88], detection, and atom-trapping [21–24]. Recent experiments in other groups have used nanofibers, for example, to store optical pulses in an atomic ensemble with EIT [37, 38], to couple the spin and orbital angular momentum of light [33, 34], and to create nonlinear optical elements with single atoms [35, 176]. These developments point to a rich future of utilizing nanofibers to explore physics within quantum information science and the engineering of novel interactions.

## Appendix A: Nanofiber modes

For a cylindrical, step-index waveguide with radius  $a$ , and with index  $n_1$  for  $r < a$  and  $n_2$  for  $r > a$ , the equations for the fundamental mode structure are in many references. [177–180]. Here I present, for the ease of the reader, the derivation from the thesis of J. E. Hoffmann [78]. We will apply them to the case of a fused silica ( $n_1 = 1.45367$ ) nanofiber ( $a = 250$  nm) in air ( $n_2 = 1$ ).

### A.1 Field equations

This section lists the electric and magnetic fields in cylindrical coordinates for the geometry stated above. For  $r < a$ :

$$E_{r,\pm} = \frac{-i\beta}{h^2} \left[ \pm \frac{i\mu_0\omega l}{\beta r} BJ_l(hr) + AhJ'_l(hr) \right] e^{i(\omega t - \beta z \pm l\varphi)} \quad (\text{A.1})$$

$$E_{\phi,\pm} = \frac{-i\beta}{h^2} \left[ \pm \frac{il}{r} AJ_l(hr) - \frac{\mu_0\omega h}{\beta} BJ'_l(hr) \right] e^{i(\omega t - \beta z \pm l\varphi)} \quad (\text{A.2})$$

$$E_{z,\pm} = AJ_l(hr) e^{i(\omega t - \beta z \pm l\varphi)} \quad (\text{A.3})$$

$$H_{r,\pm} = \frac{-i\beta}{h^2} \left[ \mp \frac{i\varepsilon_1\omega l}{\beta r} AJ_l(hr) + BhJ'_l(hr) \right] e^{i(\omega t - \beta z \pm l\varphi)} \quad (\text{A.4})$$

$$H_{\phi,\pm} = \frac{-i\beta}{h^2} \left[ \frac{\varepsilon_1\omega}{\beta} AhJ'_l(hr) \pm \frac{il}{r} BJ_l(hr) \right] e^{i(\omega t - \beta z \pm l\varphi)} \quad (\text{A.5})$$

$$H_{z,\pm} = BJ_l(hr) e^{i(\omega t - \beta z \pm l\varphi)}, \quad (\text{A.6})$$

and  $r < a$ ,

$$E_{r,\pm} = \frac{i\beta}{q^2} \left[ \pm \frac{i\mu_0\omega l}{\beta r} DK_l(qr) + ChK'_l(qr) \right] e^{i(\omega t - \beta z \pm l\varphi)} \quad (\text{A.7})$$

$$E_{\phi,\pm} = \frac{i\beta}{q^2} \left[ \pm \frac{il}{r} CK_l(qr) - \frac{\mu_0\omega h}{\beta} DK'_l(qr) \right] e^{i(\omega t - \beta z \pm l\varphi)} \quad (\text{A.8})$$

$$E_{z,\pm} = CK_l(qr) e^{i(\omega t - \beta z \pm l\varphi)} \quad (\text{A.9})$$

$$H_{r,\pm} = \frac{i\beta}{q^2} \left[ \mp \frac{i\varepsilon_2\omega l}{\beta r} CK_l(qr) + DqK'_l(qr) \right] e^{i(\omega t - \beta z \pm l\varphi)} \quad (\text{A.10})$$

$$H_{\phi,\pm} = \frac{i\beta}{q^2} \left[ \frac{\varepsilon_2\omega}{\beta} CqJ'_l(qr) \pm \frac{il}{r} DK_l(qr) \right] e^{i(\omega t - \beta z \pm l\varphi)} \quad (\text{A.11})$$

$$H_{z,\pm} = DK_l(qr) e^{i(\omega t - \beta z \pm l\varphi)}, \quad (\text{A.12})$$

where  $\beta$  is the mode propagation constant,  $h = \sqrt{k^2 - \beta^2}$ ,  $q = \sqrt{\beta^2 - k^2}$ ,  $k = 2\pi/\lambda$  is the wavenumber, and  $\varepsilon_i$  gives the dielectric constant in regions  $i = 1, 2$ . The parameter  $l$  is a nonnegative integer. We also use the notation  $J'_l(hr) = \partial J_l(hr)/\partial(hr)$ ,  $K'_l(qr) = \partial K_l(qr)/\partial(qr)$  for derivatives of Bessel functions  $J_l$  and modified Bessel functions of the second kind  $K_l$  of order  $l$ .

Boundary conditions impose the following relations for the constants  $A$ ,  $B$ ,  $C$ , and  $D$ :

$$\frac{B}{A} = \pm \left[ \left( \frac{1}{ha} \right)^2 + \left( \frac{1}{qa} \right)^2 \right] \left[ \frac{J'_l(ha)}{haJ_l(ha)} + \frac{K'_l(qa)}{qaK_l(qa)} \right]^{-1} \quad (\text{A.13})$$

$$\frac{C}{A} = \frac{J_l(ha)}{K_l(qa)} \quad (\text{A.14})$$

$$\frac{D}{A} = \frac{B}{A} \frac{J_l(ha)}{K_l(qa)} - \frac{l^2\beta^2}{k_0^2} \left[ \left( \frac{1}{ha} \right)^2 + \left( \frac{1}{qa} \right)^2 \right]^2, \quad (\text{A.15})$$

so that the knowledge of  $A$  (normalization, Sec. A.3) and the propagation constants  $\beta$  will completely define the system.

## A.2 Propagation constant

An eigenvalue equation determines the propagation constants:

$$\frac{J_{l-1}(ha)}{haJ_l(ha)} = \frac{(n_1^2 + n_2^2)}{4n_1^2} \left[ \frac{K_{l-1}(qa) + K_{l+1}(qa)}{qaK_l(qa)} \right] + \pm R \quad (\text{A.16})$$

$$R = \sqrt{\frac{(n_1^2 - n_2^2)^2}{(4n_1^2)^2} \left[ \frac{K_{l-1}(qa) + K_{l+1}(qa)}{qaK_l(qa)} \right]^2 + \frac{l^2\beta^2}{n_1^2 k_0^2} \left[ \left( \frac{1}{ha} \right)^2 + \left( \frac{1}{qa} \right)^2 \right]^2}, \quad (\text{A.17})$$

and the  $\pm R$  solutions correspond to EH and HE modes, respectively. A normalized frequency called the  $V$ -number is defined by the relation  $V = (2\pi/\lambda)a\sqrt{n_1^2 - n_2^2}$ , which scales the optical frequency by the fiber radius and its index of refraction ( $\sqrt{n_1^2 - n_2^2}$ ). We can numerically solve Eq. A.16 for a particular  $V$ -number and  $l$  by finding the points of intersection of its LHS and RHS. Modes are labeled with subscripts  $lm$ , e.g.  $\text{HE}_{lm}$ , where for a given  $l$ , the successive points of intersection signify increasing  $m$ . Fig. A.1 plots the result of this calculation (where  $n_{\text{eff}} = \beta/k$ ) as a function of  $V$ -number for various families of modes. Note that the cutoff occurs at  $V = 2.405$  and that the fundamental  $\text{HE}_{11}$  mode propagates for any  $V > 0$ .

## A.3 Normalization

The last parameter to determine is  $A$ , which is calculated using energy conservation considerations. We normalize the time-averaged Poynting vector in the  $z$ -direction relative to the input power,

$$P = \langle S_z \rangle_t = A^2 \pi (D_{\text{in}} + D_{\text{out}}), \quad (\text{A.18})$$

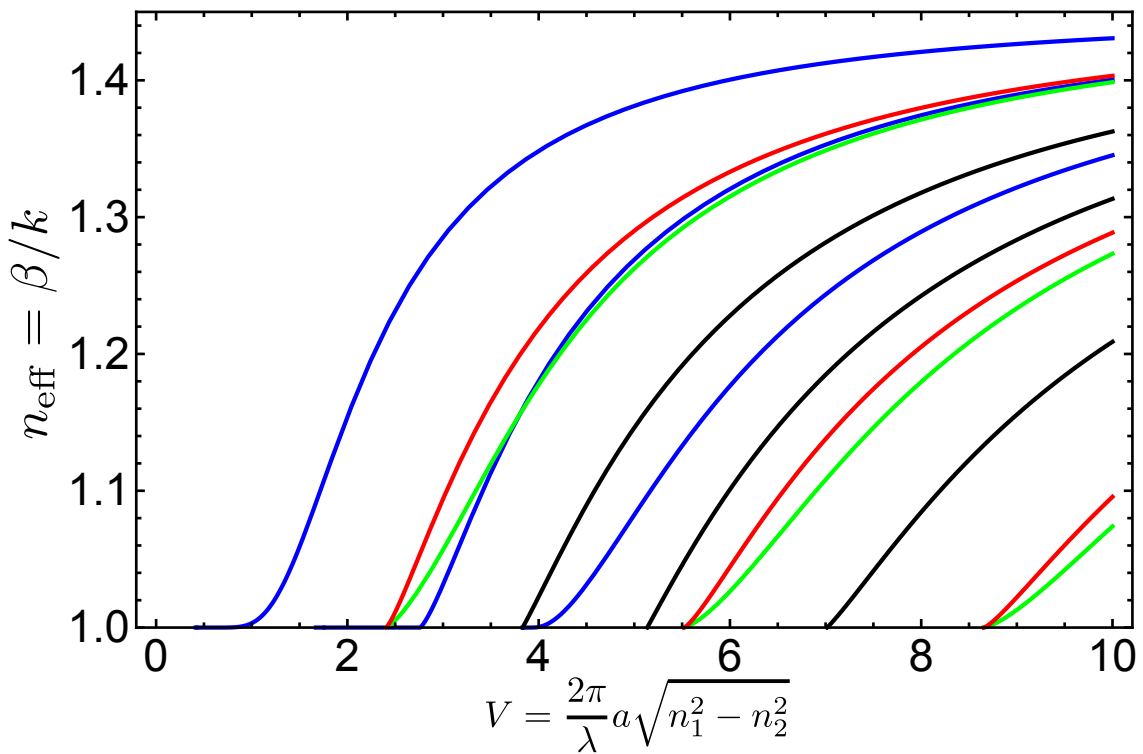


Figure A.1: Effective index of refraction as a function of V-number. The families of modes and their colors are HE (blue), EH (black), TE (red), TM (green) (figure from Ref. [78]).

where  $D_{\text{in}}$  and  $D_{\text{out}}$  will be found analytically. For the  $\text{HE}_{lm}$  and  $\text{EH}_{lm}$  modes (this thesis does not deal with TE and TM modes, so we omit these solutions), these parameters are

$$D_{\text{in}} = \frac{\pi a \beta^2}{4\mu_0 \omega} \frac{\beta}{h^2} [(1+sl)(N_1^2 + sl)[J_{l+1}^2(ha) - J_l(ha)J_{l+2}(ha)] \\ + (1-sl)(N_1^2 - sl)[J_{l-1}^2(ha) - J_l(ha)J_{l-2}(ha)]] \quad (\text{A.19})$$

$$D_{\text{out}} = \frac{-\pi a \beta^2}{4\mu_0 \omega} \frac{\beta}{q^2} \left( \frac{J_l(ha)}{K_l(qa)} \right)^2 [(1+sl)(N_2^2 + sl)[K_{l+1}^2(qa) - K_l(qa)K_{l+2}(ha)] \\ + (1-sl)(N_2^2 - sl)[K_{l-1}^2(qa) - K_l(qa)K_{l-2}(qa)]] \quad (\text{A.20})$$

where  $N_i = n_i k / \beta$  and  $s = B \mu_0 \omega / (il\beta)$  (with  $B$  given by Eq. A.13).

Fig. A.2 offers a summary of this Appendix by plotting the mode structure of the  $\text{HE}_{11}$  mode, showing the intensity as well as the norm of each electric field component normalized to their value at the fiber surface. These values were calculated for a 360-nm diameter fiber with index of refraction  $n_1 = 1.45367$  and propagating wavelength of 780 nm. Note the sharp discontinuity at the fiber surface, as well as the sizable longitudinal component ( $E_z$ ).

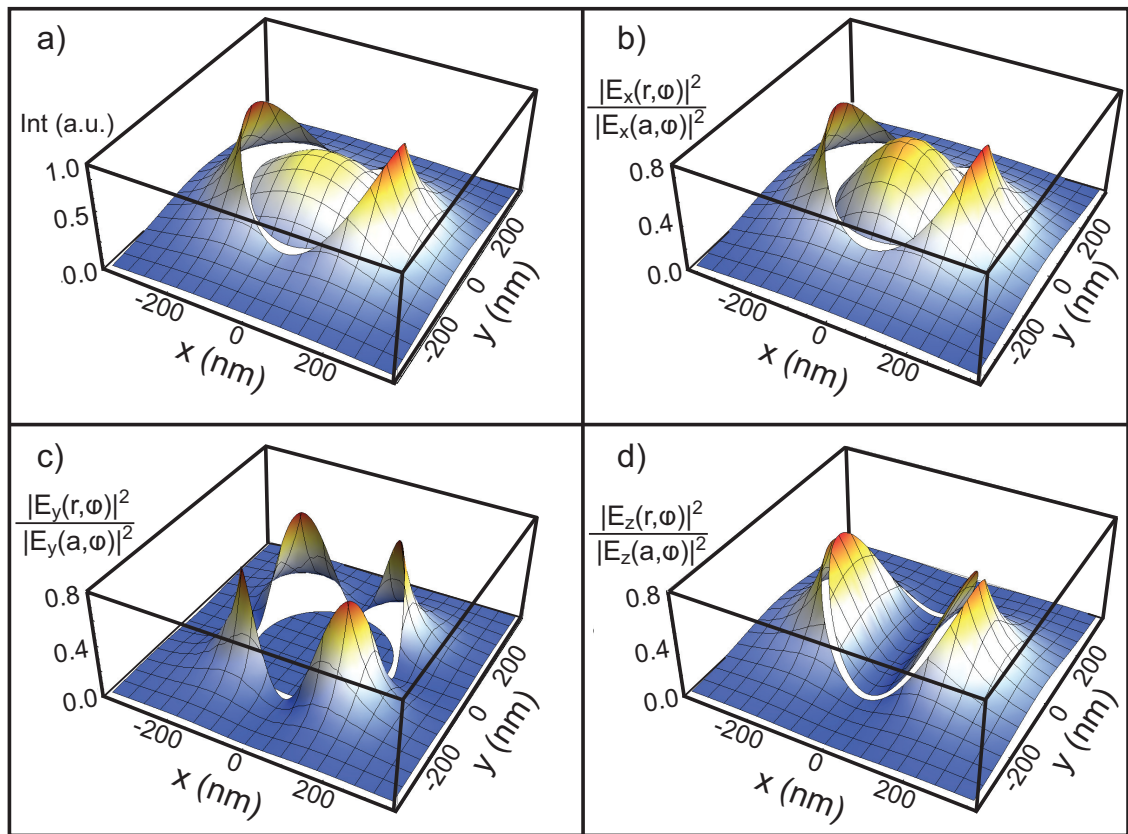


Figure A.2: Fundamental ( $HE_{11}$ ) mode structure of 360-nm diameter nanofiber.  
 (figure from Ref. [78])

## Appendix B: Nanofiber vibrations

This appendix presents a first tentative analysis of something that we discovered while performing the correlation measurements in Chap. 4. Though we are still figuring out the whole picture, we think that this can provide us much quantitative information about the nanofiber and its motion.

A nice feature of TCSPC measurements is that the same time series of photon clicks can be used to study markedly different dynamics. We have seen in Chap. 4 that the autocorrelation function reveals quantum effects on timescales associated with internal atomic dynamics (tens of nanoseconds) and correlations resulting from classical atomic dynamics near the nanofiber (microseconds). Taking the autocorrelation of the same data but for millisecond timescales uncovers information regarding the motion of the ONF. Light from one of the MOT beams couples into the guided mode of the ONF and into the detection path of the SPCMs (see Fig. B.1). This coupling is time-dependent due to vibrations of the nanofiber, and its signature is imprinted in the fluctuations of the light, as seen in Fig. B.2. We also use correlations to measure heating of the fiber from absorption of light propagating through it, as the frequency of vibration lessens with increasing laser power.

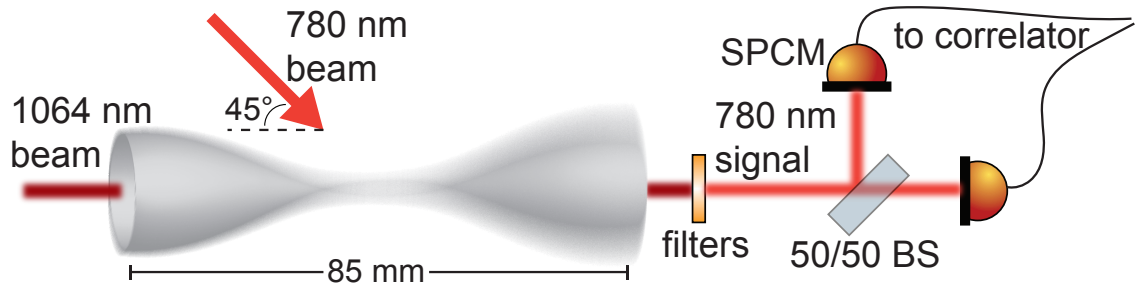


Figure B.1: Experimental setup. The MOT beam at 45° relative to the nanofiber couples into the waist and photon-detection path. Vibrations of the nanofiber modulate the coupling as a function of time, which is measured via correlations.

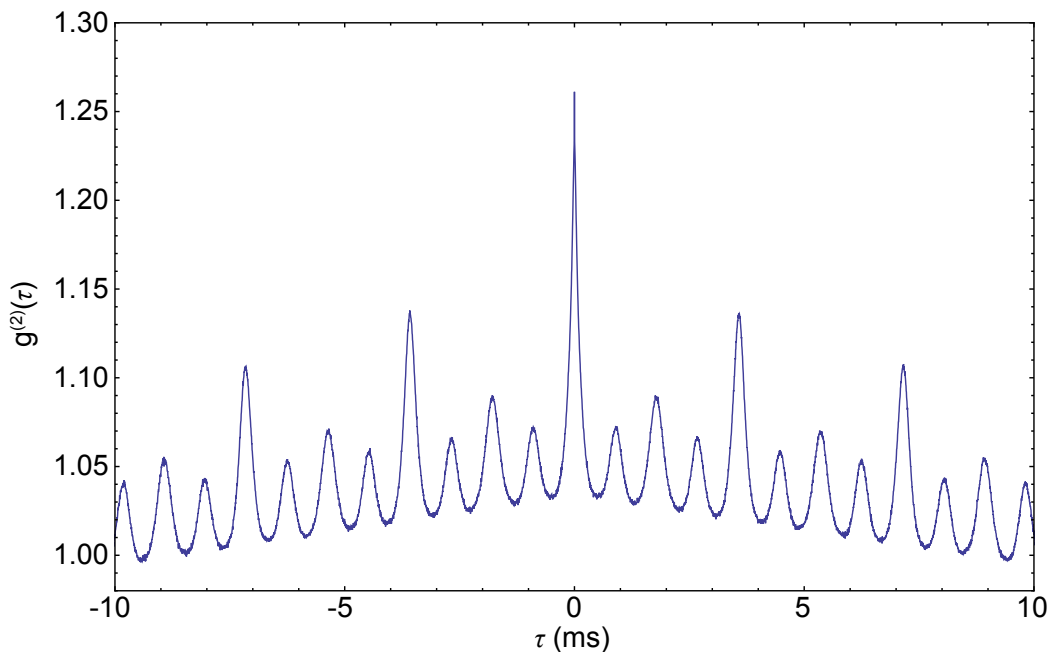


Figure B.2: Correlation function,  $g^{(2)}(\tau)$ , as a function of delay for long time. The triangular shape of the data is an artifact of finite window effects.

## B.1 Transverse vibrational modes of a nanofiber

Finding the vibrational modes of the nanofiber is difficult because the cross-sectional area changes by four orders of magnitude over its profile. The fiber is fixed in the axial direction by the holder so that there is no axial acceleration, and the axial forces must be constant. This leads to vastly different axial stresses in different parts of the fiber given the area variation described above, and the magnitude of the local stress determines the relevant dynamics. In the thicker taper regions, the so-called bending (or cantilever) modes are important because of the non-negligible second moment of area and its resistance to flexing [181]. Along the 500-nm-diameter waist, however, the fiber is well-approximated by a string whose motion is dictated instead by the large axial stresses [181]. This yields the following wave equation for the displacement,  $w(z, t)$ , of the nanofiber [182]:

$$-\frac{\partial^2}{\partial z^2} \left( E I(z) \frac{\partial^2}{\partial z^2} w(z, t) \right) + F_{\text{axial}} \frac{\partial^2}{\partial z^2} w(z, t) = \mu(z) \frac{\partial^2}{\partial t^2} w(z, t), \quad (\text{B.1})$$

where the first term on the LHS comes from the Euler-Bernoulli beam equation (assuming no transverse load), and the second term on the LHS is the standard string wave equation.  $E$  is the Young's modulus (71.7 GPa for fused silica),  $I(z) = \pi r^4(z)/4$  is the second moment of area for a cylinder,  $F_{\text{axial}}$  is the axial force (or tension), and  $\mu(z) = \rho A(z)$  is the linear mass density. The transversal waves described by Eq. B.1 are distinct from the compressional and torsional waves studied in detail in Refs. [103, 181]. Those other waves tend to be much higher frequency ( $\sim 100$  kHz compared to  $\sim 100$  Hz) and couple to the polarization of the light propagating in the fiber, pointing to a potential candidate for parametric heating in nanofiber traps [103].

Given the observed frequencies of hundreds of Hz (see Fig. B.4), we suspect that the modulations in the correlation function arise primarily from bending modes in the tapers. Solutions to the conical, tapered cantilever vibrational modes exist, but generally for boundary conditions where one end is free [183–189]. In our case, the thin waist connects the tapers so that the typically free end is now under tension. The complicated nature of this problem makes it more amenable to numerical FEM solutions, though finding a proper mesh for the disparately sized regions is challenging [181]. We are currently working on the full FEM simulations in COMSOL, but they remain incomplete as a result of the difficulty of properly defining the tension.

We gain some insight, however, by first neglecting the waist and solving the conical cantilever problem, following the treatments in Refs. [183–189]. Ignoring the string term in Eq. B.1, we consider the geometry depicted in Fig. B.3, where a cantilever with circular cross-section tapers from a radius of  $r_0$  to  $r_1$  over a distance  $l$ . This simplified picture approximates the exponential section to be linear so that the fiber taper connects directly to the waist. The exponential horn plays a much stronger role in the case of torsional modes [103].

The material has constant density so that the linear density is  $\mu = \rho A(z) = \pi r^2(z)$ . Since we are finding normal modes of vibration, we separate the displacement function into time- and space-dependent terms,  $w(z, t) = h(z) \sin(\omega t)$ , where  $\omega$  is the angular frequency of the normal mode. Rescaling the problem in terms of a dimensionless distance  $u = x/l$ , we arrive at the following differential equation:

$$\partial_u^4 h - 8 \frac{1-\alpha}{1-(1-\alpha)u} \partial_u^3 h + 12 \left( \frac{1-\alpha}{1-(1-\alpha)u} \right)^2 \partial_u^2 h = \frac{(lk)^4}{(1-(1-\alpha)u)^2} h, \quad (\text{B.2})$$

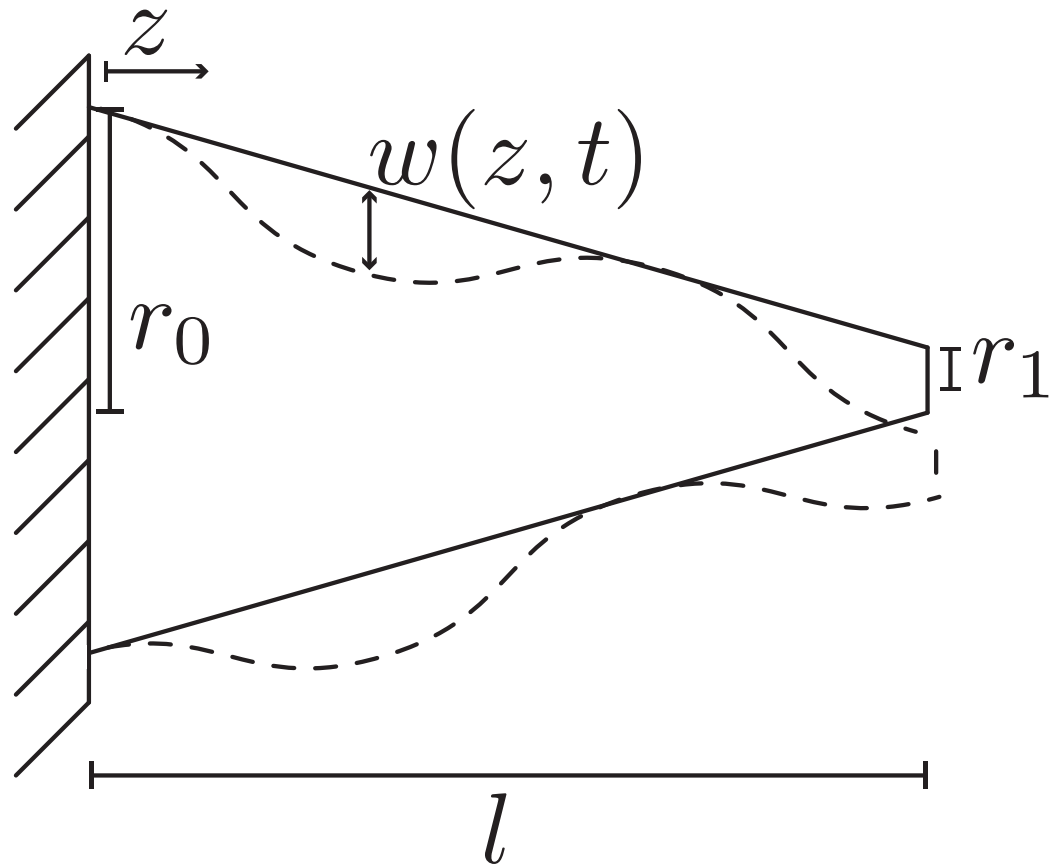


Figure B.3: Geometry of the problem of a conical cantilever. The cantilever tapers from radius  $r_0$  to  $r_1$  over a distance  $l$  and has a circular cross-section. The large radius end at  $z = 0$  obeys a fixed boundary condition. The displacement is given by  $w(z, t)$ , and the dotted line displays an exaggerated vibrational mode.

where  $\partial_i$  denotes derivation with respect to coordinate  $i$ ,  $\alpha = r_1/r_0$ , and  $k = 4\rho\omega^2/Er_0^2$ .

To find the normal modes, we solve this eigenvalue equation numerically in Mathematica, applying clamped ( $h = \partial_u h = 0$ ) boundary conditions at  $u = 0$  and sliding boundary conditions ( $\partial_u h = \partial_u^3 h = 0$ ) at  $u = 1$ . We consider a cantilever made out of fused silica ( $\rho = 2.203 \text{ g}\cdot\text{cm}^3$ ,  $E = 71.7 \text{ GPa}$ ) with length  $l = 39 \text{ mm}$ , and with large and small radii of  $r_0 = 62.5 \mu\text{m}$  and  $r_1 = 250 \text{ nm}$ , respectively. This yields frequencies of  $\omega/2\pi = 161.5, 392.3 \text{ Hz}$  for the first two normal modes. We confirm that these frequencies match the FEM simulations to within 2 Hz for the case of an untensioned cantilever with these dimensions.

The FEM simulations also illustrate that the transversal modes have the same frequency for the full fiber with two tapers connected by the nanofiber waist. In the case of no tension, the two cantilevers are essentially independent. Adding tension increases the vibrational frequencies, and we can approximate the effect by following the treatment in Refs. [188, 190, 191]. The normal mode frequencies  $\omega_n$  for small  $n$  become

$$\omega'_n = \omega_n \sqrt{1 + U_n}, \quad (\text{B.3})$$

where

$$U_n = \frac{4}{(2n-1)^2\pi^2} \frac{F_{\text{axial}}l^2}{EI}. \quad (\text{B.4})$$

We will use this result to characterize our observed vibrations.

Fig. B.4 displays the power spectrum of an exemplary long-time correlation measurement. We can clearly identify three features: the leftmost peak corresponds to the slow oscillations of the manipulator mount that holds the fiber, and the latter two are nanofiber vibrations. We note that sidebands from the manipulator vibrations are visible on the peak at approximately 555 Hz.

We do not have a good physical reason for why the first two peaks corresponding to nanofiber vibrations look like harmonics, which should not be the case for cantilever modes. One hypothesis is that the “fundamental” vibration occurs when the cantilevers oscillate in phase, and the “harmonic” arises when the cantilevers are out of phase so that the waist moves through its optimally-coupled position twice per oscillation. The other explanation is that the cantilever modes begin to exhibit string-like behavior as more tension is applied, and the frequency spacing between modes becomes more harmonic. FEM simulations with tension should help to elucidate this question.

Assuming that the peak at 277 Hz is the first vibrational mode of the fiber, we use Eq. B.4 to estimate the tension of the nanofiber. We use an average second moment of area,  $I$ , and  $n = 1$  to arrive at  $F_{\text{axial}} \approx 0.14$  mN. Translating this to total initial elongation (see Chap. 2 for a discussion of post-pull tensioning) amounts to integrating the local strain,  $\epsilon(z)$  over the length of the fiber. We use the nonlinear stress-strain equation,  $\sigma(z) = E \epsilon(z)(1 + \alpha\epsilon(z)/2)$ , with  $\alpha = 6$ , and define the strain  $\sigma(z) = F_{\text{axial}}/A(z)$  [192]. Solving for  $\epsilon(z)$  and integrating over our fiber geometry with  $F_{\text{axial}} = 0.14$  mN, we obtain a total initial elongation of 69  $\mu\text{m}$ . We do not have an exact value from our nanofiber tensioning process, but this is a reasonable estimate based on how far the motors are moved after the pull.

## B.2 Effect of heating

When laser light is sent through the nanofiber, it heats as a result of surface absorption [168, 181]. The thermal expansion of the nanofiber relaxes the axial load, causing the fiber vibration frequency to decrease. We observe this effect in our correlation measurements when 1064-nm light is transmitted through the nanofiber, as illustrated in the

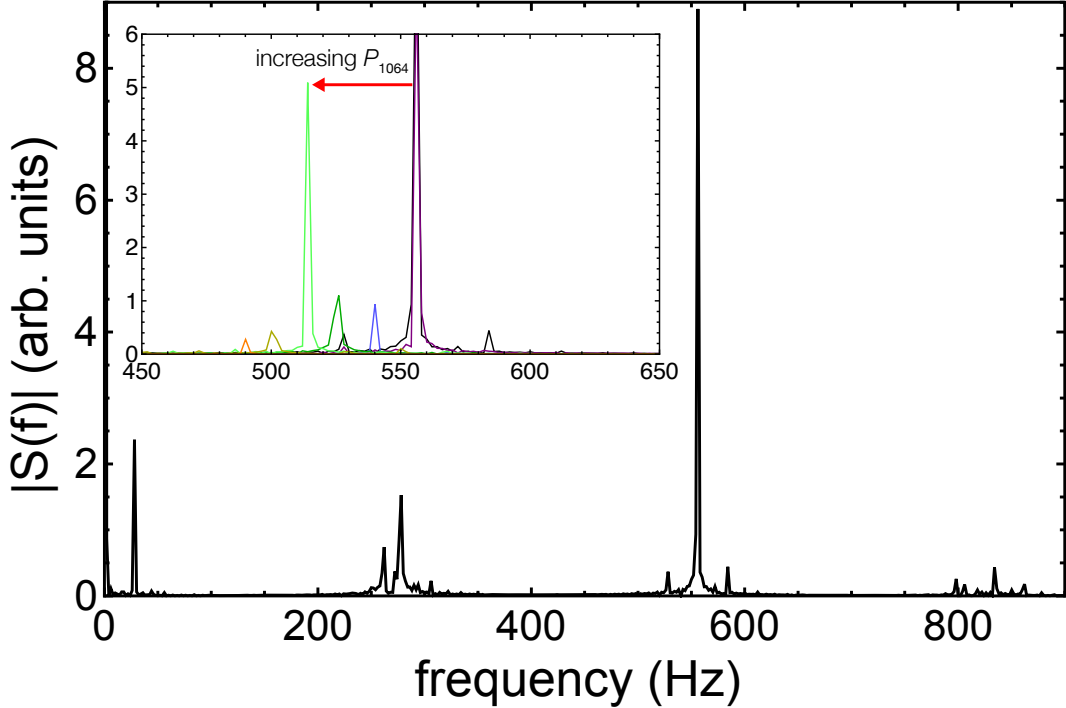


Figure B.4: Power spectrum of the long-time correlation function, such as in Fig. B.2. Inset shows the power spectra on a zoomed frequency axis for 1064 nm laser powers ranging from 0 mW to 7.5 mW (red arrow indicates direction of increasing power).

inset of Fig. B.4. We extract the fractional change in the mode frequency as a function of transmitted 1064-nm laser power and plot it in Fig. B.5. The largest fractional change of 12% for 7.5 mW of 1064-nm light corresponds to change of  $23 \mu\text{m}$  relative to the initial, pre-tensioned fiber, following the above analysis. The fractional frequency resolution of about 0.5% translates to detecting fiber-length changes of about  $2 \mu\text{m}$ .

### B.3 Heterodyne technique

The heterodyne technique mentioned briefly in Chap. 7 has also confirmed the presence of these vibrations. A local oscillator beam is sent down a reference path, and a roughly 1-MHz-detuned signal beam propagates down the fiber. These are overlapped in

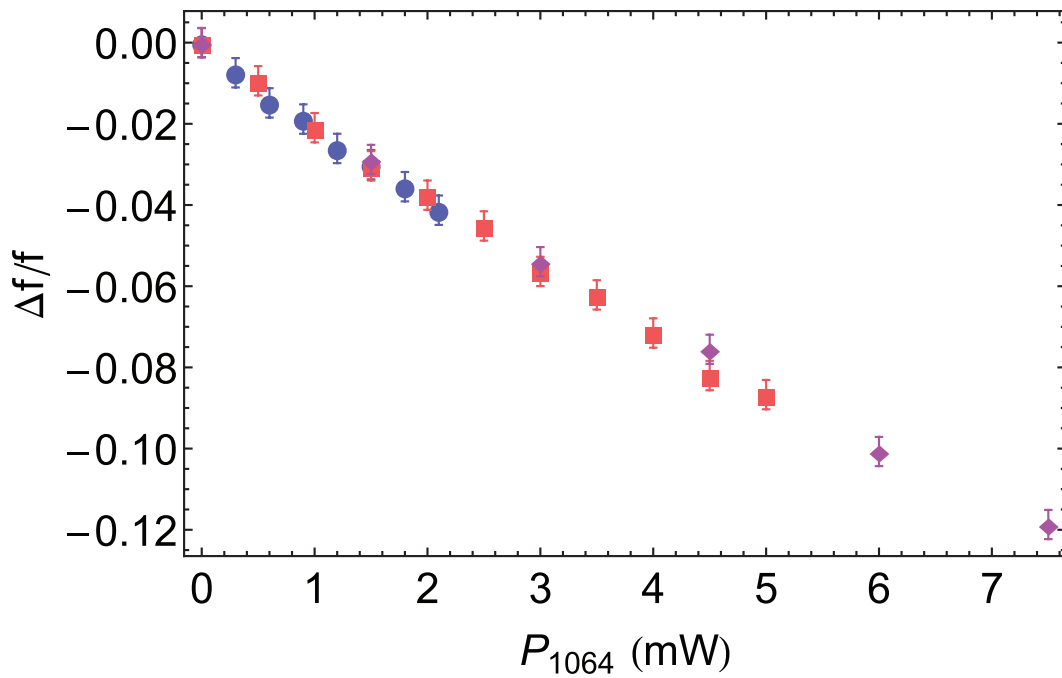


Figure B.5: Fractional change in nanofiber vibrational frequency as a function of 1064 nm laser power. The error bars represent the 3 dB point of the peaks in the power spectrum. The different colors correspond to data taken on different days.

the same spatial mode, and the beatnote is detected with a lock-in amplifier. As discussed earlier, this is a highly sensitive measurement scheme that has been able to detect, in real time, the Doppler shift of the signal light as the thermo-optic effect changes the optical path length. High signal-to-noise is maintained when sending only microwatts of heating power through it.

During the writing of this thesis, we have also seen that when the UHV manipulator is tapped, low-frequency signals appear in the lock-in signal. They correspond precisely with the 277 Hz and 555 Hz signals mentioned above, among other frequencies not detected with the correlation technique. We can also discern signals that appear to be torsional modes, starting at 180 kHz. The heterodyne scheme will enhance our capability to distinguish nanofiber vibrations modes and how they evolve during heating and cooling. It is much simpler than using correlations, as it requires very little averaging and minimal post-processing of the data; the signal is observed directly on an oscilloscope.

## Appendix C: Calculating van der Waals coefficients for $^{87}\text{Rb}$

Knowing well the surface interactions is important for calculating the full potential that nanofiber-trapped atoms see, as well as to understand the dynamics of untrapped atoms moving near the nanofiber. Numbers for the van der Waals coefficients of cesium atoms near fused silica are given, for example, in Ref. [19], but we have not found consistent values for rubidium [193,194]. This Appendix outlines the calculation of these coefficients, following the treatment in Refs. [19,179].

### C.1 Index of refraction

The Sellmeier equation for fused silica calculates the index of refraction for wavelengths in range of  $0.2\text{--}7\,\mu\text{m}$ , over which the absorption coefficient is negligibly small [195]:

$$n^2(\lambda) \equiv \frac{\varepsilon(\lambda)}{\varepsilon_0} = 1 + \frac{0.6961663\lambda^2}{\lambda^2 - 0.0684043^2} + \frac{0.4079426\lambda^2}{\lambda^2 - 0.1162414^2} + \frac{0.8974794\lambda^2}{\lambda^2 - 9.896161^2}, \quad (\text{C.1})$$

where  $\lambda$  is in micrometers. Fig. C.1 illustrates the behavior of this function from 0.2 to 7  $\mu\text{m}$ . Because we will later need to integrate the dielectric response function over imaginary frequencies, we recast Eq. C.1 from wavelength to these imaginary frequencies.

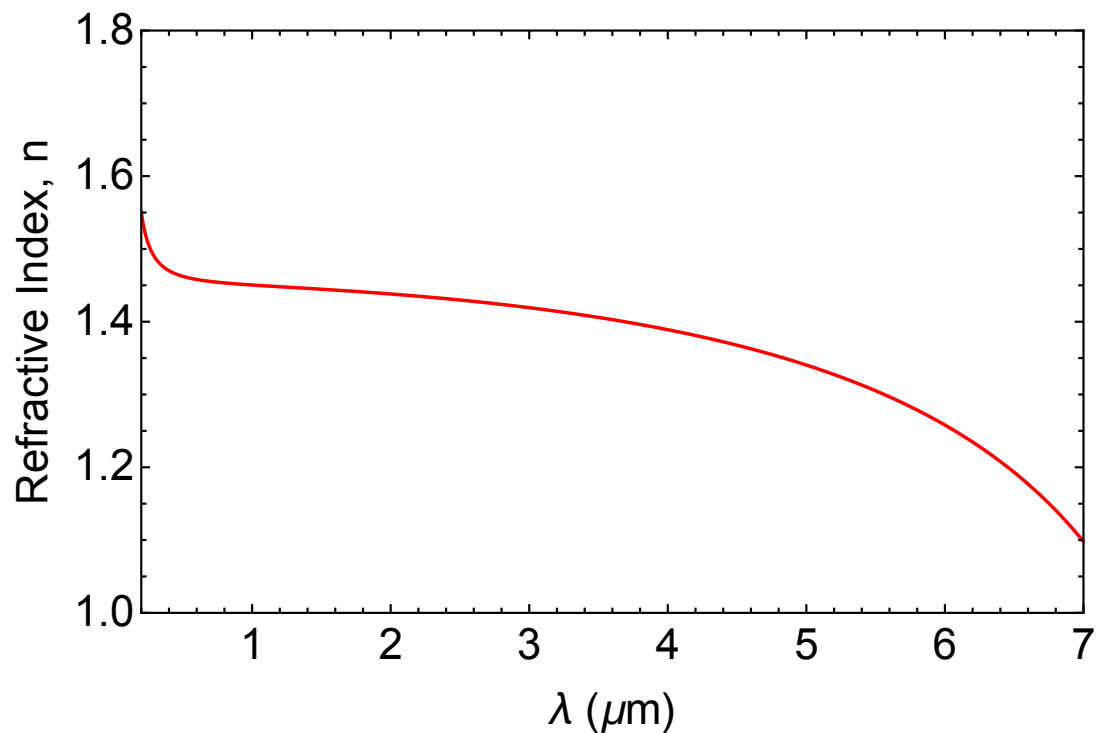


Figure C.1: Index of refraction of fused silica for  $\lambda$  between 0.2 and 7  $\mu\text{m}$ , calculated using the Sellmeier equation (Eq. C.1).

## C.2 Atomic polarizabilities

We also need the dynamical scalar polarizability of  $^{87}\text{Rb}$ , which we calculate following the treatment in Ref. [196], but using the reduced dipole matrix element values and energy levels for the  $^{87}\text{Rb}$   $D_2$  line from Refs. [197, 198]. The scalar polarizability for an atom in the hyperfine level  $|nJF\rangle$  is [196]

$$\alpha_{nJF}^s = \frac{1}{\sqrt{3(2J+1)}} (-1)^{J+1} \sum_{n'J'} (-1)^{J'} \left\{ \begin{matrix} 1 & 0 & 1 \\ J & J' & J \end{matrix} \right\} |\langle n'J' | \mathbf{d} | nJ \rangle|^2 \quad (\text{C.2})$$

$$\times \frac{1}{\hbar} \text{Re} \left( \frac{1}{\omega_{n'J'nJ} - \omega - i\gamma_{n'J'nJ}/2} + \frac{1}{\omega_{n'J'nJ} + \omega + i\gamma_{n'J'nJ}/2} \right), \quad (\text{C.3})$$

where we sum over transitions to allowed levels  $|n'J'\rangle$ , and  $\langle n'J' | \mathbf{d} | nJ \rangle$  is the reduced dipole matrix element. The symbol  $\left\{ \begin{smallmatrix} j_1 & j_2 & j_3 \\ j_4 & j_5 & j_6 \end{smallmatrix} \right\}$  represents the Wigner 6- $j$  symbol, and  $\omega_{n'J'nJ}$  and  $\gamma_{n'J'nJ}$  correspond to the frequency and linewidth, respectively, of transitions between states  $|nJ\rangle$  and  $|n'J'\rangle$ .

In Fig. C.2 we plot the scalar polarizabilities for the  $5S_{1/2}$  (blue) and  $5P_{3/2}$  (orange) states of  $^{87}\text{Rb}$  as a function of imaginary angular frequency. For use in numerical integration later, we generate interpolation functions for both of these lists that are valid out to values of angular frequency of  $\sim 10^{36} \text{ rad} \cdot \text{s}^{-1}$ .

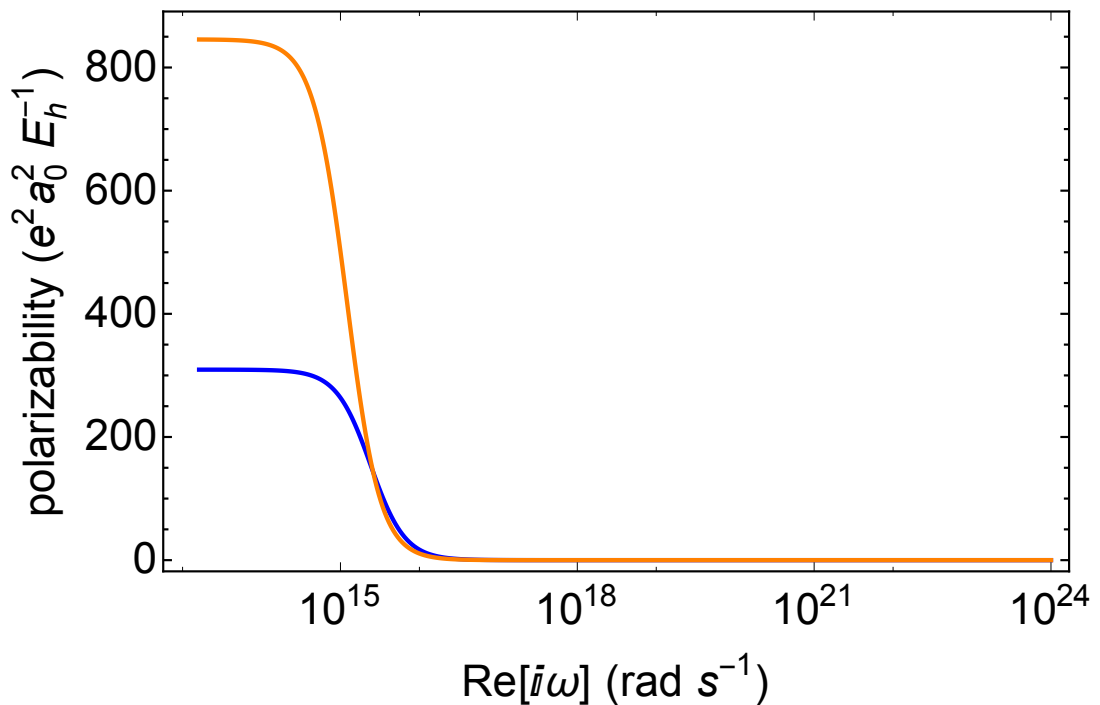


Figure C.2: Scalar polarizabilities for the  $5S_{1/2}$  (blue) and  $5P_{3/2}$  (orange) states of  $^{87}\text{Rb}$  as a function of imaginary angular frequency. The polarizability is given in atomic units of  $e^2 a_0^2 / E_h$ , with  $E_h = m_e e^4 / (4\pi\epsilon_0\hbar)^2 = m_e c^2 \alpha^2$  being the Hartree energy (approximately twice the ionization energy of ground-state hydrogen). Note the logarithmic horizontal axis.

### C.3 $C_3$ and $C_4$ coefficients

We insert the above results for the dielectric response and polarizabilities into the following integral to calculate  $C_3$  [19, 179]:

$$C_3 = \frac{\hbar}{16\pi^2\epsilon_0} \int_0^\infty d\omega \alpha_{nJF}^s(i\omega) \frac{\epsilon(i\omega) - \epsilon_0}{\epsilon_0 + \epsilon(i\omega)}, \quad (\text{C.4})$$

where we use the appropriate polarizability for either the  $5S_{1/2}$  or  $5P_{3/2}$  state. Note that we are also ignoring geometric effects due to the curvature of the nanofiber, which is unimportant for small distances (see Refs. [19, 121, 122, 179] for more details). To calculate the Casimir-Polder  $C_4$  coefficients, we make use of an approximate formula assuming an infinite dielectric [179, 199]:

$$C_4 = \frac{3}{8\pi} \frac{\hbar\alpha_{nJF}^s(0)}{4\pi\epsilon_0} \frac{n^2 - 1}{n^2 + (30/23)n + 7/23}, \quad (\text{C.5})$$

where we use the static polarizability (Eq. C.2 for  $\omega = 0$ ). Table C.1 summarizes our results. As a check, we verified our calculation for cesium against the values quoted in the literature [19].

State	$C_3 (\times 10^{-49} \text{ J} \cdot \mu\text{m}^3)$	$C_4 (\times 10^{-56} \text{ J} \cdot \mu\text{m}^4)$
$5S_{1/2}$	4.94	4.47
$5P_{3/2}$	7.05	12.2

Table C.1: van der Waals and Casimir-Polder coefficients for  $^{87}\text{Rb}$  near fused silica for both the  $5S_{1/2}$  or  $5P_{3/2}$  states.

## Bibliography

- [1] S. Haroche and J.-M. Raimond, *Exploring the Quantum: Atoms, Cavities, and Photons*. Oxford University Press, 2006.
- [2] H. J. Kimble, “Strong Interactions of Single Atoms and Photons in Cavity QED,” *Phys. Scr.*, vol. T76, p. 127, Jan. 1998.
- [3] E. M. Purcell, “Spontaneous emission probabilities at radio frequencies,” *Phys. Rev.*, vol. 69, p. 681, 1946.
- [4] D. Kleppner, “Inhibited Spontaneous Emission,” *Phys. Rev. Lett.*, vol. 47, pp. 233–236, July 1981.
- [5] S. Haroche, “Nobel Lecture: Controlling photons in a box and exploring the quantum to classical boundary,” *Rev. Mod. Phys.*, vol. 85, pp. 1083–1102, July 2013.
- [6] A. Wallraff, D. I. Schuster, A. Blais, L. Frunzio, R.-S. Huang, J. Majer, S. Kumar, S. M. Girvin, and R. J. Schoelkopf, “Strong coupling of a single photon to a superconducting qubit using circuit quantum electrodynamics.,” *Nature*, vol. 431, pp. 162–7, Sept. 2004.
- [7] R. J. Thompson, G. Rempe, and H. J. Kimble, “Observation of normal-mode splitting for an atom in an optical cavity,” *Phys. Rev. Lett.*, vol. 68, pp. 1132–1135, Jan. 1992.
- [8] D. J. Wineland, “Nobel Lecture: Superposition, entanglement, and raising Schrödinger’s cat,” *Rev. Mod. Phys.*, vol. 85, pp. 1103–1114, July 2013.
- [9] A. Blais, R. Huang, A. Wallraff, S. Girvin, and R. Schoelkopf, “Cavity quantum electrodynamics for superconducting electrical circuits: An architecture for quantum computation,” *Phys. Rev. A*, vol. 69, p. 62320, June 2004.

- [10] H. Tanji-Suzuki, I. D. Leroux, M. H. Schleier-Smith, M. Cetina, A. T. Grier, J. Simon, and V. Vuletić, “Interaction between Atomic Ensembles and Optical Resonators: Classical Description,” in *Adv. At. Mol. Opt. Phys.*, vol. 60, pp. 201–237, Elsevier, 2011.
- [11] D. Phillips, A. Fleischhauer, A. Mair, R. Walsworth, and M. Lukin, “Storage of Light in Atomic Vapor,” *Phys. Rev. Lett.*, vol. 86, pp. 783–786, Jan. 2001.
- [12] Y. Makhlin, G. Schön, and A. Shnirman, “Quantum-state engineering with Josephson-junction devices,” *Rev. Mod. Phys.*, vol. 73, pp. 357–400, May 2001.
- [13] M. Stobińska, G. Alber, and G. Leuchs, “Perfect excitation of a matter qubit by a single photon in free space,” *Europhysics Letters*, vol. 86, p. 14007, Jan. 2009.
- [14] A. Golla, B. Chalopin, M. Bader, I. Harder, K. Mantel, R. Maiwald, N. Lindlein, M. Sondermann, and G. Leuchs, “Generation of a wave packet tailored to efficient free space excitation of a single atom,” *Eur. Phys. J. D*, vol. 66, p. 190, July 2012.
- [15] S. Heugel, B. Chalopin, M. Sondermann, and G. Leuchs, “Collecting more than half the fluorescence photons from a single ion,” *Phys. Rev. A*, vol. 86, p. 043431, Jan. 2012.
- [16] M. K. Tey, Z. Chen, S. A. Aljunid, B. Chng, F. Huber, G. Maslennikov, and C. Kurtsiefer, “Strong interaction between light and a single trapped atom without the need for a cavity,” *Nat. Phys.*, vol. 4, pp. 924–927, Oct. 2008.
- [17] G. Hétet, L. Slodička, M. Hennrich, and R. Blatt, “Single Atom as a Mirror of an Optical Cavity,” *Phys. Rev. Lett.*, vol. 107, p. 133002, Sept. 2011.
- [18] E. W. Streed, A. Jechow, B. G. Norton, and D. Kielpinski, “Absorption imaging of a single atom.,” *Nat. Commun.*, vol. 3, p. 933, Jan. 2012.
- [19] F. Le Kien, V. Balykin, and K. Hakuta, “Atom trap and waveguide using a two-color evanescent light field around a subwavelength-diameter optical fiber,” *Phys. Rev. A*, vol. 70, p. 63403, Dec. 2004.
- [20] D. E. Chang, O. Painter, and H. J. Kimble, “Trapped atoms in one-dimensional photonic crystals,” *New J. Phys.*, vol. 15, p. 083026, Jan. 2013.
- [21] E. Vetsch, D. Reitz, G. Sagué, R. Schmidt, S. Dawkins, and A. Rauschenbeutel, “Optical Interface Created by Laser-Cooled Atoms Trapped in the Evanescent Field Surrounding an Optical Nanofiber,” *Phys. Rev. Lett.*, vol. 104, p. 203603, May 2010.
- [22] A. Goban, K. S. Choi, D. J. Alton, D. Ding, C. Lacroûte, M. Pototschnig, T. Thiele, N. P. Stern, and H. J. Kimble, “Demonstration of a State-Insensitive, Compensated Nanofiber Trap,” *Phys. Rev. Lett.*, vol. 109, p. 033603, July 2012.

- [23] J.-B. Béguin, E. Bookjans, S. Christensen, H. Sørensen, J. Müller, E. Polzik, and J. Appel, “Generation and Detection of a Sub-Poissonian Atom Number Distribution in a One-Dimensional Optical Lattice,” *Phys. Rev. Lett.*, vol. 113, p. 263603, Dec. 2014.
- [24] J. Lee, J. A. Grover, J. E. Hoffman, L. A. Orozco, and S. L. Rolston, “Inhomogeneous broadening of optical transitions of  $^{87}\text{Rb}$  atoms in an optical nanofiber trap,” *arXiv:1412.6754v1*, Dec. 2014.
- [25] J. D. Thompson, T. G. Tiecke, N. P. de Leon, J. Feist, A. V. Akimov, M. Gullans, A. S. Zibrov, V. Vuletić, and M. D. Lukin, “Coupling a Single Trapped Atom to a Nanoscale Optical Cavity,” *Science*, vol. 340, p. 1202, Jan. 2013.
- [26] A. Goban, C.-L. Hung, S.-P. Yu, J. Hood, J. Muniz, J. Lee, M. Martin, A. McClung, K. Choi, D. Chang, O. Painter, and H. Kimble, “Atom–light interactions in photonic crystals,” *Nat. Commun.*, vol. 5, May 2014.
- [27] A. Goban, C. L. Hung, J. D. Hood, S. P. Yu, J. A. Muniz, O. Painter, and H. J. Kimble, “Superradiance for atoms trapped along a photonic crystal waveguide,” *arXiv:1503.04503*, Mar. 2015.
- [28] R. N. Patel, T. Schröder, N. Wan, L. Li, S. L. Mouradian, E. H. Chen, and D. R. Englund, “Efficient Photon Coupling from a Diamond Nitrogen Vacancy Centre by Integration with Silica Fibre,” *arXiv:1502.07849*, Feb. 2015.
- [29] D. Reitz, C. Sayrin, R. Mitsch, P. Schneeweiss, and A. Rauschenbeutel, “Coherence Properties of Nanofiber-Trapped Cesium Atoms,” *Phys. Rev. Lett.*, vol. 110, p. 243603, June 2013.
- [30] C. Wuttke, M. Becker, S. Brückner, M. Rothhardt, and A. Rauschenbeutel, “Nanofiber Fabry-Perot microresonator for nonlinear optics and cavity quantum electrodynamics.,” *Opt. Lett.*, vol. 37, pp. 1949–51, June 2012.
- [31] M. Sadgrove, R. Yalla, K. P. Nayak, and K. Hakuta, “Photonic crystal nanofiber using an external grating,” *Opt. Lett.*, vol. 38, pp. 2542–2545, June 2013.
- [32] R. Yalla, M. Sadgrove, K. P. Nayak, and K. Hakuta, “Cavity Quantum Electrodynamics on a Nanofiber Using a Composite Photonic Crystal Cavity,” *Phys. Rev. Lett.*, vol. 113, p. 143601, Sept. 2014.
- [33] J. Petersen, J. Volz, and A. Rauschenbeutel, “Chiral nanophotonic waveguide interface based on spin-orbit interaction of light.,” *Science*, vol. 346, pp. 67–71, Sept. 2014.
- [34] C. Sayrin, C. Junge, R. Mitsch, B. Albrecht, D. O’Shea, P. Schneeweiss, J. Volz, and A. Rauschenbeutel, “Optical diode based on the chirality of guided photons,” *arXiv:1502.01549*, Feb. 2015.

- [35] J. Volz, M. Scheucher, C. Junge, and A. Rauschenbeutel, “Nonlinear  $\pi$  phase shift for single fibre-guided photons interacting with a single resonator-enhanced atom,” *Nat. Photonics*, vol. 8, pp. 965–970, Nov. 2014.
- [36] R. Yalla, F. Le Kien, M. Morinaga, and K. Hakuta, “Efficient channeling of fluorescence photons from single quantum dots into guided modes of optical nanofiber,” *Phys. Rev. Lett.*, vol. 109, p. 063602, Jan. 2012.
- [37] B. Gouraud, D. Maxein, A. Nicolas, O. Morin, and J. Laurat, “Demonstration of a memory for tightly guided light in an optical nanofiber,” *arXiv:1502.01458*, Feb. 2015.
- [38] C. Sayrin, C. Clausen, B. Albrecht, P. Schneeweiss, and A. Rauschenbeutel, “Storage of fiber-guided light in a nanofiber-trapped ensemble of cold atoms,” *arXiv:1502.01151*, Feb. 2015.
- [39] L. M. Duan, M. D. Lukin, J. I. Cirac, and P. Zoller, “Long-distance quantum communication with atomic ensembles and linear optics.,” *Nature*, vol. 414, pp. 413–8, Nov. 2001.
- [40] H. J. Kimble, “The quantum internet.,” *Nature*, vol. 453, pp. 1023–30, June 2008.
- [41] L. DiCarlo, J. M. Chow, J. M. Gambetta, L. S. Bishop, B. R. Johnson, D. I. Schuster, J. Majer, A. Blais, L. Frunzio, S. M. Girvin, and R. J. Schoelkopf, “Demonstration of two-qubit algorithms with a superconducting quantum processor.,” *Nature*, vol. 460, pp. 240–4, July 2009.
- [42] E. Lucero, R. Barends, Y. Chen, J. Kelly, M. Mariantoni, A. Megrant, P. O’Malley, D. Sank, A. Vainsencher, J. Wenner, T. White, Y. Yin, A. N. Cleland, and J. M. Martinis, “Computing prime factors with a Josephson phase qubit quantum processor,” *Nat. Phys.*, vol. 8, pp. 719–723, Aug. 2012.
- [43] L. DiCarlo, M. D. Reed, L. Sun, B. R. Johnson, J. M. Chow, J. M. Gambetta, L. Frunzio, S. M. Girvin, M. H. Devoret, and R. J. Schoelkopf, “Preparation and measurement of three-qubit entanglement in a superconducting circuit.,” *Nature*, vol. 467, pp. 574–8, Sept. 2010.
- [44] R. Barends, L. Lamata, J. Kelly, L. García-Álvarez, A. G. Fowler, A. Megrant, E. Jeffrey, T. C. White, D. Sank, J. Y. Mutus, B. Campbell, Y. Chen, Z. Chen, B. Chiaro, A. Dunsworth, I. C. Hoi, C. Neill, P. J. J. O’Malley, C. Quintana, P. Roushan, A. Vainsencher, J. Wenner, E. Solano, and J. M. Martinis, “Digital quantum simulation of fermionic models with a superconducting circuit,” *arXiv:1501.07703*, Jan. 2015.
- [45] P. Treutlein, P. Hommelhoff, T. Steinmetz, T. Hänsch, and J. Reichel, “Coherence in Microchip Traps,” *Phys. Rev. Lett.*, vol. 92, p. 203005, May 2004.

- [46] Z.-L. Xiang, S. Ashhab, J. You, and F. Nori, “Hybrid quantum circuits: Superconducting circuits interacting with other quantum systems,” *Rev. Mod. Phys.*, vol. 85, pp. 623–653, Apr. 2013.
- [47] D. M. Pozar, *Microwave Engineering*. Wile, 4th ed., 2011.
- [48] C. A. Regal and K. W. Lehnert, “From cavity electromechanics to cavity optomechanics,” *J. Phys. Conf. Ser.*, vol. 264, p. 012025, Jan. 2011.
- [49] M. Hafezi, Z. Kim, S. L. Rolston, L. A. Orozco, B. L. Lev, and J. M. Taylor, “Atomic interface between microwave and optical photons,” *Phys. Rev. A*, vol. 85, p. 020302, Feb. 2012.
- [50] R. W. Andrews, R. W. Peterson, T. P. Purdy, K. Cicak, R. W. Simmonds, C. A. Regal, and K. W. Lehnert, “Bidirectional and efficient conversion between microwave and optical light,” *Nat. Phys.*, vol. 10, pp. 321–326, Oct. 2014.
- [51] D. Marcos, M. Wubs, J. Taylor, R. Aguado, M. Lukin, and A. Sørensen, “Coupling nitrogen-vacancy centers in diamond to superconducting flux qubits,” *Phys. Rev. Lett.*, vol. 105, no. 21, p. 210501, 2010.
- [52] D. Schuster, A. Sears, E. Ginossar, L. Dicarlo, L. Frunzio, J. Morton, H. Wu, G. Briggs, B. Buckley, D. Awschalom, and R. Schoelkopf, “High-Cooperativity Coupling of Electron-Spin Ensembles to Superconducting Cavities,” *Phys. Rev. Lett.*, vol. 105, p. 140501, Sept. 2010.
- [53] Y. Kubo, F. R. Ong, P. Bertet, D. Vion, V. Jacques, D. Zheng, A. Dréau, J.-F. Roch, A. Auffeves, F. Jelezko, J. Wrachtrup, M. F. Barthe, P. Bergonzo, and D. Esteve, “Strong Coupling of a Spin Ensemble to a Superconducting Resonator,” *Phys. Rev. Lett.*, vol. 105, p. 140502, Sept. 2010.
- [54] H. Wu, R. E. George, J. H. Wesenberg, K. Mølmer, D. I. Schuster, R. J. Schoelkopf, K. M. Itoh, A. Ardavan, J. J. L. Morton, and G. A. D. Briggs, “Storage of Multiple Coherent Microwave Excitations in an Electron Spin Ensemble,” *Phys. Rev. Lett.*, vol. 105, p. 140503, Sept. 2010.
- [55] Y. Kubo, C. Grezes, A. Dewes, T. Umeda, J. Isoya, H. Sumiya, N. Morishita, H. Abe, S. Onoda, T. Ohshima, V. Jacques, A. Dréau, J.-F. Roch, I. Diniz, A. Auffeves, D. Vion, D. Esteve, and P. Bertet, “Hybrid Quantum Circuit with a Superconducting Qubit Coupled to a Spin Ensemble,” *Phys. Rev. Lett.*, vol. 107, p. 220501, Nov. 2011.
- [56] Y. Kubo, I. Diniz, A. Dewes, V. Jacques, A. Dréau, J.-F. Roch, A. Auffeves, D. Vion, D. Esteve, and P. Bertet, “Storage and retrieval of a microwave field in a spin ensemble,” *Phys. Rev. A*, vol. 85, p. 012333, Jan. 2012.

- [57] Y. Kubo, I. Diniz, C. Grezes, T. Umeda, J. Isoya, H. Sumiya, T. Yamamoto, H. Abe, S. Onoda, T. Ohshima, V. Jacques, A. Dréau, J.-F. Roch, A. Auffeves, D. Vion, D. Esteve, and P. Bertet, “Electron spin resonance detected by a superconducting qubit,” *Phys. Rev. B*, vol. 86, p. 064514, Aug. 2012.
- [58] C. Grezes, B. Julsgaard, Y. Kubo, M. Stern, T. Umeda, J. Isoya, H. Sumiya, H. Abe, S. Onoda, T. Ohshima, V. Jacques, J. Esteve, D. Vion, D. Esteve, K. Mølmer, and P. Bertet, “Multimode Storage and Retrieval of Microwave Fields in a Spin Ensemble,” *Phys. Rev. X*, vol. 4, p. 021049, June 2014.
- [59] A. Imamoğlu, “Cavity QED Based on Collective Magnetic Dipole Coupling: Spin Ensembles as Hybrid Two-Level Systems,” *Phys. Rev. Lett.*, vol. 102, p. 083602, Feb. 2009.
- [60] D. Petrosyan, G. Bensky, G. Kurizki, I. Mazets, J. Majer, and J. Schmiedmayer, “Reversible state transfer between superconducting qubits and atomic ensembles,” *Phys. Rev. A*, vol. 79, p. 40304, Apr. 2009.
- [61] J. Verdú, H. Zoubi, C. Koller, J. Majer, H. Ritsch, and J. Schmiedmayer, “Strong Magnetic Coupling of an Ultracold Gas to a Superconducting Waveguide Cavity,” *Phys. Rev. Lett.*, vol. 103, p. 43603, July 2009.
- [62] K. Henschel, J. Majer, J. Schmiedmayer, and H. Ritsch, “Cavity QED with an ultracold ensemble on a chip: Prospects for strong magnetic coupling at finite temperatures,” *Phys. Rev. A*, vol. 82, p. 033810, Jan. 2010.
- [63] K. R. Patton and U. R. Fischer, “Hybrid of superconducting quantum interference device and atomic Bose-Einstein condensate: An architecture for quantum information processing,” *Phys. Rev. A*, vol. 87, p. 052303, Jan. 2013.
- [64] J. E. Hoffman, J. A. Grover, Z. Kim, A. K. Wood, J. R. Anderson, A. J. Dragt, M. Hafezi, C. J. Lobb, L. A. Orozco, S. L. Rolston, J. M. Taylor, C. P. Vlahacos, and F. C. Wellstood, “Atoms Talking to SQUIDs,” *Rev. Mex. Fís. S.*, vol. 57, p. 1, Aug. 2011.
- [65] S. Minniberger, F. Diorico, S. Haslinger, C. Hufnagel, C. Novotny, N. Lippok, J. Majer, C. Koller, S. Schneider, and J. Schmiedmayer, “Magnetic conveyor belt transport of ultracold atoms to a superconducting atomchip,” *Appl. Phys. B*, vol. 116, pp. 1017–1021, Nov. 2014.
- [66] B. Kasch, H. Hattermann, D. Cano, T. Judd, S. Scheel, C. Zimmermann, R. Kleiner, D. Koelle, and J. Fortágh, “Cold atoms near superconductors: atomic spin coherence beyond the Johnson noise limit,” *New J. Phys.*, vol. 12, p. 65024, 2010.
- [67] S. Bernon, H. Hattermann, D. Bothner, M. Knufinke, P. Weiss, F. Jessen, D. Cano, M. Kemmler, R. Kleiner, D. Koelle, and J. Fortágh, “Manipulation and coherence of ultra-cold atoms on a superconducting atom chip.,” *Nat. Commun.*, vol. 4, p. 2380, Feb. 2013.

- [68] F. Jessen, M. Knufinke, S. C. Bell, P. Vergien, H. Hattermann, P. Weiss, M. Rudolph, M. Reinschmidt, K. Meyer, T. Gaber, D. Cano, A. Günther, S. Bernon, D. Koelle, R. Kleiner, and J. Fortágh, “Trapping of ultracold atoms in a 3He/4He dilution refrigerator,” *Appl. Phys. B*, vol. 116, pp. 665–671, Dec. 2013.
- [69] P. Weiss, M. Knufinke, S. Bernon, D. Bothner, L. Sárkány, C. Zimmermann, R. Kleiner, D. Koelle, J. Fortágh, and H. Hattermann, “Sensitivity of Ultracold Atoms to Quantized Flux in a Superconducting Ring,” *Phys. Rev. Lett.*, vol. 114, p. 113003, Mar. 2015.
- [70] R. Barends, J. Wenner, M. Lenander, Y. Chen, R. C. Bialczak, J. Kelly, E. Lucero, P. O’Malley, M. Mariantoni, D. Sank, H. Wang, T. C. White, Y. Yin, J. Zhao, A. N. Cleland, J. M. Martinis, and J. J. A. Baselmans, “Minimizing quasiparticle generation from stray infrared light in superconducting quantum circuits,” *Appl. Phys. Lett.*, vol. 99, p. 113507, Sept. 2011.
- [71] A. D. Córcoles, J. M. Chow, J. M. Gambetta, C. Rigetti, J. R. Rozen, G. A. Keefe, M. Beth Rothwell, M. B. Ketchen, and M. Steffen, “Protecting superconducting qubits from radiation,” *Appl. Phys. Lett.*, vol. 99, p. 181906, Nov. 2011.
- [72] C.-S. Lee, B. Janko, I. Derenyi, and A.-L. Barabasi, “Reducing vortex density in superconductors using the ‘ratchet effect’,” *Nature*, vol. 400, pp. 337–340, July 1999.
- [73] G. Stan, S. Field, and J. Martinis, “Critical Field for Complete Vortex Expulsion from Narrow Superconducting Strips,” *Phys. Rev. Lett.*, vol. 92, p. 097003, Mar. 2004.
- [74] J. E. Hoffman, S. Ravets, J. A. Grover, P. Solano, P. R. Kordell, J. D. Wong-Campos, L. A. Orozco, and S. L. Rolston, “Ultrahigh transmission optical nanofibers,” *AIP Adv.*, vol. 4, p. 067124, June 2014.
- [75] K. Voigt, J. Hertzberg, J. E. Hoffman, J. A. Grover, P. Solano, R. P. Budoyo, C. J. Ballard, J. Lee, J. R. Anderson, C. J. Lobb, L. a. Orozco, S. L. Rolston, and F. C. Wellstood, “Movable Thin-Film Superconducting Resonator Coupled to a Tapered Optical Microfiber at 15 mK,” *IEEE Trans. Appl. Supercond.*, vol. 25, no. 3, 2014.
- [76] T. Grünzweig, A. Hilliard, M. McGovern, and M. F. Andersen, “Near-deterministic preparation of a single atom in an optical microtrap,” *Nat. Phys.*, vol. 6, pp. 951–954, Sept. 2010.
- [77] J. Lee, J. A. Grover, L. A. Orozco, and S. L. Rolston, “Sub-Doppler cooling of neutral atoms in a grating magneto-optical trap,” *JOSA B*, vol. 30, p. 2869, Jan. 2013.

- [78] J. E. Hoffman, *Optical nanofiber fabrication and analysis towards coupling atoms to superconducting qubits*. PhD thesis, University of Maryland College Park, 2014.
- [79] G. Brambilla, F. Xu, P. Horak, Y. Jung, F. Koizumi, N. Sessions, E. Koukharenko, X. Feng, G. Murugan, J. Wilkinson, and D. Richardson, “Optical fiber nanowires and microwires: fabrication and applications,” *Adv. Opt. Photonics*, vol. 1, p. 107, Jan. 2009.
- [80] G. Brambilla, “Optical fibre nanowires and microwires: a review,” *J. Opt.*, vol. 12, p. 043001, Apr. 2010.
- [81] T. Birks and Y. Li, “The shape of fiber tapers,” *Light. Technol. J.*, vol. 10, no. 4, pp. 432–438, 1992.
- [82] F. Warken, *Ultradünne Glasfasern als Werkzeug zur Kopplung von Licht und Materie*. PhD thesis, University of Mainz, 2007.
- [83] H. L. Sørensen, E. S. Polzik, and J. Appel, “Heater Self-Calibration Technique for Shape Prediction of Fiber Tapers,” *J. Light. Technol.*, vol. 32, pp. 1886–1891, Dec. 2014.
- [84] R. Nagai and T. Aoki, “Ultra-low-loss tapered optical fibers with minimal lengths,” *Opt. Express*, vol. 22, p. 28427, Nov. 2014.
- [85] J. M. Ward, A. Maimaiti, V. H. Le, and S. N. Chormaic, “Contributed Review: Optical micro- and nanofiber pulling rig,” *Rev. Sci. Instrum.*, vol. 85, p. 111501, Nov. 2014.
- [86] S. Ravets, J. E. Hoffman, P. R. Kordell, J. D. Wong-Campos, S. L. Rolston, and L. A. Orozco, “Intermodal energy transfer in a tapered optical fiber: optimizing transmission,” *JOSA A*, vol. 30, pp. 2361–71, Jan. 2013.
- [87] M. C. Frawley, A. Petcu-Colan, V. G. Truong, and S. Nic Chormaic, “Higher order mode propagation in an optical nanofiber,” *Opt. Commun.*, vol. 285, pp. 4648–4654, Oct. 2012.
- [88] S. Ravets, J. E. Hoffman, L. A. Orozco, S. L. Rolston, G. Beadie, and F. K. Fatemi, “A low-loss photonic silica nanofiber for higher-order modes,” *Opt. Express*, vol. 21, pp. 18325–35, July 2013.
- [89] E. D. Black, “An introduction to Pound–Drever–Hall laser frequency stabilization,” *Am. J. Phys.*, vol. 69, no. January 2000, p. 79, 2001.
- [90] K. Huang, H. Le Jeannic, J. Ruaudel, O. Morin, and J. Laurat, “Microcontroller-based locking in optics experiments,” *Rev. Sci. Instrum.*, vol. 85, p. 123112, Dec. 2014.
- [91] C. J. Foot, *Atomic Physics*. Oxford University Press, 2005.

- [92] K. L. Corwin, Z.-T. Lu, C. F. Hand, R. J. Epstein, and C. E. Wieman, “Frequency-Stabilized Diode Laser with the Zeeman Shift in an Atomic Vapor,” *Appl. Opt.*, vol. 37, p. 3295, May 1998.
- [93] A. Millett-Sikking, I. G. Hughes, P. Tierney, and S. L. Cornish, “DAVLL lineshapes in atomic rubidium,” *J. Phys. B At. Mol. Opt. Phys.*, vol. 40, pp. 187–198, Jan. 2007.
- [94] M. L. Harris, S. L. Cornish, A. Tripathi, and I. G. Hughes, “Optimization of sub-Doppler DAVLL on the rubidium D2 line,” *J. Phys. B At. Mol. Opt. Phys.*, vol. 41, p. 085401, Apr. 2008.
- [95] D. Budker, W. Gawlik, D. F. Kimball, and S. M. Rochester, “Resonant non-linear magneto-optical effects in atoms,” *Rev. Mod. Phys.*, Jan. 2002.
- [96] J. H. Moore, C. C. Davis, M. A. Coplan, and S. C. Greer, *Building Scientific Apparatus*. Cambridge University Press, 4th ed., 2009.
- [97] F. Le Kien, S. Dutta Gupta, V. Balykin, and K. Hakuta, “Spontaneous emission of a cesium atom near a nanofiber: Efficient coupling of light to guided modes,” *Phys. Rev. A*, vol. 72, p. 32509, Sept. 2005.
- [98] S. Dawkins, R. Mitsch, D. Reitz, E. Vetsch, and A. Rauschenbeutel, “Dispersive Optical Interface Based on Nanofiber-Trapped Atoms,” *Phys. Rev. Lett.*, vol. 107, p. 243601, Aug. 2011.
- [99] D. E. Chang, L. Jiang, and A. V. Gorshkov, “Cavity QED with atomic mirrors,” *New J. Phys.*, vol. 14, p. 063003, Jan. 2012.
- [100] D. E. Chang, J. I. Cirac, and H. J. Kimble, “Self-organization of atoms along a nanophotonic waveguide,” *Phys. Rev. Lett.*, vol. 110, p. 113606, Jan. 2013.
- [101] T. Grießer and H. Ritsch, “Light-Induced Crystallization of Cold Atoms in a 1D Optical Trap,” *Phys. Rev. Lett.*, vol. 111, p. 055702, Aug. 2013.
- [102] E. Vetsch, S. T. Dawkins, R. Mitsch, D. Reitz, P. Schneeweiss, and A. Rauschenbeutel, “Nanofiber-Based Optical Trapping of Cold Neutral Atoms,” *IEEE J. Sel. Top. Quantum Electron.*, vol. 18, pp. 1763–1770, Feb. 2012.
- [103] C. Wuttke, G. Cole, and A. Rauschenbeutel, “Optically active mechanical modes of tapered optical fibers,” *Phys. Rev. A*, vol. 88, p. 061801, Nov. 2013.
- [104] W. Demtröder, *Laser Spectroscopy: Basic Concepts and Instrumentation*. Springer, 2003.
- [105] R. Loudon, *The Quantum Theory of Light*. Oxford University Press, 2000.

- [106] H. J. Carmichael, P. Drummond, P. Meystre, and D. Walls, “Intensity correlations in resonance fluorescence with atomic number fluctuations,” *J. Phys. A. Math. Gen.*, vol. 11, no. 5, p. L121, 1978.
- [107] H. J. Kimble, M. Dagenais, and L. Mandel, “Multiatom and transit-time effects on photon-correlation measurements in resonance fluorescence,” *Phys. Rev. A*, vol. 18, no. 1, pp. 201–207, 1978.
- [108] M. Hennrich, A. Kuhn, and G. Rempe, “Transition from Antibunching to Bunching in Cavity QED,” *Phys. Rev. Lett.*, vol. 94, p. 53604, Feb. 2005.
- [109] D. G. Norris, E. J. Cahoon, and L. A. Orozco, “Atom detection in a two-mode optical cavity with intermediate coupling: Autocorrelation studies,” *Phys. Rev. A*, vol. 80, p. 043830, Oct. 2009.
- [110] V. Gomer, B. Ueberholz, S. Knappe, F. Strauch, D. Frese, and D. Meschede, “Decoding the dynamics of a single trapped atom from photon correlations,” *Appl. Phys. B Lasers Opt.*, vol. 67, no. 6, pp. 689–697, 1998.
- [111] V. Gomer, F. Strauch, B. Ueberholz, S. Knappe, and D. Meschede, “Single-atom dynamics revealed by photon correlations,” *Phys. Rev. A*, vol. 58, pp. R1657–R1660, Sept. 1998.
- [112] D. Rotter, M. Mukherjee, F. Dubin, and R. Blatt, “Monitoring a single ion’s motion by second-order photon correlations,” *New J. Phys.*, vol. 10, p. 043011, Jan. 2008.
- [113] F. Le Kien and K. Hakuta, “Correlations between photons emitted by multiatom fluorescence into a nanofiber,” *Phys. Rev. A*, vol. 77, p. 33826, Mar. 2008.
- [114] K. Nayak and K. Hakuta, “Single atoms on an optical nanofibre,” *New J. Phys.*, vol. 10, p. 53003, Jan. 2008.
- [115] K. Nayak, F. Le Kien, M. Morinaga, and K. Hakuta, “Antibunching and bunching of photons in resonance fluorescence from a few atoms into guided modes of an optical nanofiber,” *Phys. Rev. A*, vol. 79, p. 21801, Feb. 2009.
- [116] M. Das, A. Shirasaki, K. Nayak, M. Morinaga, F. Le Kien, and K. Hakuta, “Measurement of fluorescence emission spectrum of few strongly driven atoms using an optical nanofiber,” *Opt. Express*, vol. 18, no. 16, pp. 17154–17164, 2010.
- [117] X. T. Zou and L. Mandel, “Photon-antibunching and sub-Poissonian photon statistics,” *Phys. Rev. A*, vol. 41, no. 1, pp. 475–476, 1990.
- [118] H. Paul, “Photon antibunching,” *Rev. Mod. Phys.*, vol. 54, pp. 1061–1102, Oct. 1982.

- [119] R. Grimm, M. Weidemuller, and Y. B. Ovchinnikov, “Optical dipole traps for neutral atoms,” *Adv. At. Mol. Opt. Physics*, vol. 42, pp. 95–170, Jan. 2000.
- [120] D. J. Alton, N. P. Stern, T. Aoki, H. Lee, E. Ostby, K. J. Vahala, and H. J. Kimble, “Strong interactions of single atoms and photons near a dielectric boundary,” *Nat. Phys.*, vol. 7, pp. 159–165, Nov. 2010.
- [121] N. P. Stern, D. J. Alton, and H. J. Kimble, “Simulations of atomic trajectories near a dielectric surface,” *New J. Phys.*, vol. 13, p. 085004, Aug. 2011.
- [122] M. C. Frawley, S. Nic Chormaic, and V. G. Minogin, “The van der Waals interaction of an atom with the convex surface of a nanocylinder,” *Phys. Scr.*, vol. 85, p. 058103, May 2012.
- [123] D. A. Steck, “Rubidium 87 D Line Data,” 2001.
- [124] F. Le Kien, V. Balykin, and K. Hakuta, “Scattering of an evanescent light field by a single cesium atom near a nanofiber,” *Phys. Rev. A*, vol. 73, p. 13819, Jan. 2006.
- [125] A. V. Masalov and V. G. Minogin, “Pumping of higher-order modes of an optical nanofiber by laser excited atoms,” *Laser Phys. Lett.*, vol. 10, p. 075203, Jan. 2013.
- [126] F. Le Kien and K. Hakuta, “Position distribution of cold thermal atoms in the vicinity of a dielectric surface,” *Phys. Rev. A*, vol. 77, p. 042903, Apr. 2008.
- [127] F. W. J. Olver, D. W. Lozier, R. F. Boisvert, and C. W. Clark, eds., *NIST Handbook of Mathematical Functions*. New York, NY: Cambridge University Press, 2010.
- [128] G. Sagué, E. Vetsch, W. Alt, D. Meschede, and A. Rauschenbeutel, “Cold-Atom Physics Using Ultrathin Optical Fibers: Light-Induced Dipole Forces and Surface Interactions,” *Phys. Rev. Lett.*, vol. 99, p. 163602, Oct. 2007.
- [129] L. Russell, R. Kumar, V. Tiwari, and S. Nic Chormaic, “Measurements on release–recapture of cold 85Rb atoms using an optical nanofibre in a magneto-optical trap,” *Opt. Commun.*, vol. 309, pp. 313–317, Nov. 2013.
- [130] J. Fu, X. Yin, and L. Tong, “Two-colour atom guide and 1D optical lattice using evanescent fields of high-order transverse modes,” *J. Phys. B At. Mol. Opt. Phys.*, vol. 40, pp. 4195–4210, Nov. 2007.
- [131] J. Fu, X. Yin, N. Li, and L. Tong, “Atom waveguide and 1D optical lattice using a two-color evanescent light field around an optical micro/nano-fiber,” *Chin. Opt. Lett.*, vol. 6, no. 2, pp. 112–115, 2008.
- [132] G. Sagué, A. Baade, and A. Rauschenbeutel, “Blue-detuned evanescent field surface traps for neutral atoms based on mode interference in ultrathin optical fibres,” *New J. Phys.*, vol. 10, p. 113008, Nov. 2008.

- [133] R. Kumar, V. Gokhroo, K. Deasy, A. Maimaiti, M. C. Frawley, C. Phelan, and S. N. Chormaic, “Interaction of laser-cooled  $^{87}\text{Rb}$  atoms with higher order modes of an optical nanofibre,” *New J. Phys.*, vol. 17, p. 013026, Jan. 2015.
- [134] J. E. Simsarian, L. A. Orozco, G. D. Sprouse, and W. Z. Zhao, “Lifetime measurements of the  $7p$  levels of atomic francium,” *Phys. Rev. A*, vol. 57, no. 4, pp. 2448–2458, 1998.
- [135] B. M. Patterson, J. F. Sell, T. Ehrenreich, M. A. Gearba, G. M. Brooke, J. Scoville, and R. J. Knize, “Lifetime measurement of the cesium  $6P_{3/2}$  level using ultrafast pump-probe 1,” *Phys. Rev. A*, vol. 91, p. 012506, Jan. 2015.
- [136] W. Z. Zhao, J. E. Simsarian, L. A. Orozco, W. Shi, and G. D. Sprouse, “Measurement of the  $7p^2P_{3/2}$  Level Lifetime in Atomic Francium,” *Phys. Rev. Lett.*, vol. 78, no. 22, pp. 4169–4172, 1997.
- [137] H. Kuhn, “Classical Aspects of Energy Transfer in Molecular Systems,” *J. Chem. Phys.*, vol. 53, p. 101, Sept. 1970.
- [138] R. R. Chance, A. Prock, and R. Silbey, “Molecular fluorescence and energy transfer near interfaces,” *Adv. Chem. Phys.*, vol. 37, no. 1, p. 1, 1978.
- [139] X.-s. Li and C.-d. Gong, “Resonance fluorescence of an adatom near solid surfaces,” *Phys. Rev. A*, vol. 35, pp. 1595–1602, Feb. 1987.
- [140] X.-s. Li, D. Lin, and T. George, “Spontaneous decay and resonance fluorescence of an admolecule near a silver surface with random roughness,” *Phys. Rev. B*, vol. 41, pp. 8107–8111, Apr. 1990.
- [141] V. Klimov and M. Ducloy, “Spontaneous emission rate of an excited atom placed near a nanofiber,” *Phys. Rev. A*, vol. 69, p. 13812, Jan. 2004.
- [142] L. Russell, D. A. Gleeson, V. G. Minogin, and S. Nic Chormaic, “Spectral distribution of atomic fluorescence coupled into an optical nanofibre,” *J. Phys. B At. Mol. Opt. Phys.*, vol. 42, p. 185006, 2009.
- [143] M. Chevrollier, D. Bloch, G. Rahmat, and M. Ducloy, “Van der Waals-induced spectral distortions in selective-reflection spectroscopy of Cs vapor: the strong atom-surface interaction regime,” *Opt. Lett.*, vol. 16, p. 1879, Dec. 1991.
- [144] V. V. Ivanov, R. A. Cornelussen, H. B. v. L. van den Heuvell, and R. J. C. Spreeuw, “Observation of modified radiative properties of cold atoms in vacuum near a dielectric surface,” *J. Opt. B Quantum Semiclassical Opt.*, vol. 6, pp. 454–459, Nov. 2004.
- [145] B. E. Schultz, H. Ming, G. A. Noble, and W. A. van Wijngaarden, “Measurement of the Rb D2 transition linewidth at ultralow temperature,” *Eur. Phys. J. D*, vol. 48, pp. 171–176, June 2008.

- [146] K. A. Whittaker, J. Keaveney, I. G. Hughes, A. Sargsyan, D. Sarkisyan, and C. S. Adams, “Optical Response of Gas-Phase Atoms at Less than  $\lambda/80$  from a Dielectric Surface,” *Phys. Rev. Lett.*, vol. 112, p. 253201, June 2014.
- [147] C. Stehle, C. Zimmermann, and S. Slama, “Cooperative coupling of ultracold atoms and surface plasmons,” *Nat. Phys.*, vol. 10, pp. 937–942, Oct. 2014.
- [148] K. H. Drexhage, “Influence of a dielectric interface on fluorescence decay time,” *Journal of Luminescence*, vol. 1-2, pp. 693–701, 1970.
- [149] P. B. Coates, “The correction for photon ‘pile-up’ in the measurement of radiative lifetimes,” *J. Phys. E.*, vol. 1, pp. 878–879, Aug. 1968.
- [150] P. B. Coates, “Pile-up corrections in the measurement of lifetimes,” *J. Phys. E.*, vol. 5, pp. 148–150, Feb. 1972.
- [151] G. Labeyrie, R. Kaiser, and D. Delande, “Radiation trapping in a cold atomic gas,” *Appl. Phys. B Lasers Opt.*, vol. 81, no. 2005, pp. 1001–1008, 2005.
- [152] A. A. Istratov and O. F. Vyvenko, “Exponential analysis in physical phenomena,” *Rev. Sci. Instrum.*, vol. 70, p. 1233, Feb. 1999.
- [153] K. Lee, J. Kim, H. Noh, and W. Jhe, “Single-beam atom trap in a pyramidal and conical hollow mirror,” *Opt. Lett.*, vol. 21, no. 15, pp. 1177–1179, 1996.
- [154] J. A. Kim, K. I. Lee, H. R. Noh, W. Jhe, and M. Ohtsu, “Atom trap in an axicon mirror,” *Opt. Lett.*, Jan. 1997.
- [155] M. Vangeleyn, P. F. Griffin, E. Riis, and A. S. Arnold, “Single-laser, one beam, tetrahedral magneto-optical trap,” *Opt. Express*, vol. 17, p. 13601, July 2009.
- [156] M. Vangeleyn, P. F. Griffin, E. Riis, and A. S. Arnold, “Laser cooling with a single laser beam and a planar diffractor.,” *Opt. Lett.*, vol. 35, pp. 3453–5, Oct. 2010.
- [157] C. C. Nshii, M. Vangeleyn, J. P. Cotter, P. F. Griffin, E. A. Hinds, C. N. Ironside, P. See, A. G. Sinclair, E. Riis, and A. S. Arnold, “A surface-patterned chip as a strong source of ultracold atoms for quantum technologies.,” *Nat. Nanotechnol.*, vol. 8, pp. 321–4, May 2013.
- [158] K. Petsas, A. Coates, and G. Grynberg, “Crystallography of optical lattices,” *Phys. Rev. A*, vol. 50, pp. 5173–5189, Dec. 1994.
- [159] V. Minogin and O. Serimaa, “Resonant light pressure forces in a strong standing laser wave,” *Opt. Commun.*, vol. 30, pp. 373–379, Sept. 1979.
- [160] M. Walhout, J. Dalibard, S. L. Rolston, and W. D. Phillips, “ $\sigma_- + \sigma_-$  Optical molasses in a longitudinal magnetic field,” *J. Opt. Soc. Am. B*, vol. 9, p. 1997, Nov. 1992.

- [161] C. Townsend, N. Edwards, C. Cooper, K. Zetie, C. Foot, A. Steane, P. Sriftgiser, H. Perrin, and J. Dalibard, “Phase-space density in the magneto-optical trap,” *Phys. Rev. A*, vol. 52, pp. 1423–1440, Aug. 1995.
- [162] T. Walker, D. Sesko, and C. Wieman, “Collective behavior of optically trapped neutral atoms,” *Phys. Rev. Lett.*, vol. 64, pp. 408–411, Jan. 1990.
- [163] K. Lindquist, M. Stephens, and C. Wieman, “Experimental and theoretical study of the vapor-cell Zeeman optical trap,” *Phys. Rev. A*, vol. 46, pp. 4082–4090, Oct. 1992.
- [164] T. Isayama, Y. Takahashi, N. Tanaka, K. Toyoda, K. Ishikawa, and T. Yabuzaki, “Observation of Larmor spin precession of laser-cooled Rb atoms via paramagnetic Faraday rotation,” *Phys. Rev. A*, vol. 59, pp. 4836–4839, June 1999.
- [165] M. Terraciano, M. Bashkansky, and F. Fatemi, “Faraday spectroscopy of atoms confined in a dark optical trap,” *Phys. Rev. A*, vol. 77, p. 063417, June 2008.
- [166] F. K. Fatemi and M. Bashkansky, “Spatially resolved magnetometry using cold atoms in dark optical tweezers.,” *Opt. Express*, vol. 18, pp. 2190–6, Feb. 2010.
- [167] P. Schneeweiss, F. L. Kien, and A. Rauschenbeutel, “Nanofiber-based atom trap created by combining fictitious and real magnetic fields,” *New J. Phys.*, vol. 16, p. 013014, Jan. 2014.
- [168] C. Wuttke and A. Rauschenbeutel, “Thermalization via Heat Radiation of an Individual Object Thinner than the Thermal Wavelength,” *Phys. Rev. Lett.*, vol. 111, p. 024301, July 2013.
- [169] K. Dieckmann, R. Spreeuw, M. Weidemüller, and J. Walraven, “Two-dimensional magneto-optical trap as a source of slow atoms,” *Phys. Rev. A*, vol. 58, pp. 3891–3895, Nov. 1998.
- [170] J. Schoser, A. Batär, R. Löw, V. Schweikhart, A. Grabowski, Y. Ovchinnikov, and T. Pfau, “Intense source of cold Rb atoms from a pure two-dimensional magneto-optical trap,” *Phys. Rev. A*, vol. 66, p. 023410, Aug. 2002.
- [171] T. Tiecke, S. Gensemer, A. Ludewig, and J. Walraven, “High-flux two-dimensional magneto-optical-trap source for cold lithium atoms,” *Phys. Rev. A*, vol. 80, p. 013409, July 2009.
- [172] A. Black, H. Chan, and V. Vuletić, “Observation of Collective Friction Forces due to Spatial Self-Organization of Atoms: From Rayleigh to Bragg Scattering,” *Phys. Rev. Lett.*, vol. 91, p. 203001, Nov. 2003.

- [173] K. Baumann, C. Guerlin, F. Brennecke, and T. Esslinger, “Dicke quantum phase transition with a superfluid gas in an optical cavity.,” *Nature*, vol. 464, pp. 1301–6, Apr. 2010.
- [174] F. Le Kien and A. Rauschenbeutel, “Anisotropy in scattering of light from an atom into the guided modes of a nanofiber,” *Phys. Rev. A*, vol. 90, p. 023805, May 2014.
- [175] R. Mitsch, C. Sayrin, B. Albrecht, P. Schneeweiss, and A. Rauschenbeutel, “Quantum state-controlled directional spontaneous emission of photons into a nanophotonic waveguide,” *Nat. Commun.*, vol. 5, p. 5713, Dec. 2014.
- [176] D. O’Shea, C. Junge, J. Volz, and A. Rauschenbeutel, “Fiber-Optical Switch Controlled by a Single Atom,” *Phys. Rev. Lett.*, vol. 111, p. 193601, Nov. 2013.
- [177] A. W. Snyder and J. D. Love, *Optical Waveguide Theory*. Chapman and Hall, 1983.
- [178] A. Yariv, *Optical Electronics*. Oxford University Press, 1990.
- [179] G. Sagué, *Cold atom physics using ultra-thin optical fibres*. PhD thesis, University of Mainz, 2008.
- [180] E. Vetsch, *Optical Interface Based on a Nanofiber*. PhD thesis, University of Mainz, 2010.
- [181] C. Wuttke, *Thermal excitations of optical nanofibers measured with a cavity*. PhD thesis, University of Mainz, 2014.
- [182] J. M. Gere and B. J. Goodno, *Mechanics of Materials*. Cengage Learning, 8 ed., 2012.
- [183] H. D. Conway and J. F. Dubil, “Vibration Frequencies of Truncated-Cone and Wedge Beams,” *J. Appl. Mech.*, vol. 32, p. 932, Dec. 1965.
- [184] H. H. Mabie, “Transverse vibrations of double-tapered cantilever beams with end support and with end mass,” *J. Acoust. Soc. Am.*, vol. 55, p. 986, Aug. 1974.
- [185] E. Suhir, “Predicted stresses and strains in fused biconical taper couplers subjected to tension.,” *Appl. Opt.*, vol. 32, pp. 3237–40, June 1993.
- [186] S. Naguleswaran, “A Direct Solution for the Transverse Vibration of Euler-Bernoulli Wedge and Cone Beams,” *J. Sound Vib.*, vol. 172, pp. 289–304, May 1994.
- [187] N. Auciello and A. Ercolano, “Exact solution for the transverse vibration of a beam a part of which is a taper beam and other part is a uniform beam,” *Int. J. Solids Struct.*, vol. 34, pp. 2115–2129, June 1997.

- [188] N. Auciello, “On the transverse vibrations of non-uniform beams with axial loads and elastically restrained ends,” *Int. J. Mech. Sci.*, vol. 43, pp. 193–208, Jan. 2001.
- [189] M. C. Ece, M. Aydogdu, and V. Taskin, “Vibration of a variable cross-section beam,” *Mech. Res. Commun.*, vol. 34, pp. 78–84, Jan. 2007.
- [190] A. Bokaian, “Natural frequencies of beams under tensile axial loads,” *J. Sound Vib.*, vol. 142, pp. 481–498, Nov. 1990.
- [191] P. Seshu and K. D. Dhuri, “Corrected Formulas for Natural Frequencies of Cantilever Beams Under Uniform Axial Tension,” *AIAA J.*, vol. 45, p. 1435, May 2012.
- [192] S. Holleis, T. Hoinkes, C. Wuttke, P. Schneeweiss, and A. Rauschenbeutel, “Experimental stress-strain analysis of tapered silica optical fibers with nanofiber waist,” *Appl. Phys. Lett.*, vol. 104, p. 163109, Jan. 2014.
- [193] Y.-j. Lin, I. Teper, C. Chin, and V. Vuletić, “Impact of the Casimir-Polder Potential and Johnson Noise on Bose-Einstein Condensate Stability Near Surfaces,” *Phys. Rev. Lett.*, vol. 92, p. 050404, Feb. 2004.
- [194] J. Märkle, A. J. Allen, P. Federsel, B. Jetter, A. Günther, J. Fortágh, N. P. Proukakis, and T. E. Judd, “Evaporative cooling of cold atoms at surfaces,” *Phys. Rev. A*, vol. 90, p. 023614, Aug. 2014.
- [195] I. H. Malitson, “Interspecimen Comparison of the Refractive Index of Fused Silica,” *J. Opt. Soc. Am.*, vol. 55, p. 1205, Oct. 1965.
- [196] F. Le Kien, P. Schneeweiss, and A. Rauschenbeutel, “Dynamical polarizability of atoms in arbitrary light fields: general theory and application to cesium,” *Eur. Phys. J. D*, vol. 67, p. 92, Nov. 2013.
- [197] M. S. Safranova and U. I. Safranova, “Critically evaluated theoretical energies, lifetimes, hyperfine constants, and multipole polarizabilities in  $^{87}\text{Rb}$ ,” *Phys. Rev. A*, vol. 83, p. 052508, May 2011.
- [198] B. Arora and B. K. Sahoo, “State-insensitive trapping of Rb atoms: linearly versus circularly polarized lights,” *Phys. Rev. A*, vol. 86, p. 033416, Sept. 2012.
- [199] L. Spruch and Y. Tikochinsky, “Elementary approximate derivations of some retarded Casimir interactions involving one or two dielectric walls,” *Phys. Rev. A*, vol. 48, pp. 4213–4222, Dec. 1993.